



University of Technology, Sydney

Faculty of Engineering and Information Technology

Modelling and State-of-Charge Estimation for Ultracapacitors in Electric Vehicles

A thesis submitted for the degree of

Doctor of Philosophy

Lei ZHANG

(2016)

Title of the thesis:

Modelling and State-of-Charge estimation for ultracapacitors in electric vehicles

Ph.D. student:

Lei Zhang

E-mail: Lei.Zhang-15@student.uts.edu.au

Supervisor:

Dr. Li Li

E-mail: Li.Li@uts.edu.au

Co-Supervisor:

A.Prof. Youguang Guo

E-mail: Youguang.Guo-1@uts.edu.au

External Supervisor:

Prof. David G. Dorrell

E-mail: dorrelld@ukzn.ac.za

Address:

School of Electrical, Mechanical and Mechatronic Systems

University of Technology, Sydney, 15 Broadway, Ultimo, NSW 2007, Australia

Certificate of Original Authorship

I certify that the work in this thesis has not previously been submitted for a degree nor has it been submitted as part of requirements for a degree except as fully acknowledged within the text.

I also certify that the thesis has been written by me. Any help that I have received in my research work and the preparation of the thesis itself has been acknowledged. In addition, I certify that all information sources and literature used are indicated in the thesis.

Signature of Student:

Lei Zhang

Date:

Acknowledgments

I would express my deep gratitude to both of my principal Professors David. G. Dorrell, formerly with UTS, now with The University of Kwazulu-Natal, and Zhenpo Wang, with BIT, for their guidance and encouragement during my studies. I also would like to thank my other supervisors, Prof. Fengchun Sun, Dr. Li Li, A. Prof. Youguang Guo, for their help and advice.

I am extremely thankful to my friend Prof. Xiaosong Hu. He discussed research points in detail, and gave me insightful advice. I also appreciate his efforts in reviewing this thesis.

I would like to thank my friends and colleagues, Xingxing Zhou, Jinglai Wu, Yu Wang, Sangzhi Zhu, Tianxiao Zhang, Guangzhogn Xu, Jiageng Ruan, Shuo Wang, Bo Zhu, Jianwei Zhang, Linfeng Zheng, for their support in daily life.

Finally, my deepest thanks go to my family. Without their potent understanding and support, it is not possible for me to complete this thesis.

Publications and Conference Contributions

The following publications are part of the thesis.

1. Published journal papers

- [1] **L. Zhang***, X. Hu, Z. Wang, D. G. Dorrell, Experimental Investigation of Ultracapacitor Impedance Characteristics. *Energy Procedia* **75** (2015) 1888-1894.
- [2] **L. Zhang***, X. Hu, Z. Wang, F. Sun, D. G. Dorrell, Fractional-Order Modeling and State-of-Charge Estimation for Ultracapacitors. *Journal of Power Sources* 314 (2016) 28-34.
- [3] **L. Zhang***, X. Hu, Z. Wang, F. Sun, D. G. Dorrell, Experimental Impedance Investigation of an Ultracapacitor at Different Conditions for Electric Vehicle Applications. *Journal of Power Sources* **287** (2015) 129-138.
- [4] **L. Zhang***, Z. Wang, X. Hu, F. Sun, D. G. Dorrell, A Comparative Study of Equivalent Circuit Models of Ultracapacitors for Electric Vehicles. *Journal of Power Sources* **274** (2015) 899-906.
- [5] **L. Zhang***, Z. Wang, F. Sun, D. G. Dorrell, Online Parameter Identification of Ultracapacitor Models Using the Extended Kalman Filter. *Energies* **2014**, 07, 3204-3217.

2. Journal papers under review

- [6] **L. Zhang***, X. Hu, Z. Wang, F. Sun, J. Deng, D. G. Dorrell, Multi-Objective optimal sizing of hybrid energy storage system for electric vehicles. *IEEE Transactions on Vehicular Technology*, 2016
- [7] **L. Zhang***, X. Hu, Z. Wang, F. Sun, D. G. Dorrell, A Survey of ultracapacitor modeling, estimation and applications. *Journal of Power Sources*, 2016

3. Published conference paper

- [1] **L. Zhang***, X. Hu, S. Su, D. G. Dorrell, Robust State-of-Charge Estimation of

Ultracapacitors for Electric Vehicles. *The 13th IEEE International Conference on Industrial Informatics (INDIN)*, Cambridge, UK, 2015.

Abstract

In order to cope with the global challenges like fossil fuel depletion and environmental pollution, electrified vehicles (EVs) have been widely accepted as an enabling option for future ground mobility. In comparison to conventional combustion engine vehicles, EVs have the advantage of high efficiency, environment-friendly operation and excellent control flexibility. There is a proviso here that the electricity used by the EV is from a green source such as hydro, wind or solar. The energy storage system (ESS) is a key ingredient of an EV, and significantly affects its driving performance and cost-effectiveness. The exploration of a vehicular ESS poses a formidable challenge, because of high power/energy demands and unpredictable driving environments. Li-ion batteries represent a main choice for this use, but suffer the drawbacks of low power density and poor recyclability. Recently, ultracapacitors (UCs), also referred to as supercapacitors (SCs) or electric double-layer capacitors (EDLCs), have gained increasing attention in the energy storage community, thanks to their high power density, high efficiency, fast charge, wide temperature window and excellent recyclability. These advantages make UCs a good augmentation to high-energy ESSs (e.g., fuel cells, lithium-ion batteries). This combination represents a hybrid energy storage system (HESS) that can fully leverage the synergistic benefits of each constituent device. To ensure efficient, reliable and safe operations of UC systems, numerous challenges including modelling and characterization, and State-of-Charge (SOC) estimation should be effectually surmounted. In order to meet the above mentioned challenges, the main research presented in this dissertation includes:

1. A special test rig for UC characteristic investigation has been established. A test procedure is proposed to collect comprehensive test data. A plethora of tests have been conducted on this test rig including capacity calibration, experimental impedance investigation under different temperatures and SOC values, and dynamic cycling including pulse tests and driving-cycle-based tests under different temperatures, resulting in a wide-ranging UC database.

2. The impedance characteristics of UCs are experimentally investigated under different temperatures and SOC values. The results show that the impedance is highly sensitive to temperature and SOC; and the temperature effect is more significant. In particular, the coupling effect between the temperature and SOC is illustrated, and the high-efficiency SOC window is highlighted.

3. For UC modelling, three commonly used equivalent circuit models are systematically examined in terms of model accuracy, complexity and robustness in the context of EV applications. A genetic algorithm (GA) is employed to extract the optimal model parameters based on the Hybrid Pulse Power Characterization (HPPC) test data. The performance of these models is then evaluated and compared by measuring the model complexity, accuracy, and robustness against “unseen” data collected in the Dynamic Stress Test (DST) and a self-designed pulse (SDP) test. The validation results show that the dynamic model has the best overall performance for EV applications.

4. Online parameter identification of UC models is researched. The extended Kalman Filter (EKF) is proposed to recursively estimate the model parameters using the DST dataset, in which the dynamic model is used to represent the UC dynamics. The effectiveness and robustness of the proposed method is validated using another driving-cycle-based dataset.

5. A novel robust H -infinity observer is presented to realize UC SOC estimation in real-time. In comparison to the state-of-the-art Kalman filter-based (KF-based) methods, the developed robust scheme can ensure high estimation accuracy without prior knowledge of process and measurement noise statistical properties. More significantly, the proposed H -infinity observer proves to be more robust to modelling uncertainties arising from the change of thermal conditions and/or cell health status.

6. A novel fractional-order model is put forward to emulate the UC dynamics. In contrast to integer-order models, the presented fractional-order model has the merits of better model accuracy and fewer parameters. It consists of a series resistor, a constant-phase-element (CPE), and a Warburg-like element. The model parameters are optimally extracted using GA, based on the time-domain Federal Urban Driving Schedule (FUDS) test data acquired through the established test rig. By means of this fractional-order model, a fractional Kalman filter is synthesized to recursively estimate the UC SOC. Validation results show that the proposed fractional-order modelling and state estimation scheme is accurate and outperforms the current practice based on integral-order techniques.

7. An optimal HESS sizing method using a multi-objective optimization algorithm is presented, in which the primary goal is reducing the ESS cost and weight while prolonging battery life. To this end, a battery state-of-health (SOH) model is incorporated to quantitatively investigate the impact of component sizing on battery life. The wavelet-transform-based power management algorithm is adopted to realize the power coordination between the battery and UC packs. The results provide prudent insights into HESS sizing with different emphases.

Key words: electrified vehicles; ultracapacitor; extended Kalman filter; H -infinity observer; fractional-order modelling; hybrid energy storage system

Contents

Certificate of Original Authorship	i
Acknowledgments	ii
Publications and Conference Contributions.....	iii
Abstract.....	v
List of Tables	xii
List of Figures.....	xiii
Nomenclature.....	xv
1 Introduction.....	1
1.1 Background and Motivation	1
1.2 Literature Review	7
1.2.1 Ultracapacitor models	7
1.2.2 State-of-Charge estimation	15
1.2.3 Motivation and research aims	17
1.3 Contributions and Organization of the Thesis	19
1.3.1 Intellectual contributions	19
1.3.2 Document organization	21
2 Ultracapacitor Test and Its Impedance Characteristic Investigation.....	22
2.1 Test Rig.....	22
2.2 Test Procedure	26
2.3 Investigation of UC Impedance Characteristics.....	30
2.3.1 Temperature dependency of impedance.....	30
2.3.2 SOC dependency of impedance	34
2.4 Dynamic Model of the Ultracapacitor	38
2.5 Summary	47
3 A Comparative Study of Equivalent Circuit Models of Ultracapacitors for Electric Vehicles.....	49
3.1 Motivation.....	49
3.2 Model Description	52

3.3 Model Characterization.....	55
3.4. Comparison Result and Discussion	58
3.4.1 Model accuracy and robustness	58
3.4.2 Model complexity	63
3.5. Summary	64
4 An Online Parameter Identification of Ultracapacitor Models Using the Extended Kalman Filter	65
4.1 Motivation.....	65
4.2 Modelling and Parameter Estimation for UCs.....	67
4.2.1 UC model structure	67
4.2.2 Parameter estimation using the extended Kalman filter.....	68
4.3 Results and Discussion	72
4.3.1 Parameter estimation in the DST test.....	72
4.3.2 Model validation in the HPPC test.....	76
4.4 Summary	78
5 Robust State-of-Charge Estimation of Ultracapacitors for Electric Vehicles.....	79
5.1 Motivation.....	79
5.2 UC Modelling and Characterization	81
5.2.1 Model validation in the HPPC test.....	81
5.2.2 Model characterization.....	82
5.3 H -infinity Observer for UC SOC Estimation.....	84
5.4 Experimental Validation and Discussion	88
5.4.1 Validity of the proposed H -infinity observer	88
5.4.2 Robustness against modelling uncertainty	89
5.5 Summary	94
6 Fractional-order Modelling and SOC Estimation for Ultracapacitors	95
6.1 Motivation.....	95
6.2 Background and Fundamentals of Fractional-Order Calculus.....	97
6.3 Fractional-Order Modelling and Characterization of UCs.....	99
6.4 Fractional Kalman Filter for UC SOC Estimation.....	105
6.5 Experimental Validation	107
6.6 Summary	109

7 Multi-Objective Optimal Sizing of Hybrid Energy Storage System for Electric Vehicles.....	110
7.1 Motivation.....	110
7.2 Battery SOH Model	114
7.3 Powertrain Modelling	117
7.3.1 Powertrain configuration.....	117
7.3.2 Battery modelling.....	119
7.3.3 UC modelling.....	121
7.4 Wave-transform-based Power Split Strategy.....	123
7.5 Multi-objective Optimal Sizing of HESS	127
7.5.1 Maximum speed.....	128
7.5.2 Driving mileage	129
7.5.3 Acceleration time	129
7.6 Summary	134
8 Conclusions and Future Work	135
8.1 Conclusions.....	135
8.2 Future Work.....	136
References	138

List of Tables

Table 1.1 Summary of model types for UC electrical behavior simulation.....	15
Table 1.2 Summary of all UC SOC estimation methods.	17
Table 2.1 Digatron BTS-600 main specification.	23
Table 2.2 ZENNIUM electrochemical workstation main specification [82].	25
Table 2.3 Maxwell K2 UC specification.	27
Table 2.4 The performed test. The green shading in the intersection cell indicates that the EIS test was performed at the given combination of temperature and SOC.	27
Table 2.5 Detailed test schedule.	28
Table 3.1 State-space representations.	53
Table 3.2 Model parameters for identification.....	54
Table 3.3 The key parameters of the genetic algorithm.....	56
Table 3.4 The pseudo code of GA for UC model characterization.....	56
Table 3.5 The derived optimal model parameters.....	57
Table 4.1 The estimation results of the EKF.	75
Table 4.2 The estimated model parameters.	75
Table 5.1 The derived model parameters under 20°C at 100% SOC.....	83
Table 5.2 Model parameters under different temperatures.	90
Table 6.1 The derived model parameters.....	102
Table 7.1 Pre-exponential factor as a function of C-rate.	116
Table 7.2 Basic vehicle parameters.....	119
Table 7.3 Main specifications of battery.....	120
Table 7.4 Main specifications of UC.	122
Table 7.5 Driving performance requirements.	129

List of Figures

Fig. 1.1 Percentage contribution of vehicle tailpipe emissions to total emissions in US in 2011 [3]...	1
Fig. 1.2 Global CO ₂ emission trend [4].	2
Fig. 1.3 The UC structure [13].	4
Fig. 1.4 Schematic of UC energy management system.	6
Fig. 1.5 Gouy-Chapman-Stern model.	11
Fig. 1.6 Equivalent circuit models.	11
Fig. 1.7 Example neuron body with multiple inputs and single output.	12
Fig. 1.8 Example of ultracapacitor fractional-order model.	12
Fig. 2.1 Configuration of the test rig.	23
Fig. 2.2 Schematic of test schedule.	27
Fig. 2.3 Pulse profile of the HPPC test.	28
Fig. 2.4 Current profile of SDP test.	28
Fig. 2.5 Static capacity test at 20°C.	29
Fig. 2.6 The average impedance magnitude of all sampled frequencies under different temperatures and SOCs.	32
Fig. 2.7 Schematic impedance spectra in Nyquist plots under different temperatures at (a) 10%SOC; (b) 50%SOC; (c) 90% SOC.	33
Fig. 2.8 Arrhenius fit to the measured impedance (at 10Hz and 60% SOC).	34
Fig. 2.9 Schematic impedance spectra in Nyquist plots with different SOC values at (a) -40°C; (b) -20°C; (c)0°C; (d)20°C; (e) 40°C.	37
Fig. 2.10 Evolution of average impedance magnitude with SOC under different temperatures.	37
Fig. 2.11 Dynamic model structure for UCs.	40
Fig. 2.12 Frequency ranges used for model identification.	40
Fig. 2.13 Model parameters at different temperatures.	42
Fig. 2.14 Measured impedance spectra and model-predicted impedance at (a) -40°C; (b) -20°C; (c) 0°C; (d) 20°C and (e) 40°C.	44
Fig. 2.15 RMS error in DST and FUDS tests with different operating conditions.	45
Fig. 2.16 Error distribution under dynamic driving-cycle tests at all temperatures.	46
Fig. 3.1 Model structure.	53
Fig. 3.2 Comparison outcomes in the HPPC test: (a) Simulated and measured voltages; (b) Maximum and mean absolute errors; (c) RMS error.	60
Fig. 3.3 Comparison outcomes in the DST test: (a) Simulated and measured voltages;	61
Fig. 3.4 Comparison outcomes in the SDP test: (a) Simulated and measured voltages; (b) Maximum and mean absolute errors; (c) RMS error.	62
Fig. 4.1 The UC model structure.	68
Fig. 4.2 The measured voltage (a) and current (b) profiles in the DST test.	73
Fig. 4.3 The evolution of the estimated model parameters in the DST test: (a) R ₁ ; (b) C ₁ ; (c) R ₂ ; (d) C ₂ ; (e) C; (f) R _s .	74
Fig. 4.4 The measured and estimated voltages in the DST test.	75
Fig. 4.5 The relative voltage error in the DST test.	75

Fig. 4.6 The measured voltage (a) and current (b) profiles in the HPPC test.	76
Fig. 4.7 The simulated and measured voltages in the HPPC test.	77
Fig. 4.8 The error between the simulated and measured voltages in the HPPC test.	77
Fig. 5.1 UC model structure.	82
Fig. 5.2 Measured and predicted impedance spectra under 20°C at 100% SOC.	83
Fig. 5.3 Schematic of the Kalman filter for UC SOC estimation. ($\hat{x}_{k k-1}$ and $\hat{x}_{k k}$ are the prior and posterior estimate of state vector at time interval k ; $P_{k k-1}$ and $P_{k k}$ are the error covariance of $\hat{x}_{k k-1}$ and $\hat{x}_{k k}$; K_k represents the Kalman gain.)	87
Fig. 5.4 Comparison of the H -infinity observer and the Kalman filter for the UC SOC estimation in the FUDS test at 20°C.	89
Fig. 5.5 UC SOC estimation result in the FUDS test at -40°C.	91
Fig. 5.6 UC SOC estimation result in the FUDS test at 0°C.	91
Fig. 5.7 UC SOC estimation result in the FUDS test at 40°C.	92
Fig. 5.8 Mean absolute errors of UC SOC estimation.	92
Fig. 5.9 Root-mean-square errors of UC SOC estimation.	93
Fig. 6.1 Fractional-order model structure.	102
Fig. 6.2 Comparison of measured voltage, fractional-order model, and dynamic model in FUDS test at 20°C.	102
Fig. 6.3 The evolution of current and SOC in FUDS test at 20°C.	103
Fig. 6.4 Impedance spectra comparison at 100% SOC at the temperatures of (a) -40 °C; (b) -20 °C; (c) 0°C; (d) 20°C; (e) 40 °C.	104
Fig. 6.5 The DST and FUDS current profiles.	108
Fig. 6.6 SOC estimates at 20°C.	108
Fig. 6.7 Estimation errors at 20°C.	108
Fig. 7.1 (a) number of cycles until EOL; (b) SOH change rate.	116
Fig. 7.2 The powertrain illustration of the example electric vehicle with HESS.	118
Fig. 7.3 EM efficiency and torque bounds.	119
Fig. 7.4 (a) Battery; (b) UC model.	120
Fig. 7.5 UDDS driving cycle power demand.	125
Fig. 7.6 <i>Harr</i> wavelet decomposition and reconstruction.	125
Fig. 7.7 Power demand for (a) battery pack; (b) UC pack.	126
Fig. 7.8 The evolution of (a) discharging C-rate; (b) battery SOH after 100 repeated UDDS cycles; with regard to the battery number.	128
Fig. 7.9 The optimization result for a UDDS driving cycle.	132
Fig. 7.10 UC SOC evolution during the UDDS driving cycle.	132
Fig. 7.11 Battery degradation with HESS and battery-only ESS during the UDDS driving cycle.	132
Fig. 7.12 The evolution of battery wear and HESS weight with regard to cost.	133

Nomenclature

Global abbreviations used in this thesis

EV	=	Electrified vehicle
BEV	=	Battery electric vehicle
HEV	=	Hybrid electric vehicle
PHEV	=	Plug-in hybrid electric vehicle
UC	=	Ultracapacitor
SC	=	Supercapacitor
EDL	=	Electric-double-layer
ESS	=	Energy storage system
HESS	=	Hybrid energy storage system
UMS	=	Ultracapacitor management system
SOC	=	State-of-Charge
SOH	=	State-of-Health
EKF	=	Extended Kalman filter
KF	=	Kalman filter
GA	=	Genetic algorithm
HPPC	=	Hybrid Pulse Power Characterization
DST	=	Dynamic Stress Test
FUDS	=	Federal Urban Driving Schedule
SDP	=	Self-designed Pulse
UDDS	=	Urban Dynamometer Driving Schedule
EoL	=	End-of-Life
ANN	=	Artificial neural network
PDE	=	Partial differential equation
ODE	=	Ordinary differential equation
RMS	=	Root-mean-squared
EIS	=	Electrochemical impedance spectroscopy

LMI	=	Linear Matrix Inequality
ARE	=	Algebraic Riccati Equation
FOC	=	Fractional-order calculus
GL	=	Grünald-Letnikov
GLD	=	Grünald-Letnikov derivative
RL	=	Riemann-Liouville
CPE	=	Constant-phase-element
DP	=	Dynamic programming
MPC	=	Model predictive control
WT	=	Wavelet-transform
NSGA	=	Non-dominated sorting genetic algorithm

1 Introduction

1.1 Background and Motivation

The number of vehicles on road has seen a huge increase due to continuously advancing manufacturing techniques (making vehicles affordable) and rising living standards since the Second World War. The overwhelming majority of the existing vehicles are powered by the Internal Combustion Engines (ICEs). They convert fossil-fuel energy into mechanical work and heat while producing environmentally-damaging emissions and greenhouse gases. This poses a huge threat to the sustainable supply of energy and environmental protection that concerns both governments and citizens around the world. Taking the US for example, nearly a third of energy consumed annually is in the transportation sector, 97% of which is petroleum [1]. Light-duty vehicles claimed 60% of this energy and 45% of the total US petroleum use in 2009 [2]. It was estimated that the daily consumption of fossil oil would reach 130 million barrels by 2030. Vehicles also account for a large proportion of the pollutant emissions: 53% of CO, 31% of NO_x, 24% of VOCs, 1.7% of PM_{2.5} in 2011, as shown in Fig. 1.1 [3]. Additionally, transportation is responsible for 31% of the total CO₂ emission in 2009 [2]. The global CO₂ emission trend in recent years is shown in Fig. 1.2 [4].

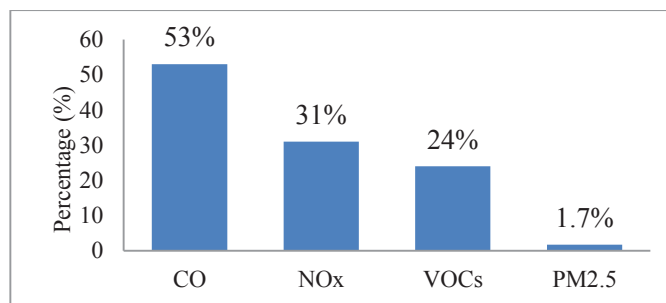


Fig. 1.1 Percentage contribution of vehicle tailpipe emissions to total emissions in US in 2011 [3].

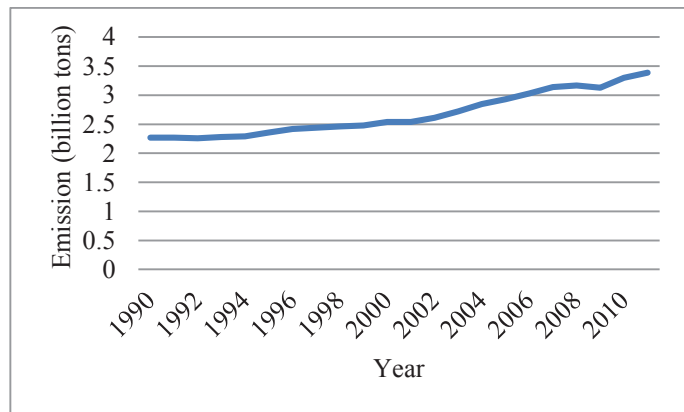


Fig. 1.2 Global CO₂ emission trend [4].

In order to ease oil-depleting, global warming and environmental protection issues, electrified vehicles, including Battery Electric Vehicles (BEVs), Hybrid Electric Vehicle (HEVs) and Plug-in Hybrid Electric Vehicles (PHEVs) represent a promising alternative to the ICE vehicles to expedite a paradigm shift towards a sustainable transportation. Generally speaking, EVs can make use of the electricity stored or generated on board to power the electrical drivetrain. The electricity can be generated from renewable sources including nuclear power, solar power, wind power, and hydro power, as well as other energy sources. The penetration of EVs will help to spur a synergic development of the renewable energy sector [5].

There is a noteworthy distinction in powertrain configuration between an electric vehicle and a conventional ICE vehicle, that is, an energy storage system (ESS) is employed with the purpose of storing electricity for the future use. The energy density in these storage devices is somewhat less than the energy density of petrol or diesel fuel. The exploration for a sufficient vehicular ESS poses a formidable challenge, since electric vehicles simultaneously demand sufficient amounts of energy and power, while ensuring safe, reliable, and durable operation under demanding and unpredictable driving conditions. Many potential energy

storage devices have been reported and analyzed in the literature [6]. Of all the mentioned devices, Li-ion batteries provide the best performance with regards to specific energy, while exhibiting no memory effect, offering long cycle-life and having low self-discharge rate when idle [7]. These properties, as well as decreasing cost, have established Li-ion batteries as a leading candidate for the next generation of automotive and aerospace applications [8]. However, a Li-ion battery-based ESS suffers from several limitations in terms of delivering high power transients due to its comparatively lower power density. A possible solution to the problem is that the vehicle may deploy more batteries than is strictly necessary; or the system may be highly stressed by high-power delivery in harsh accelerations and decelerations. Additionally, high-load conditions are a tough challenge for an energy management system to effectively tackle due to thermal issues, which have an adverse effect on battery life. The situation is especially severe when the energy storage system is exposed to high-rate charge and discharge [9][10]. Therefore, it is necessary to seek for an alternative feasible solution to offset the drawback of poor power density.

Ultracapacitors (UCs), also known as supercapacitors (SCs) or electric double-layer capacitors (EDLCs), are electrical energy storage devices that can offer higher power density and efficiency, and much longer cycle-life than electrochemical batteries [11]. UCs are characterized by fast charging time and wide operating temperature range. These characteristics have made UCs a promising candidate in a wide range of applications such as uninterruptible power supplies, electric vehicles and personal cell-phones [12]. The electric double-layer (EDL) phenomenon was firstly described by Helmholtz in 1853, and patented by Becker (General Electric Company) in 1957, who used porous carbon material with high specific area as electrodes for double-layer structure formation. The Nippon Electric

Company (or NEC) developed and licensed an UC product as a memory backup device that marked the first commercial application in 1971. Structurally, the UC consists of two electrodes, a membrane separator, and associated electrolyte, as shown in Fig. 1.3 [13]. The two electrodes are insulated by the membrane separator and impregnated with the electrolyte. The membrane separator only permits ion mobility but prevents electric contact. UCs store electrical energy mainly through the formation of the so-called double-layer capacitor structure at the interface between the electrodes and the electrolyte. This energy storage mechanism involves no chemical phase or composition changes, apart from the fast and reversible Faradaic reactions existing on the electrode surfaces, which also contribute to the total capacitance and is termed as pseudo-capacitance. The characteristic of electrostatic charge transfer results in a high degree of recyclability. Compared to conventional capacitors, the high capacitance of UCs originates from the high specific area of the electrodes, which are largely determined by the used electrode materials and their physical properties (e.g. conductivity and porosity) [14].

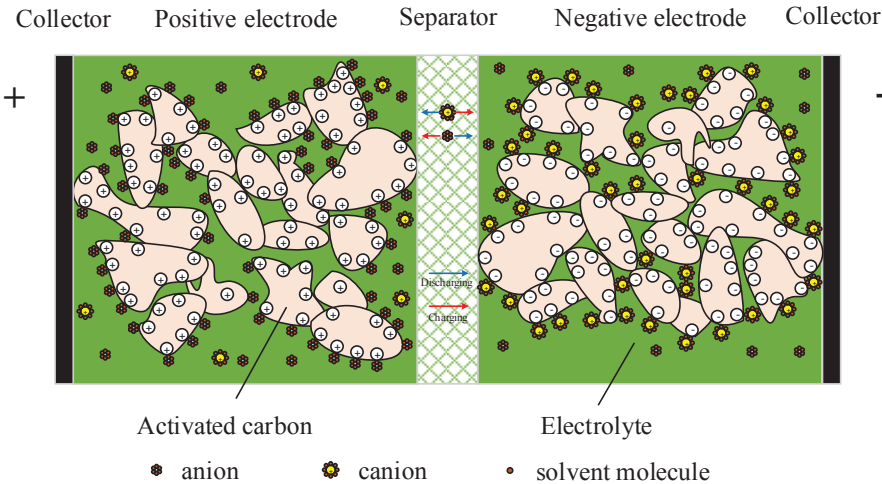


Fig. 1.3 The UC structure [13].

Taking advantages and limits of both batteries and UCs into consideration, the coordinated use of batteries and UCs as a hybrid energy storage system (HESS) has gained increasing interest from both academia and industry [15][16][17][18][19], since the HESS can store sufficient energy and also provide sufficient transient power at a reasonable cost. This contributes to better driving performance compared to the individual use of either energy source independently. During practical operation of an HESS, the battery pack is assigned to supply a near constant power to fulfil the average power demands while making the UCs work as a power buffer to meet the dynamic power demands. Such a power allocation allows the battery to avoid working under high-load and frequent high-rate charge-discharge operations, which will extend its cycle-life [20].

Due to low energy density and cell voltage of a UC, UC packs are always formed through series-parallel connections of cells. A capable ultracapacitor management system (UMS) is therefore necessary to ensure safe, efficient and reliable operation of such UC pack, whose functionalities are illustrated in Fig 1.4. The main tasks of UMS are listed as follows:

- (1) Voltage monitoring: Realize real-time supervision of cell voltage to prevent over-charge/over-discharge.
- (2) Current monitoring: Realize real-time supervision of cell current to prevent overcurrent.
- (3) Thermal management: Realize real-time supervision of cell temperature and maintain the temperature in a reasonable range through appropriate control of cooling or heating systems.

(4) State estimation: Based on the detected voltage, current and temperature information, realize real-time State-of-Charge (SOC) estimation and correspond it to the control unit for power control.

(5) Equalization management: Based on the voltage and SOC information, realize the cell equalization within the pack.

(6) Safety protection: Trigger the protection mechanism when detecting abnormal voltage, current, temperature or SOC.

(7) Power coordination: On the basis of SOC information, realize power coordination between the battery and UC packs when a HESS is deployed.

To ensure efficient, reliable and safe operations of UC systems, numerous challenges including modelling and characterization, and SOC estimation, should be addressed.

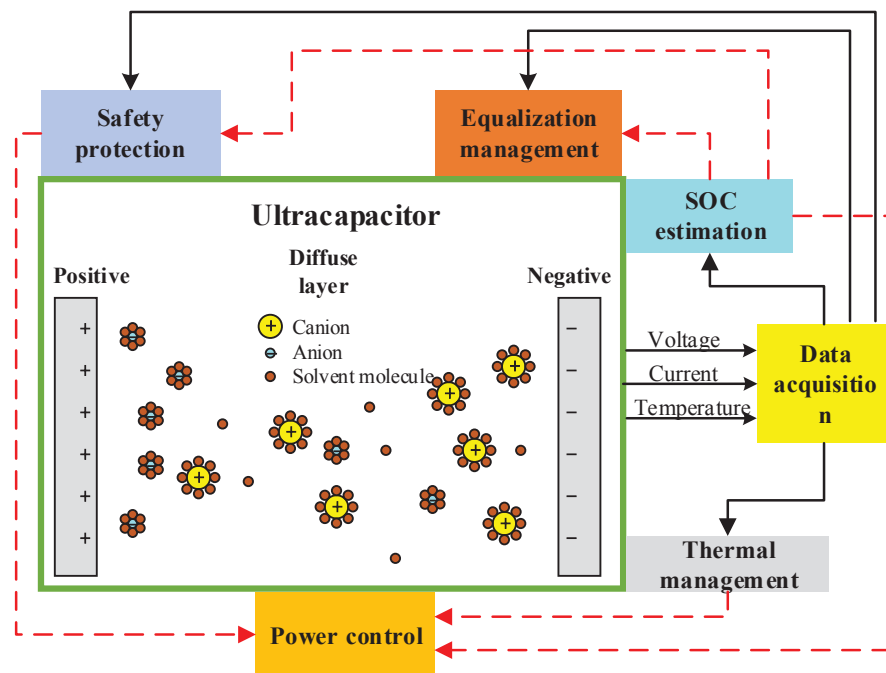


Fig. 1.4 Schematic of UC energy management system.

1.2 Literature Review

1.2.1 Ultracapacitor models

Modelling of UCs is essential for design prediction, state monitoring and control synthesis. Numerous UC models have been proposed in the literature for different purposes including electrochemical models, equivalent circuit models, intelligent models and fractional-order models.

1.2.1.1 Electrochemical models

Helmholtz discovered the electric-double-layer (EDL) phenomenon and described it with a model in which all the charges were assumed to be adsorbed at the electrode surface [21]. This is identical to the conventional dielectric capacitor structure [22]. Gouy [23] and Chapman [24] further modified the Helmholtz model to account for the ion mobility in the electrolyte solution as a result of diffusion and electrostatic forces. Boltzmann distribution equation was utilized to analytically depict the relationship between the ionic concentration and the local electrical potential in the diffuse layer. Stern combined the Helmholtz model and the Gouy-Chapman model, and divided the EDL into two characteristically distinct layers, i.e., the Stern layer (Helmholtz layer) and the diffuse layer (Gouy-Chapman layer), as shown in Fig. 1.5. The Stern layer takes care of the specific absorption of the ions on the electrode surface whilst the diffuse layer serves to incorporate the Gouy-Chapman model [25]. The total capacitance of EDL can be treated as the series connection of the Stern layer and the diffuse layer capacitances. However, unrealistic ion concentration value may be reached by deriving the Poission-Boltzmann (PB) equation; this model treats the ions as point charges by ignoring their physical size, but the point-charge assumption is only valid for low ion concentration

and low electrical potential [26][27]. Bikerman [28] reformulated the Poission-Boltzmann model by incorporating the influence of finite ion size under equilibrium conditions where the anions and cations in the electrolyte were assumed to have different size with identical valence. Verbrugge and Liu [29] proposed a one-dimensional one-domain mathematical model based on the dilute-solution theory and porous electrode analysis, where the UC was regarded as a continuum entity with homogeneous and isotropic physical properties. Allu *et al.* [30] further extended it into a three-domain model based on the uniform formulation of electrode-electrolyte system. This illustrated the benefits of capturing the irregular geometric configuration, charge transport and related performance in higher dimensions, and introducing spatio-temporal variations, anisotropic physical properties and upstream parameters into simulations. Wang and Pilon [31] developed a three-dimensional (3D) model for UCs, which simultaneously considers 3D electrode morphology, finite ion size and field-dependent electrolyte dielectric permittivity. A general set of boundary conditions were derived to describe the Stern layer behaviour without simulating it in the computational domain.

Generally, electrochemical models have high accuracy but low calculation efficiency, since they are able to capture the real reaction process inside UCs at the expense of coupled partial differential equations (PDEs). This hinders their applications in embedded systems for real-time energy management and control.

1.2.1.2 Equivalent circuit models

Equivalent circuit models which employ the parameterized *RC* (resistor-capacitor) networks to mimic the electrical behavior of UCs have the properties of simplicity and ease of implementation. This is due to the use of ordinary differential equations (ODEs), which

have proved popular. The most used equivalent circuit models are shown in Fig. 1.6. The simplest equivalent circuit model is an equivalent resistor connected with a capacitor in series [32]. Spyker and Nelms [33] added another parallel resistor that accounts for the self-discharge phenomenon to form the classical equivalent circuit model. But, this model can only adequately represent the UC dynamics over a time scope of several seconds, which significantly limits its practical applicability. Targeting power electronic applications, Zubieta *et al.* [34] developed a model that comprises three *RC* branches, i.e., immediate branch, delayed branch and long-term branch. Each branch captures UC characteristics on a distinct time-scale. The nonlinear capacitance was incorporated into the immediate branch as a voltage-dependent capacitor that is connected in parallel with a constant capacitor. The parameters of three branches were subsequently extracted through observation of the terminal voltage evolution during a high constant-current charging process. Analogous model representations were devised by other researchers but using different characterization methods [35][36][37][38]. In particular, Liu *et al.* [39], quantitatively investigated the temperature impact on the model parameters, and synthesized temperature-dependent three-branch model. Zhang *et al.* [40] exploited a variable resistor to characterize the self-discharge process on the basis of three-branch model, which claimed to have higher model accuracy for the use of self-powered wireless sensors. Buller *et al.* [41] proposed a dynamic model using the electrochemical impedance spectroscopy (EIS) technique in the frequency domain. This model was composed of a series resistor, a bulk capacitor and two parallel *RC* networks. Musolino *et al.* [42] aimed to describe the full-frequency-range behavior of a UC. They used the dynamic model to replace the immediate branch of the three-branch model, and introduced a parallel leakage resistor to form the combined UC model. Gualous *et al.* [43] conducted an

experimental study of UC series resistance and capacitance variations with temperature, and synthesized an equivalent circuit model with temperature-dependent parameters. Rafika *et al.* [44] also presented an equivalent circuit model with 14 RCL elements whose values are functions of voltage and/or temperature and are estimated through the EIS methodology. In order to capture the distributed capacitance and electrolyte resistance determined by the porous electrodes, the transmission line model was introduced. This takes transient and long-term behavior into consideration with variant model complexity, relying on the number of employed *RC* networks [45][46]. Each *RC* network is assigned to delineate capacitance and resistance of each pore distribution in electrodes. Generally, the model accuracy increases with more *RC* networks, but this is at the expense of computational efficiency. Rizoug *et al.* [47] employed a hybrid method composed of a frequency approach and a temporal approach to characterize the transmission line model. Dougal *et al.* [48] used a numerical method to realize automatic model order selection of the transmission model based on the simulation time step, which gives better modelling flexibility and computational efficiency.

Equivalent circuit models are derived from empirical experience and experimental data under certain conditions. This renders it inadequate for represent the UC dynamics under wide-range conditions, thus giving rise to model mismatch issues. Also, their parameters and states lack physical representations so that no internal information is explicitly available. However, the structural simplicity and decent modelling accuracy make them well-accepted for real-time energy management synthesis.

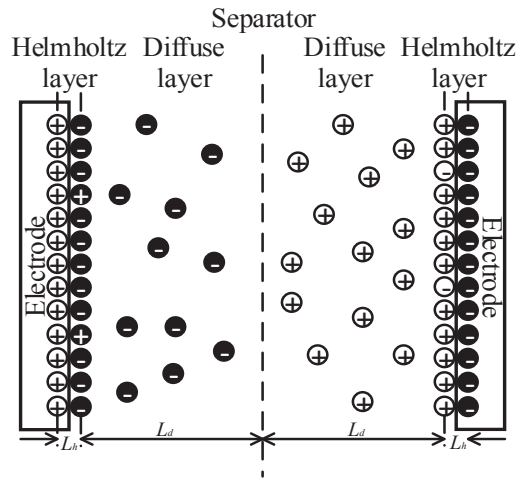


Fig. 1.5 Gouy-Chapman-Stern model.

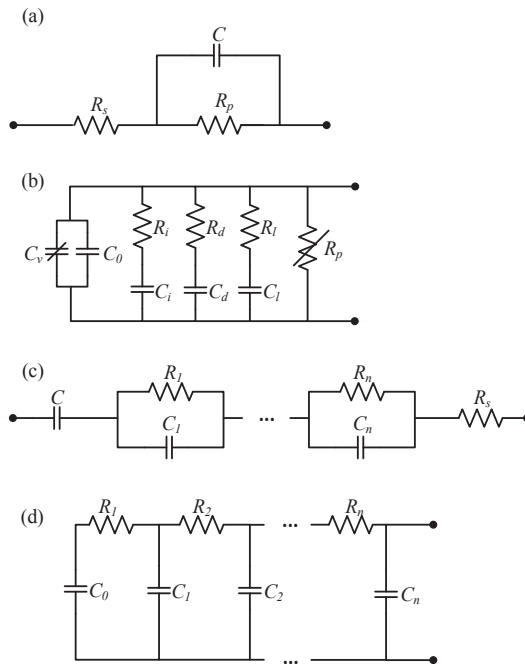


Fig. 1.6 Equivalent circuit models.

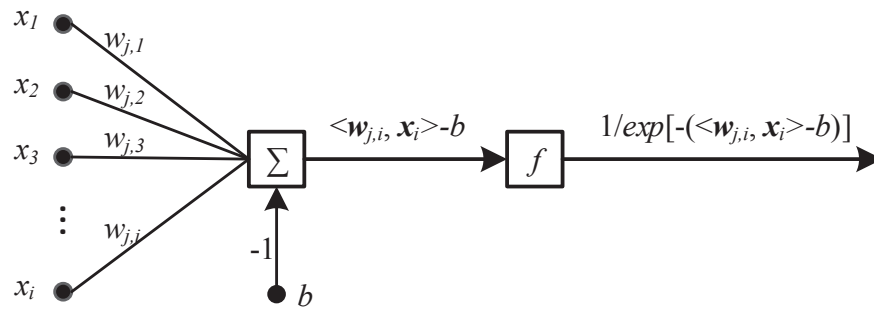


Fig. 1.7 Example neuron body with multiple inputs and single output.

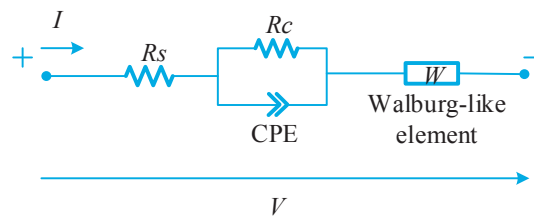


Fig. 1.8 Example of ultracapacitor fractional-order model.

1.2.1.3 Intelligent models

Intelligent modelling techniques, such as artificial neural network (ANN) and fuzzy logic, have been successfully used to predict the performance of energy storage systems including batteries and UCs [49][50]. Fig. 1.7 illustrates an example neuron body which processes the input signals and returns the result. These intelligence-based methods have the capability of depicting the sophisticated nonlinear relationship between the performance and its influencing factors without a detailed understanding of involved mechanisms. A large quantity of rich and reliant training data is necessary for ensuring model accuracy and generality. These unique features have led to the widespread use of intelligent methods for both UC design and performance prediction. For example, Farsi *et al.* [51] proposed an ANN model to examine the impacts of several intrinsic characteristics on the UC performance in

terms of utilization, energy density and power density. The model inputs were crystal size, surface lattice length, exchange current density of the active material and cell current, which are critical parameters for UC prototype design. The findings can provide prudent insights for enhancing UC performance during laboratory design process. Wu *et al.* [52] presented a dynamic model for UC behavior simulation, in which the model parameters were predicted through an established ANN model. The inputs of the ANN model were terminal voltage and temperature while the outputs were the two influencing factors put into model parameter calculation. Eddahech *et al.* [53] used a one-layer feed-forward artificial neural network to represent the behavior of UCs as a complex function of current rate, temperature, chemistry and history. The model fidelity was validated through power-cycling with the resulting model further harnessed for voltage control purpose. Weigert *et al.* [54] established an SOC estimator using ANN for a battery-UC hybrid energy storage device. Marie-Francoise *et al.* [55] also used the ANN model to track the voltage with current, temperature and voltage variations. The ANN network was claimed to provide useful information on the transient behaviours of a UC taking thermal influences into consideration.

1.2.1.4 Fractional-order models

Recently, fractional-order models have gained interest in the area of energy storage devices, including both batteries and UCs [56][57]. Fig. 1.8 illustrates an example of a fractional-order model, which comprises of a series resistor, a parallel resistor, a constant-phase-element (CPE) and a Warburg-like element. In most cases, fractional-order models exhibit a better capability of fitting experimental data with fewer model parameters, in contrast to their integral-order counterparts. For example, Riu *et al.* [58] introduced a half-order model for UCs that dramatically reduced the model order while retaining certain

accuracy. However, the fixation of fractional differentiation order inevitably restricted the model accuracy. Martynyuk and Ortigueira [59] presented a fractional-order model of an electrochemical capacitor, in which the model parameters were estimated by least-squares fitting of the impedance data. In addition, Bertrand *et al.* [60] deduced a non-linear fractional-order model from a set of linear equations as a result of frequency analysis of UCs, where the model parameters were also estimated in the frequency domain. In a similar fashion, Martín *et al.* [61] proposed a Havriliak-Negami function-based model that achieved excellent fitting for the whole frequency interval. These attempts invariably applied frequency-based impedance data to model identification. Such treatment has proved to be reliable in a specialized laboratory environment, since the impedance spectra of UCs can be steadily and precisely obtained over a range of frequencies via the EIS technique. A considerable model mismatch may occur when these laboratory-calibrated models are used under uncertain conditions. Alternatively, Dzieliński *et al.* [62] proposed a fractional-order model for UCs whose parameters were identified based on time-domain data collected through a constant-current charging test. Freeborn *et al.* [63] estimated the impedance parameters of a fractional-order UC model by voltage step response rather than direct impedance measurement. Nonetheless, the model precision may be severely compromised when the UC is exposed to varying loading conditions in real-time application conditions, since the model parameters are highly sensitive to variable conditions. Gabano *et al.* [64] introduced a fractional continuous LPV model, which was synthesized from a set of locally identified LTI fractional impedance models through a cubic spine interpolation technique. The operating-voltage-dependent nonlinear behavior of UCs was considered, attaining higher modelling accuracy

and robustness. The four model categories for simulating the electric behavior of UCs are summarized and compared in Table 1.1 for reference.

Table 1.1 Summary of model types for UC electrical behavior simulation.

Category	Subclass	Upside	Downside	Examples
Electrical behavior	1). Electrochemical models	Description of inside physical-chemical reactions; High possible accuracy	Heavy computation; Immeasurability of some parameters	[21]-[31]
	2). Equivalent circuit models	Moderate accuracy; relatively easy implementation and model identification	Absence of physical meanings; susceptible to aging process	[32]-[48]
	3). Intelligent models	Good modelling capability; disclosure of the influencing factors to desirable model output	Sensitive to training data quality and quantity; poor robustness	[50]-[55]
	4). Fractional-order models	Better capability to fit experimental data; few model parameters	Heavy computation;	[58]-[64]

1.2.2 State-of-Charge estimation

Accurate SOC estimation under the presence of model uncertainty and noise is critical for ensuring reliant, efficient and resilient operation of UC systems. A precise metering of the SOC can allow an energy management controller to make better use of the UC power potential without incurring detrimental overcharging, over-discharging or catastrophic failure [65].

The UC SOC is more directly related to its terminal voltage when compared to rechargeable batteries. This is the result of the unique electrostatic energy storage characteristic. However, the reading of terminal voltage for SOC indication may lead to a considerable error from the true SOC, due to the existence of self-discharge phenomenon (charge redistribution and leakage current) and side-effect reactions (pseudocapacitance) inside the UC. Thus, there has been work exploring improved solutions, which mainly use intelligent models or model-based state observers. For example, Zhang *et al.* [66] established a neural network model for UC residual capacity estimation for EV applications. The current, voltage and temperature are considered as the influencing factors and formulated as the ANN inputs, and the residual capacity is directly indicated as the output. Rich and reliable data collected in dynamic tests were used to train and validate the proposed ANN model. Nadeau *et al.* [67] synthesized a Kalman filter for tracking the SOC based on the three-branch equivalent circuit model. The effectiveness of the proposed method was experimentally validated in a solar power application. Chiang *et al.* [68] applied the extended Kalman filter (EKF) to simultaneously obtain the SOC and temperature estimates using a combined formulation of a voltage-and-thermal-dependent equivalent circuit model and a thermal model. Yang and Zhang [69] tried to use a linear capacitance instead of the rated capacitance for estimating the UC energy, based on the UC's physical characteristics. Dey *et al.* [70] proposed an online UC SOC estimation scheme using the sliding mode methodology for a hybrid energy storage system composed of batteries and UCs. The estimation scheme included two separate state observers for the batteries and UCs. The two types of UC SOC estimation methods are summarized in Table 1.2 for reference.

Table 1.2 Summary of all UC SOC estimation methods.

Category	Subclass	Upside	Downside	Examples
SOC estimation	1). Artificial neural networks	Good nonlinear mapping; disclosure of the influences of related factors	Sensitive to training data quality and quantity; poor robustness	[66]
	2). Kalman filter-based and observer-based methods	Online and closed-loop	Relatively heavy computational burden; sensitive to precision and robustness of battery model	[67][68][70]

1.2.3 Motivation and research aims

1. The knowledge of UC impedance can help develop accurate models and effectual energy management strategies. Nevertheless, it is variable, and strongly influenced by several factors such as thermal conditions and SOC. However, the quantitative investigation of these impacts on UC impedance is constantly absent. Therefore, one of primary purposes is to thoroughly revealing these effects, providing quantitative reference for energy management synthesis.

2. Equivalent circuit models have simplicity and high accuracy relative to other modelling methodologies, and many model structures have been reported in the literature for different applications. However, there is lack of comparative study of these models for EV applications. This study aims to evaluate and compare the state-of-art equivalent circuit models in the contest of EV applications, and identify the optimal model structure, which lays the foundation for SOC estimation.

3. Equivalent circuit models are lumped models that are derived based on the experimental data. Along with aging, the model parameters endure lasting and slow variations, which necessitates periodical model parameter updates. Another research objective is to develop an enabling model parameter estimation scheme, which can be implemented in real time.

4. SOC estimation is critical for maximizing the UC potential, but it faces formidable challenges including dramatic variation and varying working conditions. Traditional SOC estimation methods, typically KF-based methods, exhibit poor robustness towards model uncertainty as a result of aging and/or changing working conditions. Thus, it is meaningful to search for new SOC estimation scheme to accommodate this issue.

1.3 Contributions and Organization of the Thesis

1.3.1 Intellectual contributions

The main contributions of this research are summarized as follows:

1. A special test rig for UC characteristic investigation was purposely established in the laboratory. A test procedure was put forward to collect test data. Numerous tests were conducted on this test rig, including capacity calibration, impedance investigation under different temperatures and SOCs, and dynamic cycling under standard driving environments and disparate temperatures, resulting in a wide-ranging UC database.

2. The impedance characteristics of a commercial UC are analyzed under different temperatures and SOC values. In particular, the coupling effect between the temperature and SOC is illustrated, and the high-efficiency SOC window is highlighted.

3. For UC modelling, three commonly used equivalent circuit models are systematically examined in terms of model accuracy, complexity and robustness in the context of EV applications. The GA is employed to extract the optimal model parameters based on the Hybrid Pulse Power Characterization (HPPC) test. The performance of these models is then evaluated and compared by measuring the model complexity, accuracy, and robustness against “unseen” data collected in the Dynamic Stress Test (DST) and a self-designed pulse (SDP) test. The validation results show that the dynamic model has the best overall performance for EV applications.

4. Online parameter identification of UC models is researched. It is proposed that the extended KF can be used to recursively estimate the model parameters using the DST dataset,

in which the dynamic model is used to represent the UC dynamics. The effectiveness and robustness of the proposed method is validated using another driving cycle database.

6. A novel robust H -infinity observer is presented in order to realize the SOC estimation of a UC in real time. In comparison to the state-of-the-art KF-based methods, the developed robust scheme can ensure high estimation accuracy even without prior knowledge of the process and measurement noise statistical properties. More significantly, the H -infinity observer proves to be more robust/tolerant to modelling uncertainties arising from the change of thermal conditions and/or cell health status.

7. A novel fractional-order model is proposed in order to emulate the UC dynamics. Relative to integer-order models, the fractional-order model has the merits of better model accuracy and fewer parameters. The novel fractional-order model consists of a series resistor, a CPE, and a Warburg-like element. The model parameters are optimally extracted using the genetic algorithm (GA), based on the time-domain data acquired through the Federal Urban Driving Schedule (FUDS) test. By means of this fractional-order model, a fractional KF is synthesized to recursively estimate the UC SOC. Validation results show that the proposed fractional-order modelling and state estimation scheme is accurate and outperforms the current practice based on integral-order techniques.

8. An optimal HESS sizing method using a multi-objective optimization algorithm is presented, with the overarching goal of reducing the ESS cost and weight while prolonging battery life. To this end, a battery state-of-health (SOH) model is incorporated to quantitatively investigate the impact of component sizing on battery life. The wavelet-transform-based power management algorithm is adopted to realize the power coordination between the batteries and UCs. The results provide prudent insights into HESS sizing with

different emphases. Finally, Chapter 8 captures the overall thesis conclusions, and presents suggestions for future research as a sequence of this thesis study.

1.3.2 Document organization

The remainder of this dissertation is organized as follows. Chapter 2 introduces the UC test rig and test implementation for UC data acquisition. A UC impedance characteristic investigation is carried out to investigate the influence of temperature and SOC. Chapter 3 systematically compares the state-of-art equivalent circuit models for UCs in terms of model accuracy, model complexity and robustness, to unseen loading conditions in the context of EV applications, resulting in the best model structure. Chapter 4 proposes an online model parameter identification method based on the previous obtained model structure. Chapter 5 uses the H -infinity observer to estimate UC SOC. This method is proved to be robust to the model uncertainty arising from aging or varying operating conditions. Chapter 6 proposes a novel fractional-order model for representing UC dynamics, and developed a fractional-order Kalman filter for SOC estimation. Chapter 7 utilizes the NSGA-2 method to realize the optimal design of an HESS, and presents a wavelet-transform based energy management scheme for power coordination.

2 Ultracapacitor Test and Its Impedance Characteristic Investigation

Unlike conventional capacitors, UCs have the advantages of high power density [71], low internal resistance [72], wide temperature window, typically $-45\sim 60^{\circ}\text{C}$ [73], excellent recyclability [74], and fast charge/discharge capability [75]. To investigate these features, it is necessary to develop a systematic and comprehensive test plan and collect test data in order to systematically investigate its characteristics.

2.1 Test Rig

In order to perform tests and establish a comprehensive database, a test rig was set up by the author as shown in Fig. 2.1. The test rig consists of a battery test system (BTS), a thermal chamber, an electrochemical workstation, a host computer, and a test UC. The main constituent facilities had been in existence in the laboratory, but arranged in an organized manner for the special experimentation purpose of this thesis study. This test rig has the ability of execute the time-domain cycling tests and the frequency-domain impedance measurement for model characterization and results verification. The BTS is used to load the UC in accordance with pre-defined loading profiles. The maximum working voltage and current are 600 V and ± 300 A, respectively. The current resolution is high, typically $\pm 20\text{mA}$, which guarantees the reliability of the measured current. The main equipment specification is listed in Table 2.1. The system has the capability of recording various quantities, such as accumulated capacity, power, current and terminal voltage with a maximum sampling frequency of 100 Hz, which is sufficiently high. The recorded data can be relayed to the host

computer through a CAN network which serves as a reliable and fast-response communication between the host computer and the cycler.

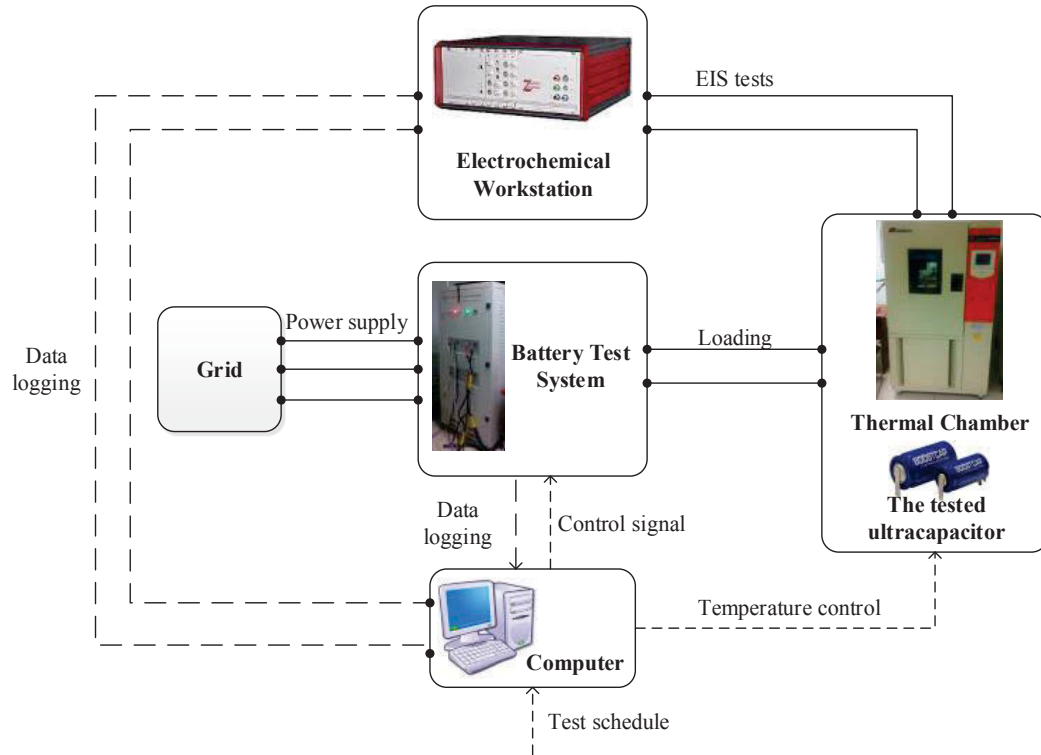








Fig. 2.1 Configuration of the test rig.

Table 2.1 Digatron BTS-600 main specification.






	Charging/discharging current: -300A ~ +300A
	Charging/discharging voltage: 0V ~ 600V
	Continuous power: 80kW; Peak power: 120kW
	Current and voltage accuracy: $\pm 0.1\%$ of the scale range; Current resolution: $\pm 10\text{mA}$
	Charge/discharge switch time: $< 20\text{ms}$ (+10% ~ +90% current scale)
	Current rising/falling time: $< 10\text{ms}$ (+10% ~ +90% current scale)

The thermal chamber accommodates the UC and provides the thermostatic ambience for all the tests. The temperature can be set at any point between -60°C and 150°C with the fluctuation and deviation bounded by $\pm 0.3^{\circ}\text{C}$ and $\pm 2^{\circ}\text{C}$, respectively. The electrochemical workstation is able to measure the UC impedance over a given frequency range with high precision under different temperatures and SOCs. The test frequency can range from $10\ \mu\text{Hz}$ to $4\ \text{MHz}$ with the frequency resolution of $0.0025\ \%$. The main specification is listed in Table 2.2. The host computer is used to develop the loading profiles, and store the test data fetched from the BTS and the electrochemical workstation.

The EIS technique is a well-established approach for investigating energy storage devices such as batteries and UCs [76] [77]. It provides a deep insight into the internal processes of the system by exploring the impedance characteristics under a wide range of frequencies [79]. It is implemented by injecting a small known sinusoidal current signal into the device and measuring the response voltage, or vice versa (galvanostatic or potentiostatic approach). The complex impedance can be calculated as the quotient of the detected voltage and the injected current at each sampled frequency. A Nyquist diagram is often plotted to depict the evolution of the real and imaginary parts of the impedance under the sampled frequencies. Equivalent circuit models can be further extracted by analyzing and interpreting the impedance spectra via basic circuit elements. It can be noted that the impedance changes throughout the service life of the device, where the impedance basically increases with aging [80]. One definition of the End-of-Life (EoL) of a UC is a pre-defined impedance increase with respect to its nominal start-of-life impedance. However, compared to the impedance variation caused by the temperature and SOC, the impedance varies much more slowly with aging. Therefore, it is

reasonable to first neglect the impact of aging on the UC impedance in a relatively long time scale. The aging issue needs further work, which is beyond the scope of this thesis. Generally, the electrode adhesion on the collectors recedes with time, and the availability of the ions in the electrolyte diminishes due to the electrochemical cycling, both resulting in the aging of the UC. More information is given in [81].

Table 2.2 ZENNIUM electrochemical workstation main specification [82].

 Frequency range: 10 μHz ~4 MHz; Frequency resolution: 0.0025%
 Potentiostatic impedance measurement accuracy: 1 $\text{m}\Omega$ ~ 1 $\text{G}\Omega/\pm 2\%$ 100 $\text{m}\Omega$ ~ 100 $\text{G}\Omega/\pm 2\%$
 Galvanostatic impedance measurement accuracy: 30 $\mu\Omega$ ~ 1 $\text{G}\Omega/\pm 2\%$
 Potentiostatic scanning voltage range: ± 10 V
 Current range: 1 nA ~ 2.5 A

2.2 Test Procedure

There is a wide range of UCs with different specifications available in the market. For electric vehicle applications, high-capacitance units are preferred with the purpose of increasing the energy density of the overall system. The Maxwell K2 series is selected for tests with a detailed specification listed in Table 2.3. In order to obtain the characteristics of UCs, an elaborate and implementable test schedule was developed to fully excite the test UC, as illustrated in Fig. 2.2. It comprises of a static capacity test, EIS tests, pulse tests and driving-cycle-based tests. The static capacity test serves to calibrate the capacitance of the test UC with the average value of 3 repeated tests, which is later used as the true capacitance. The EIS tests are used to acquire the UC impedance spectra under different temperature and SOC values, which helps to identify the high-efficiency SOC window. The data can also be employed to extract model parameters as the training data or to verify model accuracy as the validation data. The tests done are listed in Table 2.4. The pulse tests are the HPPC (Hybrid Pulse Power Characterization) and SDP (Self-designed Pulse) tests. The HPPC is in accordance with the FreedomCar Ultracapacitor Test Manual [83], and can excite the tested UC from its rated voltage to the exhausted state with highly dynamic pulses as shown in Fig 2.3. The profile can effectively reflect the typical loading conditions of on-board UCs in acceleration and deceleration scenarios of EVs. As shown in Fig. 2.4, the SDP profile is composed of random charging or discharging pulses, which represents the unpredictability of practical driving conditions in EVs. The driving-cycle-based tests, including DST (Dynamic Stress Test) and Federal Urban Driving Schedule (FUDES) tests, simulate the typical loading conditions of UCs during real-world driving. These tests can effectively excite the UCs and

also drive the SOC value to vary over a wide range, thus generating substantial and interesting test data. The detailed schedule is given in Table 2.5.

Table 2.3 Maxwell K2 UC specification.

Nominal capacity (F)	Rated voltage (V)	ESR _{DC} (mΩ)	Leakage current (mA)	Operating Temperature (°C)
3000	2.7	0.29	5.2	-40 ~ +65

Table 2.4 The performed test. The green shading in the intersection cell indicates that the EIS test was performed at the given combination of temperature and SOC.

T(°C)	SOC									
	10%	20%	30%	40%	50%	60%	70%	80%	90%	100%
-40										
-20										
0										
20										
40										

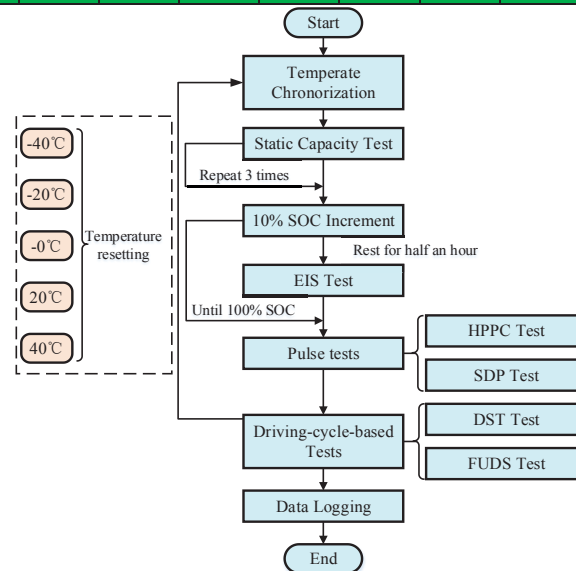


Fig. 2.2 Schematic of test schedule.

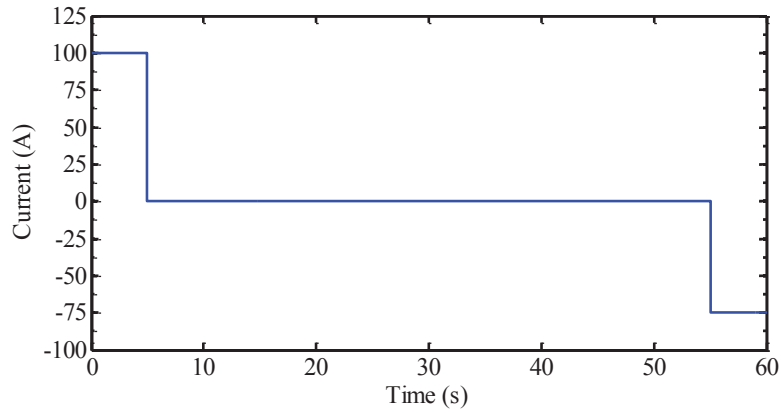


Fig. 2.3 Pulse profile of the HPPC test.

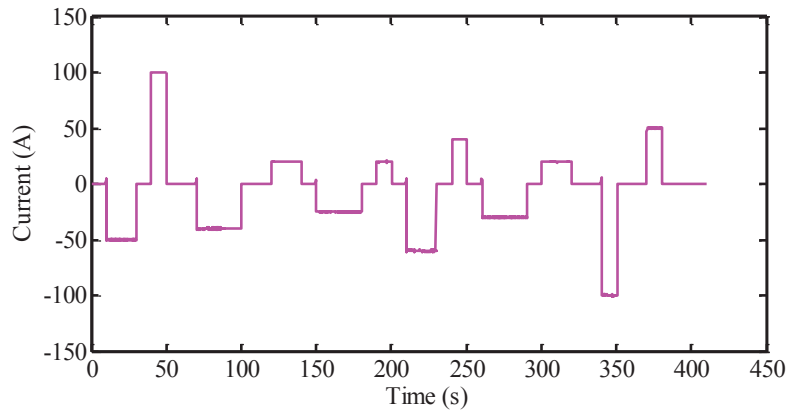


Fig. 2.4 Current profile of SDP test.

Table 2.5 Detailed test schedule.

Step1: The tested UC was discharged at a given C-rate to exhaust it, and left short-circuited for 24 hours in order to eliminate the charge redistribution effect; a current of 1 C in amps is equivalent to the charge capacity of the UC in amp-hours (i.e., for a UC capacity of 1 Ah, 1C = 1 A).

Step2: The completely discharged UC was held in the thermal chamber for 3 hours to synchronize the temperature of the tested UC with the ambient environment. The temperature of the thermal chamber was set and preheated to the pre-set value beforehand.

Step 3: The static capacity test was implemented three times to acquire the real capacity of the tested

UC in line with the Freedom Car Test Manual. The capacity was measured and recorded during the discharging of UC with a 1 C current from the rated voltage till exhausted. The average capacity of the three capacity tests was calculated and used as the real capacity in the subsequent sections. The evolution of the UC voltage during static capacity test at 20°C is shown in Fig. 2.5 for demonstration.

Step 4: The tested UC was charged with a 1 C current until the SOC value increased by 10%. The UC was then left to rest for half an hour to stabilize its terminal voltage and redistribute the charge within its internal structure.

Step 5: The EIS test was carefully imposed on the stabilized UC, where the sampled impedance spectra ranged from 10 mHz to 100 Hz with a bias voltage set at 5 mV. It is reasonable to believe that the selected frequency range covers the majority of the operating points of a UC in practical EV applications.

Step 6: The above two steps were repeated until 100% SOC was reached.

Step 7: The dynamic tests, including DST and FUDS, were performed to investigate the characteristic of the tested UC under dynamic loading profiles. These served to represent the actual loading conditions of a UC in practical EV applications.

Step 8: The above sequences were repeated for all circumstances shown in Table 2.4.

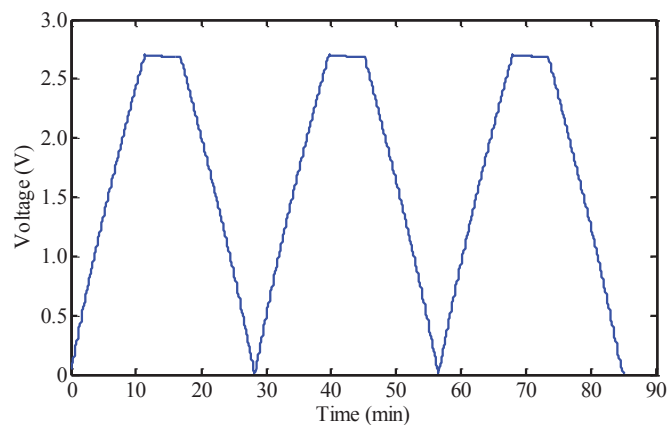


Fig. 2.5 Static capacity test at 20°C.

2.3 Investigation of UC Impedance Characteristics

The power sourcing/delivery capability of a UC is highly dependent on its impedance, to which the charge/discharge energy loss is directly proportional. As a result, a systematic examination of such impedance behaviour is critical to the development of control/management systems for ensuring a safe, reliable, and durable operation of UCs. The associated challenge is, however, serious, because the UC impedance may vary significantly with respect to dynamic operating conditions. All the existing studies merely take the open-circuit voltage variation of UCs into account, without explicitly assessing the SOC effect on impedance characteristics. In contrast to the open-circuit voltage, SOC is clearly more indicative of available energy inside UCs. Unlike conventional capacitors, the UC SOC is mostly a nonlinear function of open-circuit voltage, which often cannot be easily evaluated due to its variability with operating circumstances [40]. Hence, a direct inclusion of SOC as an influencing factor for impedance analysis and modelling could lead to a more aggressive yet effectual control scheme sufficiently leveraging the potential of a UC pack. In addition, limited levels of influencing factors were considered, incurring the absence of a precise impedance dependency upon operating conditions. The coupling impact of the temperature and SOC on the UC impedance has been constantly overlooked in previous work.

2.3.1 Temperature dependency of impedance

Using the results from the EIS tests, the dependency of the UC impedance on the temperature was studied in detail. Five temperature points were selected, covering the typical thermal operating conditions from extremely low to high temperatures. Fig. 2.6 illustrates the average impedance magnitude over all sampled frequencies under different conditions. It is

evident that the temperature significantly affects the impedance magnitude for all SOC values, especially at temperatures below 0°C. It is obvious that the impedance magnitude increases, as the temperature reduces. An exponential relationship between the impedance magnitude and the ambient temperature can be further observed. That is, the temperature dependency of the UC impedance is even greater at temperatures below 0°C. This may be attributed to the reduced solubility of the conducting salt and the increased viscosity of the electrolyte for temperatures below the freezing point. Both of these effects result in dramatically reduced electrolyte conductivity and increased impedance [81].

Fig. 2.7 shows the influence of temperature in more detail using Nyquist plots. Generally, the evolution of impedance with frequency can be divided into three distinct phases, i.e., ‘90°’ zone, ‘45°’ zone, and ‘L’ zone. The ‘90°’ zone at lower frequencies may result from the surface roughness and nonuniformity of the double-layer thickness [84]. The ‘45°’ zone is believed to involve the electrolyte resistance. Semicircles can be found in all the plots at low temperatures, one of which is marked as the ‘L’ zone in Subplot Fig. 2.7(b) for illustration. This phenomenon is due to the slower reaction rate at low temperatures, which induces a lower frequency threshold to exhibit inductive behaviour that mainly arises from the stray inductance of the current collectors and terminals, and the porous geometry of the electrodes [85]. It is apparent that the diameter of the semicircle increases with the decreasing temperature, because the lower temperatures intensify the stray inductance of the current collectors and terminals. Furthermore, the intersection of the ‘L’ zone on the real axle is always interpreted as the series resistance in equivalent circuit models [44]. The real part of the impedance principally accounts for the internal resistance of contactors and the bulk electrolyte. It drops with increasing frequency since high frequency renders a deep internal

surface in the porous electrodes inaccessible to ions, consequently reducing their contributions to the Ohmic losses. It can be further deduced that the impedance increase with the decreasing temperature becomes more pronounced at relatively low temperatures. The real part of the impedance significantly increases at -40°C , compared to the case of $+40^{\circ}\text{C}$, throughout the SOC range considered. As a consequence, the power capability of the UC would be severely compromised at low operating temperatures. Additionally, the impedance of electrochemical energy storage is always expected to have an Arrhenius dependence on its temperature [86]. Fig. 2.8 shows such Arrhenius fitting at 60% SOC and 10 Hz to quantitatively portray the temperature influence. The temperature of 0°C is noticed to be a critical point where the Arrhenius fitting coefficients alter considerably.

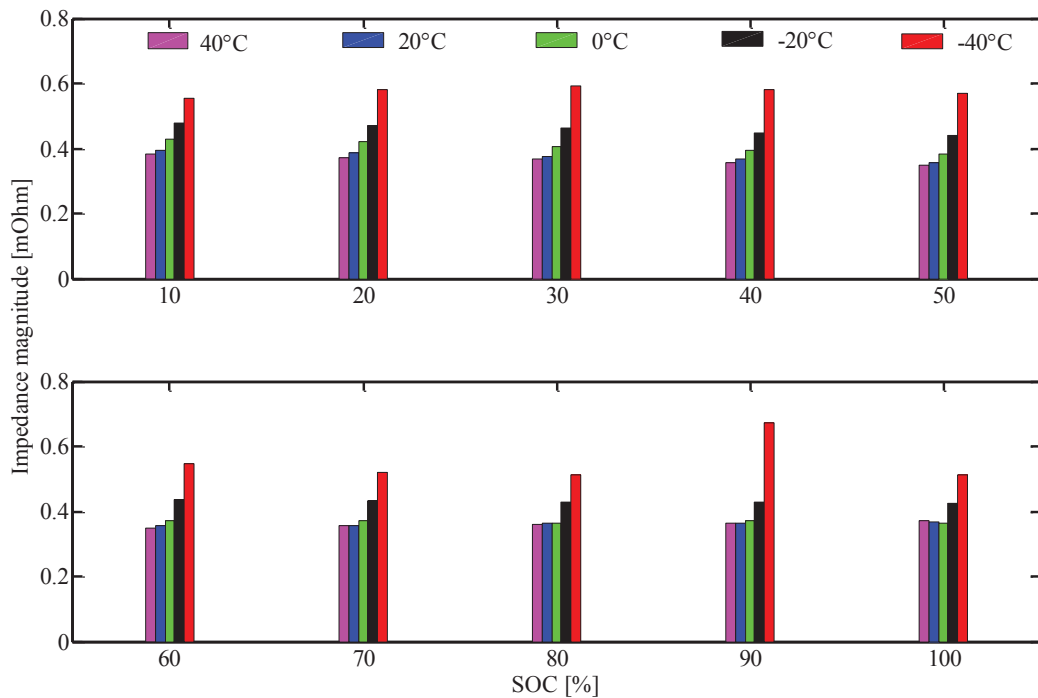


Fig. 2.6 The average impedance magnitude of all sampled frequencies under different temperatures and SOC.

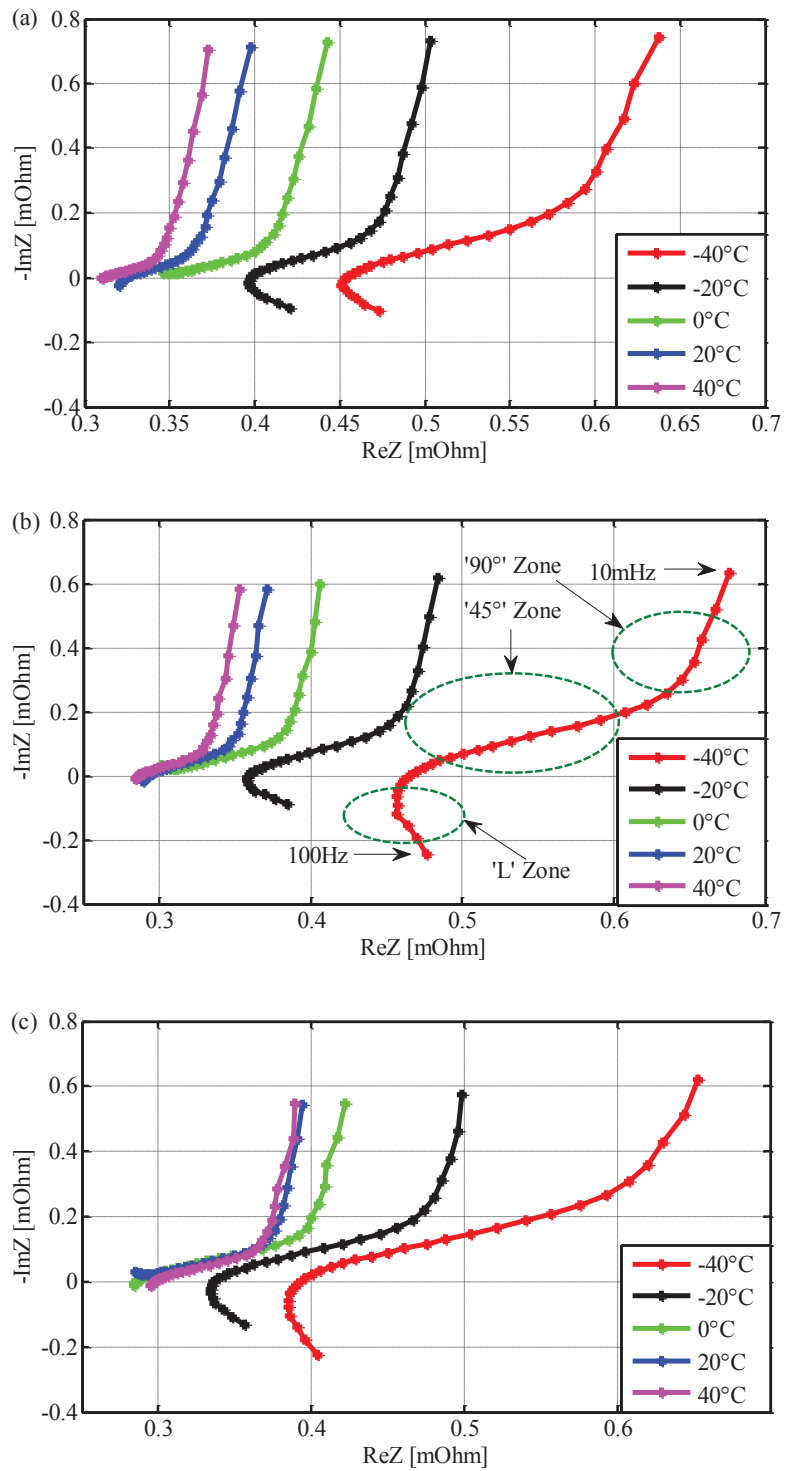


Fig. 2.7 Schematic impedance spectra in Nyquist plots under different temperatures at (a) 10%SOC; (b) 50%SOC; (c) 90% SOC.

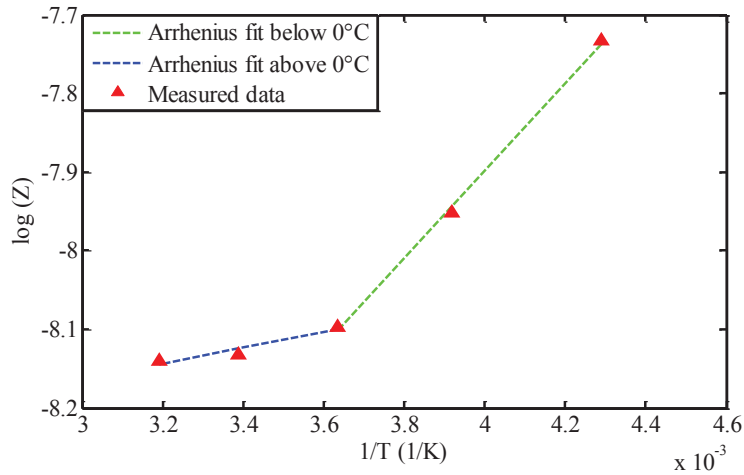
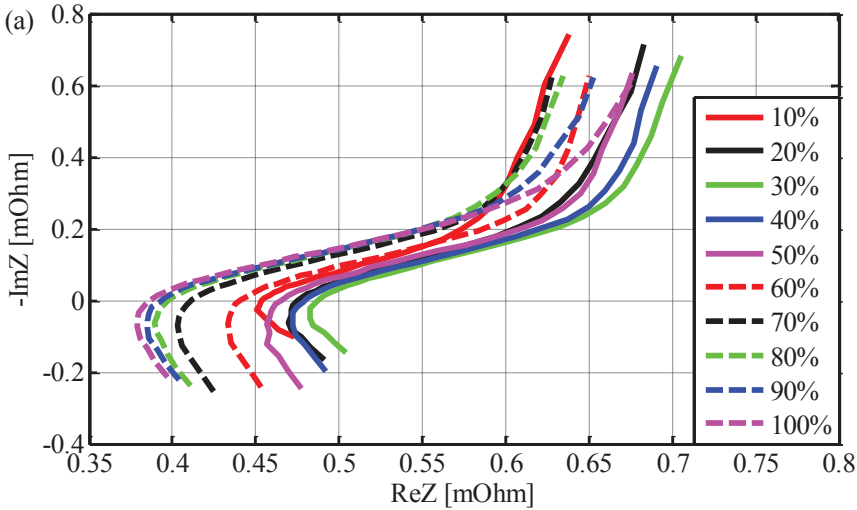


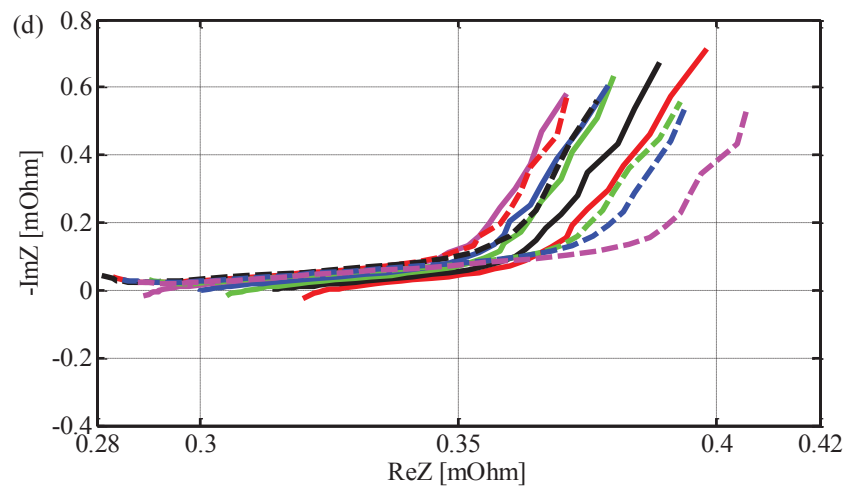
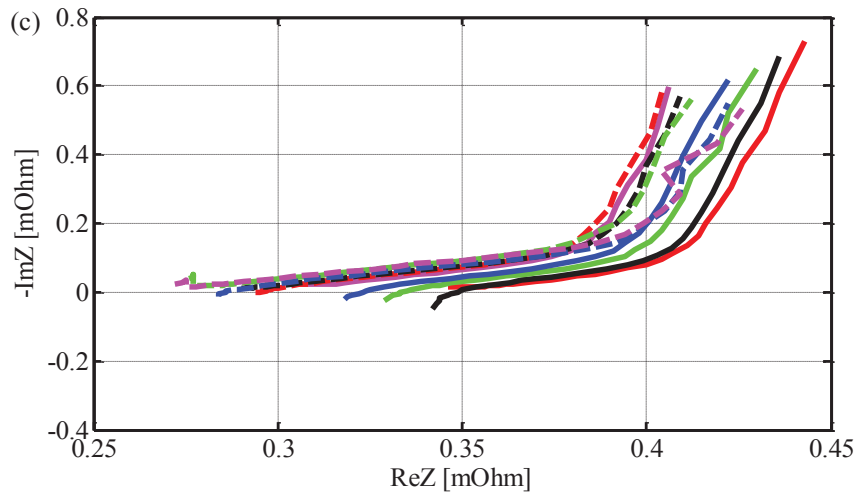
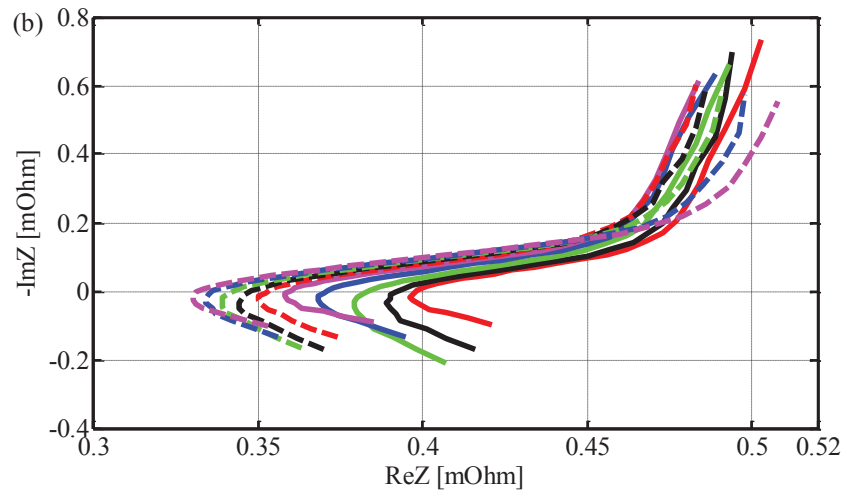
Fig. 2.8 Arrhenius fit to the measured impedance (at 10Hz and 60% SOC).

2.3.2 SOC dependency of impedance

The SOC influence on the impedance characteristics of the UC was also investigated. Fig. 2.9 shows how the impedance evolves with the SOC at all the temperatures. In contrast to the impedance variation caused by the temperature, the SOC factor seems to be less dominant. Upon a closer examination, it is noted that extreme temperatures (as low as -40°C and as high as 40°C) intensify the SOC influence, particularly in the low-frequency region. The evolution of the average impedance magnitude with the SOC is indicated in Fig. 2.10. It can be seen there is no regular change pattern. For example, at 40°C , the average impedance first reduces, as the SOC increases until about 30%, and then increases when continuing to raise the SOC. Nonetheless, in the case of -20°C , there is a monotonically decreasing impedance trajectory with increased SOC. At temperatures below 0°C , the SOC dependency even exhibits an opposite trend to that at 40°C . These observations in turn underline the coupling effect of the temperature and SOC on the UC impedance. The SOC range corresponding to low impedance at each temperature can be readily discerned from Fig. 2.10, which represents the high-

efficiency SOC window. While the impedance magnitude variation is less than $0.1 \text{ m}\Omega$, the percentage change is as high as 20% over the SOC range, which is actually substantial (as the UC impedance itself is very small, it is more judicious to consider the relative change). Owing to typical high-power applications of UCs, the 20% impedance rise probably leads to markedly increased power loss and heat generation, which ultimately requires costlier circuitry and thermal management systems, in addition to the excessive energy. Taking a 200 A charge or discharge for the UC as a rough example, it is found that operation in the low-efficiency area could increase the power loss by more than 1.5% at each time instance. This means there is a preference for the use of the high-efficiency SOC window in real applications, particularly for UC-only powered energy systems. Another supporting example is in the energy management and regenerative braking control of hybrid electric vehicles with UC energy storage [86].





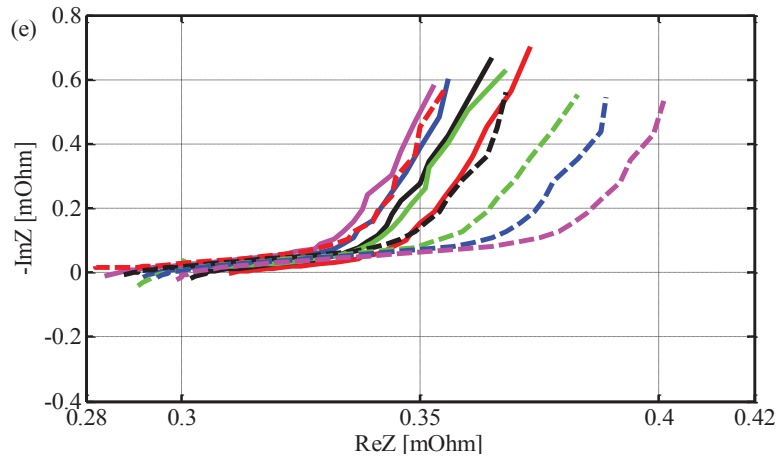


Fig. 2.9 Schematic impedance spectra in Nyquist plots with different SOC values at (a) -40°C ; (b) -20°C ; (c) 0°C ; (d) 20°C ; (e) 40°C .

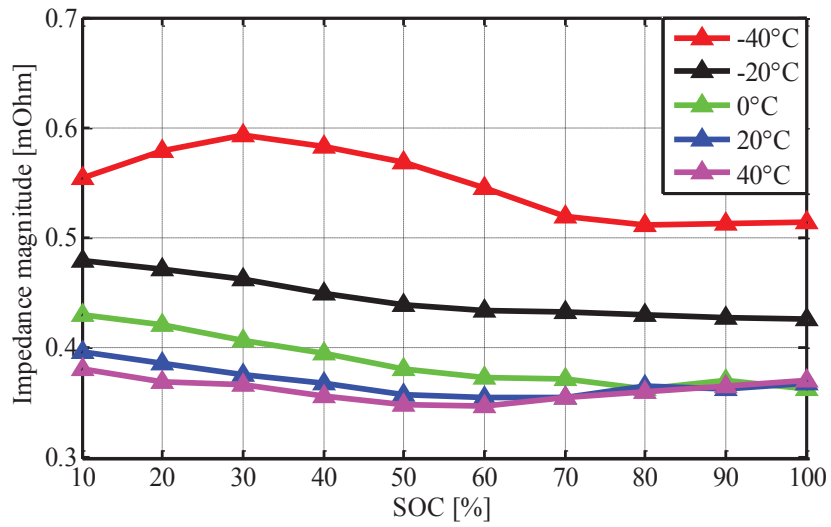


Fig. 2.10 Evolution of average impedance magnitude with SOC under different temperatures.

2.4 Dynamic Model of the Ultracapacitor

It has been well recognized that a good UC model plays an important role in energy management of advanced systems powered by UCs. To capture the UC dynamics precisely, many models have been proposed, each with its advantages and disadvantages. The EIS method has been widely used for characterization of such models. Impedance-based model parameterization enables an investigation of how UC parameters vary with dynamic operating conditions. Here, the so-called dynamic model is considered because of its high accuracy, modest complexity and inherent robustness. As shown in Fig. 2.11, the model topology consists of a series resistance, a bulk capacitor, and two resistor-capacitor (RC) networks. The series resistor represents the contact resistance between the electrodes and their metallic current collectors, and the ionic resistance in the electrolyte. The bulk capacitor accounts for the capacitance phenomenon of the tested UC. The two RC networks with different time constants aim to capture the dynamic transients arising from the charge redistribution due to the porous structure of the electrodes. According to basic circuit analysis, the impedance model can be expressed as

$$Z(j\omega) = R_s + \frac{1}{j\omega C} + \frac{R_1}{1 + R_1 \cdot j\omega C_1} + \frac{R_2}{1 + R_2 \cdot j\omega C_2} \quad (2.1)$$

where ω denotes the sampled angular frequency in the EIS tests.

The model parameters, R_s , C , R_1 , R_2 , C_1 , and C_2 are identified using the nonlinear least-squares algorithm, based on the collected EIS test data. The objective function of the algorithm is described by

$$\min_{R_s, C, R_1, R_2, C_1, C_2} \left(\frac{1}{2} \sum_{\omega_i = \omega_0}^{\omega_n} \left[\left(\text{Re}_{\omega_i, m} - \text{Re}_{\omega_i, e} \right)^2 + \left(\text{Im}_{\omega_i, m} - \text{Im}_{\omega_i, e} \right)^2 \right] \right) \quad (2.2)$$

where $\text{Re}_{\omega_i,m}$ and $\text{Im}_{\omega_i,m}$ are the real and imaginary parts of the sampled impedance of the dynamic model at angular frequency ω_i , $\text{Re}_{\omega_i,e}$ and $\text{Im}_{\omega_i,e}$ are measured values.

As shown in Fig. 2.9, the impedance becomes inductive (positive imaginary part) at relatively high frequencies, especially at temperatures below 0°C. However, UCs usually operate at fairly moderate frequencies in practice so that it is reasonable to neglect inductive effects during modelling. Therefore, the inductive parts of the EIS impedance spectra are discarded.

Fig. 2.12 shows the sampled frequencies where the measured impedance spectra are for model identification. After executing the nonlinear least-squares algorithm, the model parameters at all circumstances (wide ranges of temperature and SOC) are derived and shown in Fig. 2.13.

The comparisons of the measured and model-estimated impedance spectra at each temperature are shown in Fig. 2.14. It can be seen that the identified model can very accurately emulate the UC impedance behaviour in a major portion of frequencies. At very low frequencies, the deviation is relatively large due to the limited low-frequency characterization of the model topology. The associated improvements will be used in future work; e.g., using more advanced fraction-order modelling techniques. The model accuracies are further compared in the two dynamic driving-cycle tests; i.e., the DST and FUDS tests. The root-mean-squared (RMS) deviation from the experimentally recorded voltage is adopted as the metric of model fidelity. The RMS errors at different operating conditions are given in Fig. 2.15. It is abundantly clear that the model accuracy is, overall, high and increases with the SOC at each temperature. Furthermore, the error distribution in both tests at each temperature is shown in Fig. 2.16 where the model parameters in Fig. 2.13 were used. The outcome indicates a general error bound of 0.08 V for both tests at each temperature, thereby achieving

satisfactory model accuracy. The effects of temperature and SOC on the UC parameters (i.e., resistance and capacitance elements) are, in turn, reasonably well quantified, which is conducive to synthesizing robust UC controllers in changing operating conditions.

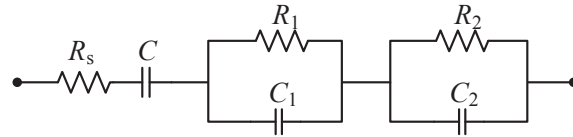


Fig. 2.11 Dynamic model structure for UCs.

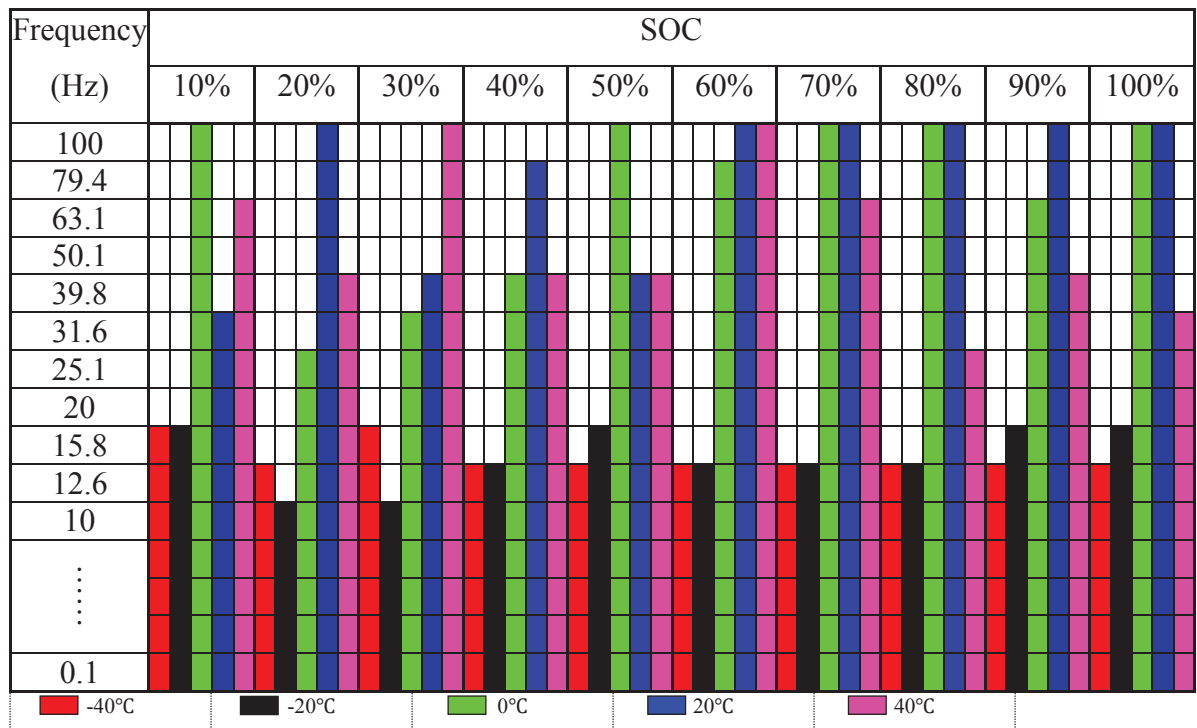
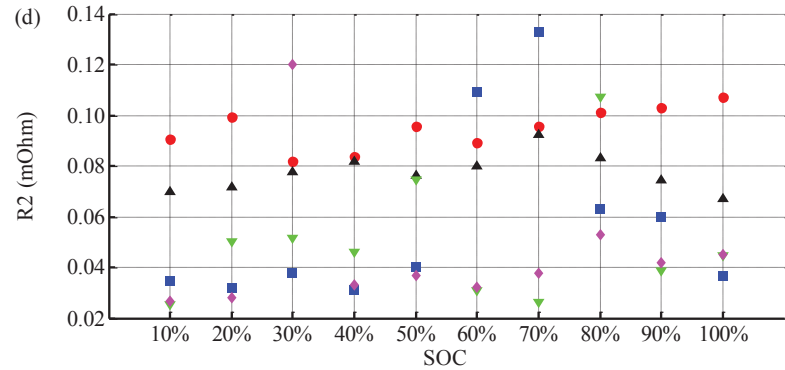
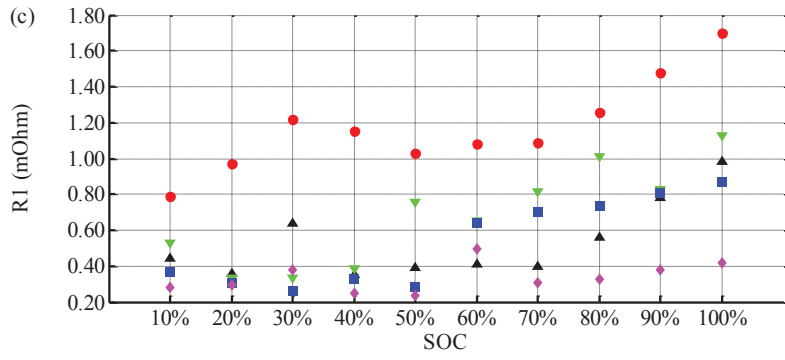
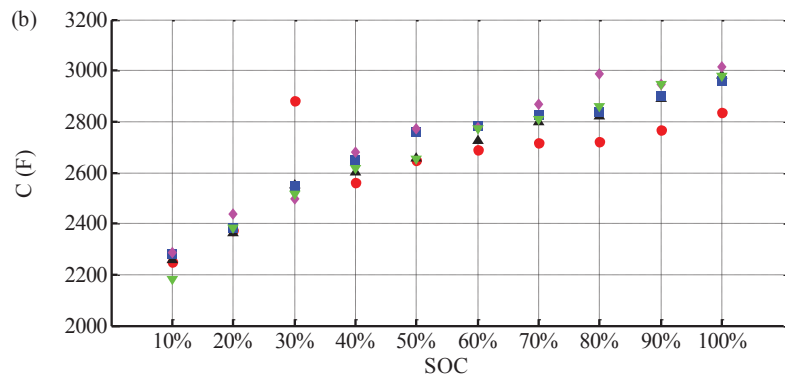
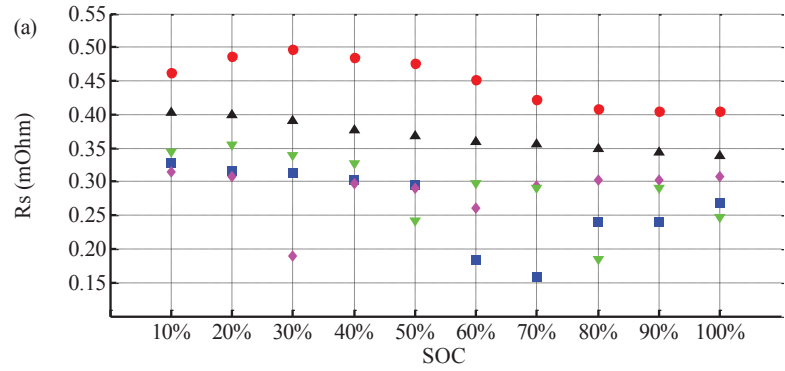


Fig. 2.12 Frequency ranges used for model identification.



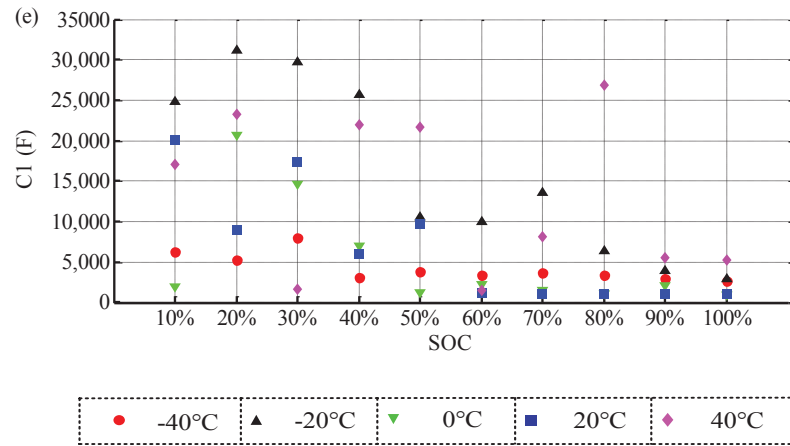
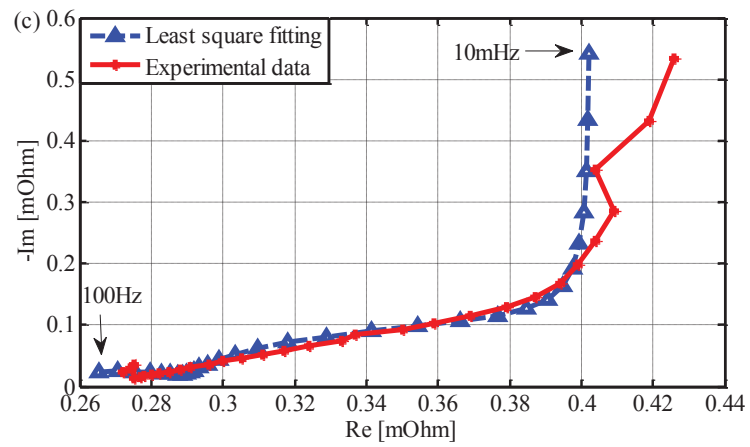
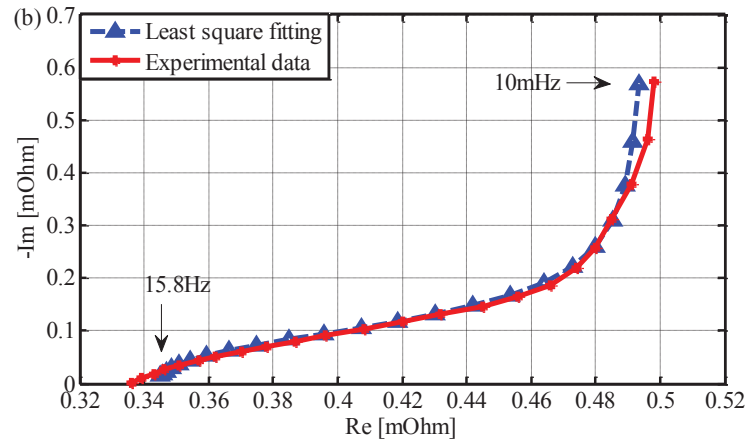
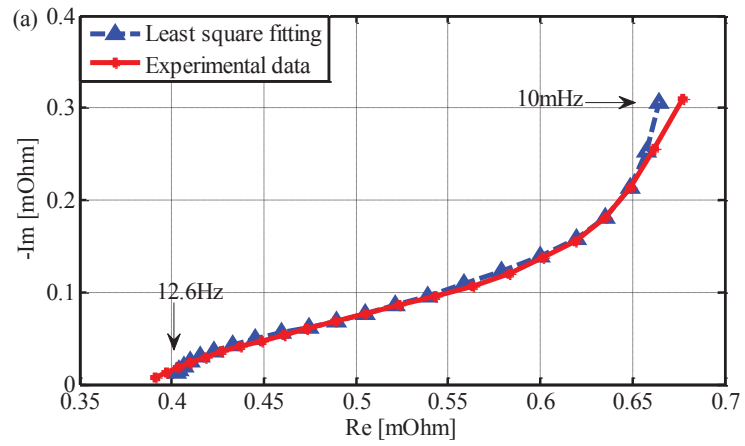


Fig. 2.13 Model parameters at different temperatures.



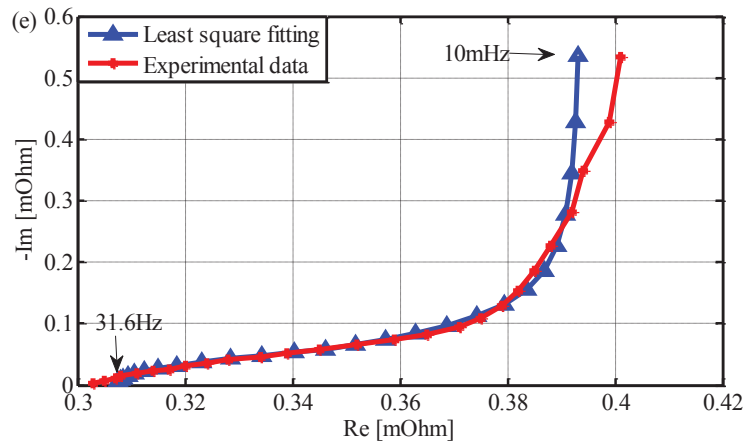
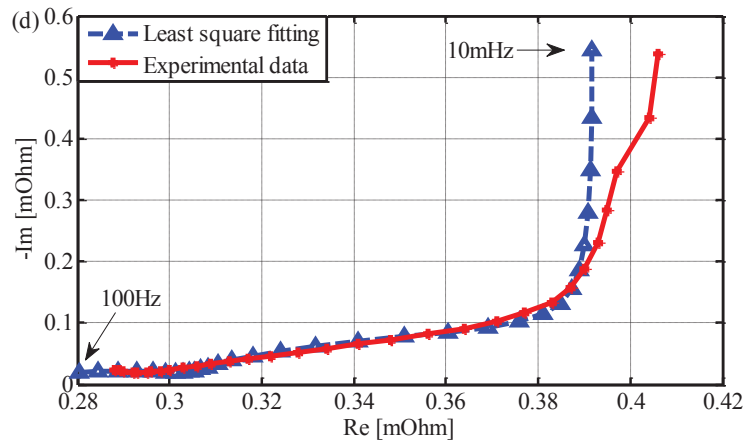


Fig. 2.14 Measured impedance spectra and model-predicted impedance at (a) -40°C ; (b) -20°C ; (c) 0°C ; (d) 20°C and (e) 40°C .

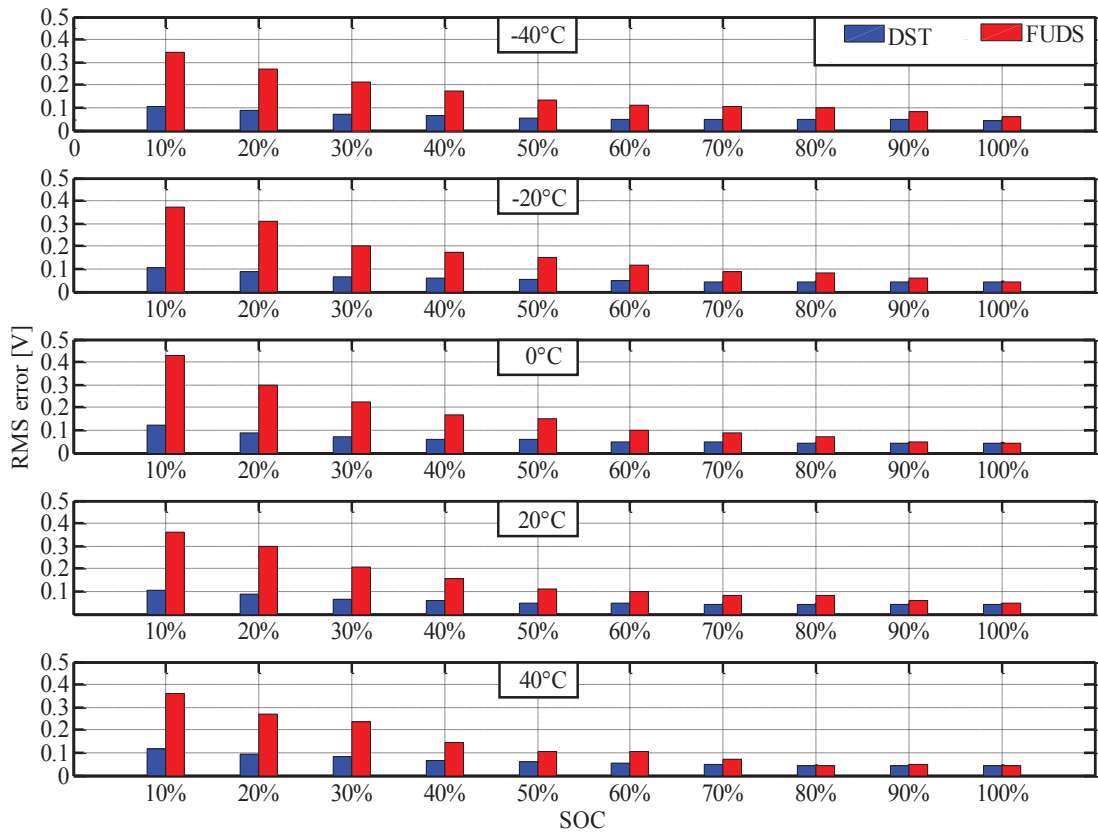


Fig. 2.15 RMS error in DST and FUDS tests with different operating conditions.

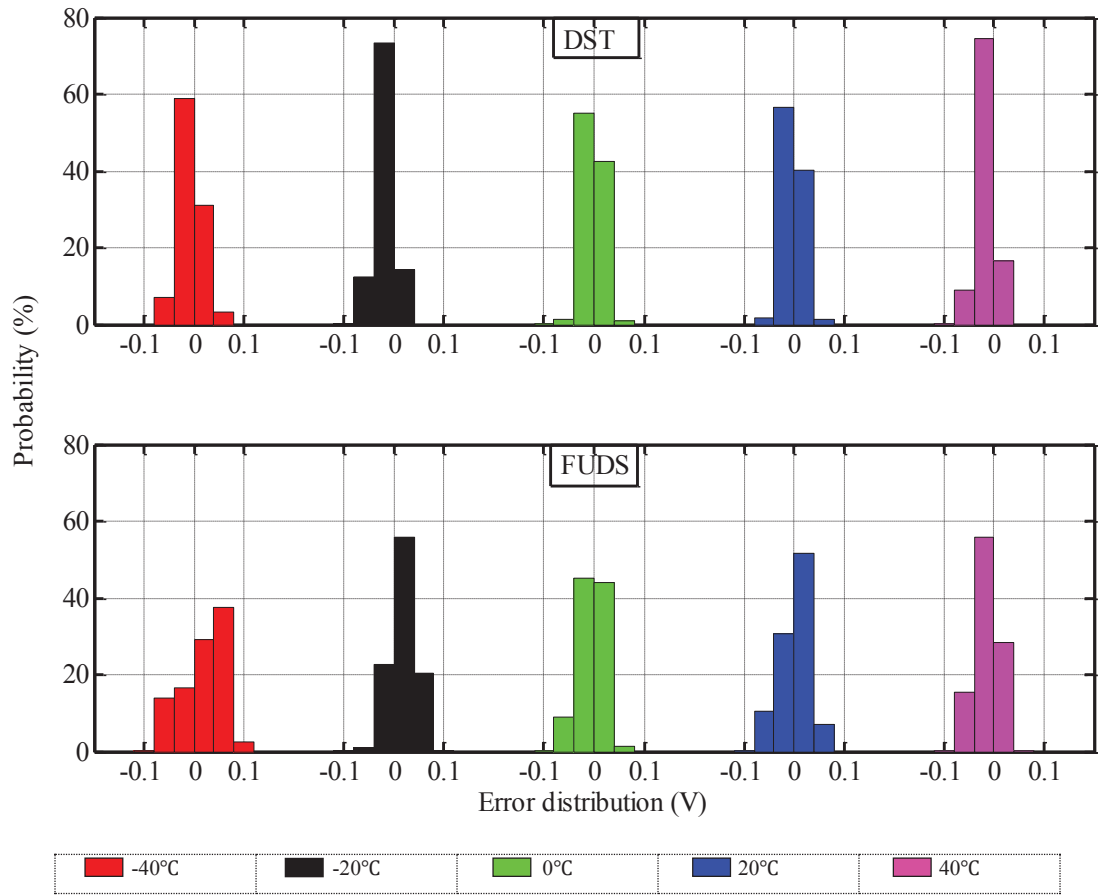


Fig. 2.16 Error distribution under dynamic driving-cycle tests at all temperatures.

2.5 Summary

The establishment of a wide-ranging, accurate and reliable database is critical for the modelling and state estimation of a UC system. This chapter briefly introduced a test rig and its specification which is able to acquire UC test data. A variety of tests were conducted on the test rig including the static capacity test, EIS tests under different temperatures and SOCs, and dynamic tests. A specific test procedure was designed for test implementation, and a UC database was built based on the obtained data, which lays the foundations for the study of the modelling and state estimation described in later chapters. Based on the EIS test data, the UC impedance characteristics at different operating conditions (wide range of temperatures and SOC values) was systematically studied. The experimental results indicate that the impedance magnitude exhibits an exponential increase as the temperature decreases, while the impedance phase at relatively low or high frequencies is sensitive to the temperature variation. These impedance alterations will inevitably compromise the UC system efficiency and power capability in low temperature environments, which needs a careful consideration in system integration and control. The analysis of the SOC dependency of the impedance highlights the high-efficiency SOC window of the tested UC. Such a window varies with temperature, which reflects the interactive effect of the temperature and SOC on the UC impedance. It is valuable to take this into consideration when optimizing the UC system performance. To verify the effectiveness of the EIS-based investigation, the dynamic model was calibrated in order to predict the UC dynamics, whose high accuracy has been substantiated in the DST and FUDS tests. The model parameters have been optimized by executing the nonlinear least-squares algorithm, given large amounts of EIS test data. These high-fidelity parameters enable a

quantitative analysis of how the UC parameters are affected by the temperature and SOC changes.

3 A Comparative Study of Equivalent Circuit Models of Ultracapacitors for Electric Vehicles

3.1 Motivation

A model that can emulate the dynamics of a UC with high precision and good robustness is of utmost importance for energy management design in EVs equipped with UCs or HESSs [53]. The model should also avoid excessive complexity so that it can be easily incorporated into real-time controllers. Therefore, it is vital to strike a balance between model accuracy and robustness, and model complexity. There are many ultracapacitor models existing in the literature [87]. They can be generally categorized into three groups: *electrochemical models*, *ANN-based models* and *equivalent circuit models*. **Electrochemical models** are derived from first principles, and can achieve very high accuracy once their parameters are precisely identified. They depict the real physical-chemical reactions inside the UC from an elemental view, which makes them suitable for understanding and optimizing UC design. However, the modelling uses sets of partial differential equations that have a large number of unknown parameters, some of which are particularly difficult to be calibrated. The extreme complexity of these differential equations leads to unacceptable computation loading and large memory requirement. Hence, PDE-based electrochemical models are not desirable for real-time energy management and power control in electric vehicles.

ANN-based models can accurately capture the dynamics of a UC given an appropriate training data set, due to their powerful capability for approximating any nonlinear function

between the inputs and outputs [88]. The performance and accuracy of these models, nevertheless, relies heavily on the amount and quality of the training data. As a consequence, their robustness may not be great under varying loading conditions.

Equivalent circuit models have been well developed for on-board energy management in EVs and extensively reported in the literature [89][90]. They are lumped-parameter models with relatively simple structures, while maintaining a reasonable precision in terms of the delineation of the dynamic behaviour of a UC. Unfortunately, there are few studies comparing these models in a comprehensive and systematic fashion. In [91], the authors reviewed and compared a variety of equivalent circuit models. Model characterization was performed through constant-current and constant-power tests, and the EIS technique. However, such tests significantly differ from the real loading conditions of a UC pack in an EV application, and are also highly sensitive to measurement noise. Consequently, the robustness and accuracy of the models cannot be sufficiently verified in highly dynamic loading regimes (characteristic to EV applications).

The overarching goal of this chapter is therefore to systematically compare the applicability of different models (i.e., a comprehensive measure of model complexity, accuracy, and robustness) in the context of driving-cycle-based loading conditions. Particularly, robustness means modelling accuracy retention capability when the model is exposed to random loading conditions. This is critical since the model is always parameterized under a certain scenario, and then used in unpredictable and varying conditions. To that end, the state-of-the-art lumped equivalent circuit models are examined; i.e., the classic equivalent circuit model, the multi-stage ladder model, and the dynamic model. The genetic algorithm (GA) is used to identify the optimal parameters of these models using the

experimental data specially collected in the HPPC test. The GA method is capable of extracting the optimal model parameters by searching the whole possible parameter sphere as well as avoiding the local traps, thus effectively offsetting the impacts brought by measurement noises. Finally, the robustness of these models is evaluated and contrasted using the validation data acquired in the DST and an SDP test. The DST and SDP tests serve as representatives of driving-cycle-based loading profiles. The comparison outcomes provide useful insights into model selection, parameterization, and simulation of UCs for the development of EV energy management strategies.

3.2 Model Description

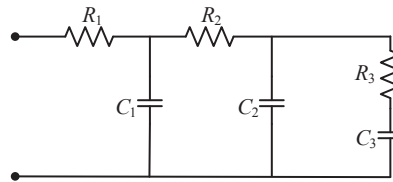
Equivalent circuit models are lumped models that describe the voltage response using a basic electrical circuit composed of common electrical components. They exhibit both moderate accuracy and complexity in comparison with sophisticated electrochemical models and intelligence-based models. Several different equivalent circuit models have been reported in the literature. For a UC, these models can be grouped into three types: the classic model, the multi-stage ladder model, and the dynamic model, with their model structures and state-space representations shown in Fig. 3.1 and Table 3.1, respectively. Note that all the above formulated continuous state-space equations were transformed into their corresponding discrete forms for predicting the voltage evolution using the measured input samples. The model parameters that need to be identified are summarized in Table 3.2.

The ladder model is based on the porous structure of a UC, and can dynamically mimic the distributed nature of the UC. Note that this type of model is flexible in terms of the number of stages. Generally, more stages lead to higher model accuracy at the cost of computational efficiency. For EV applications, it is reasonable to adopt the three-stage ladder model to achieve a trade-off between model accuracy and complexity for the real-time energy management. The dynamic model consists of a bulk capacitance, a series resistance, and two *RC* networks. The *RC* networks aim to represent capacitance and charge distributions across the interface of double layers. The number of *RC* networks is flexible as well. Here, a dynamic model with two *RC* networks is adopted for fair comparison to the three-stage ladder model, as well as for its ample accuracy in representing the UC dynamics in real applications. The

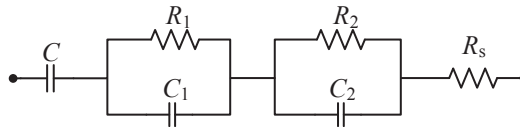
dynamic model is capable of capturing the transient behaviour of a UC over a wide range of frequencies.



(a) Classic model



(b) Ladder model



(c) Dynamic model

Fig. 3.1 Model structure.

Table 3.1 State-space representations.

Model type	State-space representation
Classic model	where V_c denotes the output voltage of the model, R_s is the internal resistance which includes the electrolyte resistance and contact resistance, R_p is used to simulate the self-discharge phenomenon, u_c denotes the voltage across the capacitor and i is the charging current.
	$\begin{cases} \frac{du_c}{dt} = -\frac{1}{CR_p}u_c + \frac{1}{C}i \\ V_c = u_c + iR_s \end{cases}$

Ladder model

$$\begin{bmatrix} \frac{du_1}{dt} \\ \frac{du_2}{dt} \\ \frac{du_3}{dt} \end{bmatrix} = \begin{bmatrix} -\frac{1}{R_2 C_1} & \frac{1}{R_2 C_1} & 0 \\ \frac{1}{R_2 C_2} & -\frac{R_2 + R_3}{R_3 R_2 C_2} & \frac{1}{R_3 C_2} \\ 0 & \frac{1}{R_3 C_3} & -\frac{1}{R_3 C_3} \end{bmatrix} \begin{bmatrix} u_1 \\ u_2 \\ u_3 \end{bmatrix} + \begin{bmatrix} \frac{1}{C_1} \\ 0 \\ 0 \end{bmatrix} i$$

$V = u_1 + R_1 i$

where u_1 , u_2 and u_3 denote the voltages across the capacitors C_1 , C_2 and C_3 , and V is the output voltage.

Dynamic model

where u_0 represents the bulk capacitance, u_1 and u_2 denote the voltages of the two RC networks, V is the output voltage, and R_s represents the series resistance.

$$\begin{bmatrix} \frac{du_1}{dt} \\ \frac{du_2}{dt} \\ \frac{du_3}{dt} \end{bmatrix} = \begin{bmatrix} 0 & 0 & 0 \\ 0 & -\frac{1}{R_1 C_1} & 0 \\ 0 & 0 & -\frac{1}{R_2 C_2} \end{bmatrix} \begin{bmatrix} u_1 \\ u_2 \\ u_3 \end{bmatrix} + \begin{bmatrix} \frac{1}{C} \\ \frac{1}{C_1} \\ \frac{1}{C_2} \end{bmatrix} i$$

$V = u_0 + u_1 + u_2 + R_s i$

Table 3.2 Model parameters for identification.

Model type	Model parameters
Classic model	C, R_s, R_p
Ladder model	$C_1, C_2, C_3, R_1, R_2, R_3$
Dynamic model	$C, R_s, C_1, C_2, R_1, R_2$

3.3 Model Characterization

The parameters of these models are identified by means of the HPPC test dataset. In order to avoid getting locked in local optima, the GA was adopted to search for the optimal solution. This is one approach to global optimization. Compared with traditional optimization methods, the GA proves to be robust in solving the non-gradient and global optimization problems, which is well-suited for the random searching of optimal model parameters. There are only a few parameters to assign for the GA, as listed in Table 3.3.

The optimization objective is to minimize the RMS error between the experimentally recorded voltage and the simulated output of the optimized models. The RMS error is a good indicator of the model accuracy and robustness. The optimization process starts with a random population initialization, where the model parameters are coded by a sequence of binary numbers in each population member. The RMS error is then used as the fitness function to evaluate each population member. A roulette game is applied to update the population members in a sense that the fittest population member is conserved for further operations in the game. Parents are then picked at random from the population to generate a new population through crossover and mutation operators. Usually, mutations occur randomly along the long strings of genes at fairly low odds. The RMS error is once again employed to evaluate the fitness of the new population members. This process is iteratively implemented until the termination criteria are fulfilled. The pseudo code of the implemented GA for UC characterization is shown in Table 3.4. Further details of the GA are in [92]. The derived parameters are given in Table 3.5.

Table 3.3 The key parameters of the genetic algorithm.

Parameter (Abbreviation)	Value
Population Size (N)	30
Number of Generation ($iGen$)	100
Tournament Selection (p_s)	0.75
Crossover Probability (p_c)	0.8
Mutation Probability (p_m)	0.025

Table 3.4 The pseudo code of GA for UC model characterization.

Step 1: The bounds of the model parameters, θ_L and θ_U , are assigned.

Step 2: Randomly generate the initial population P_0 which comprises N members, i.e., m_1^j, \dots, m_N^j , within the parameter bounds. Each member represents a possible solution of the model parameters. Herein, the uppercase j is the generation index.

Step 3: Evaluate the function $f(P_0)$, and register the population member with the best performance as $bestInd$ with its function value $Find$. The $Find$ is also assigned to the $bestGlobal$, which retains the function value of the fittest member so far. The function $f(\cdot)$ is the cost function that gauges the root-squared-error between the simulated voltage and the measured voltage based on the input model parameters.

Step 4: If j is less than the $iGen$, the following steps are repeated:

- (1) The roulette game is used to rearrange the population with the sense that the members with better performance have bigger chance to survive for further operation.
- (2) The parents are selected randomly to manoeuvre the crossover and mutation with the possibilities of p_c and p_m , respectively. As a result, a renewed population P_j is obtained for further fitness evaluation.
- (3) Calculate the function $f(P_j)$ for the updated population, and recode the best performer $bestInd$.
- (4) Compare the function value of $bestInd$ with the preceding $bestGlobal$, and assign the new $Find$ to the $bestGlobal$ if it is smaller. $j=j+1$.

Step 5: If $j=iGen$, terminate the algorithm. Recall the member with the best performance index $bestGlobal$.

Table 3.5 The derived optimal model parameters.

Ultracapacitor models	Parameter (Unit)	Value
Classic model	C (F)	2708
	R_p (Ω)	4366
	R_s (Ω)	9.854×10^{-4}
Multi-stage ladder model	C_1 (F)	1680
	C_2 (F)	749
	C_3 (F)	193
	R_1 (Ω)	4.5×10^{-4}
	R_2 (Ω)	5.0×10^{-5}
	R_3 (Ω)	4.0×10^{-5}
Dynamic model	C (F)	2712
	R_s (Ω)	8.216×10^{-4}
	C_1 (F)	627
	C_2 (F)	1843
	R_2 (Ω)	3.883×10^{-4}

3.4. Comparison Result and Discussion

3.4.1 Model accuracy and robustness

To evaluate and compare the precision of the three models in the HPPC, DST and SDP tests, several statistical metrics, i.e., maximum error and mean error, and RMS error, are taken into account. Comparative results of these models in the HPPC test are given in Fig. 3.2. It can be seen that the classic model exhibits slightly better accuracy than the dynamic model, while the ladder model is worst.

For EV applications, model robustness under transient and varying conditions is very important. Here, the datasets in the DST and SDP tests are used to examine the robustness of these models. The results of the DST test are shown in Fig. 3.3. It shows the accuracy of the ladder model in the DST test is even lower than that in the HPPC test. Its robustness may be a challenging issue for realistic EV control system design. However, the precision of the classic model and the dynamic model are similar to those in the HPPC test. Furthermore, it is discernible that the dynamic model is more precise than the classic model in the DST test, despite a slightly poorer performance in the HPPC test. This in turn demonstrates that the dynamic model is more robust.

To further verify robustness of these models under varying loading profiles, the data recorded in the SDP test are also considered. The SDP profile serves to emulate the highly unpredictable loading scenarios of EV UCs. The evaluation results in the SDP test are given in Fig. 3.4. They also illustrate that the dynamic model has the best overall performance.

In summary, the dynamic and classic models can better capture the dynamics of the tested UC in all the tests in comparison to the ladder model. Even though the classic model has a

simpler structure and slightly better accuracy in the HPPC test, the dynamic model exhibits better robustness against variant loading conditions.

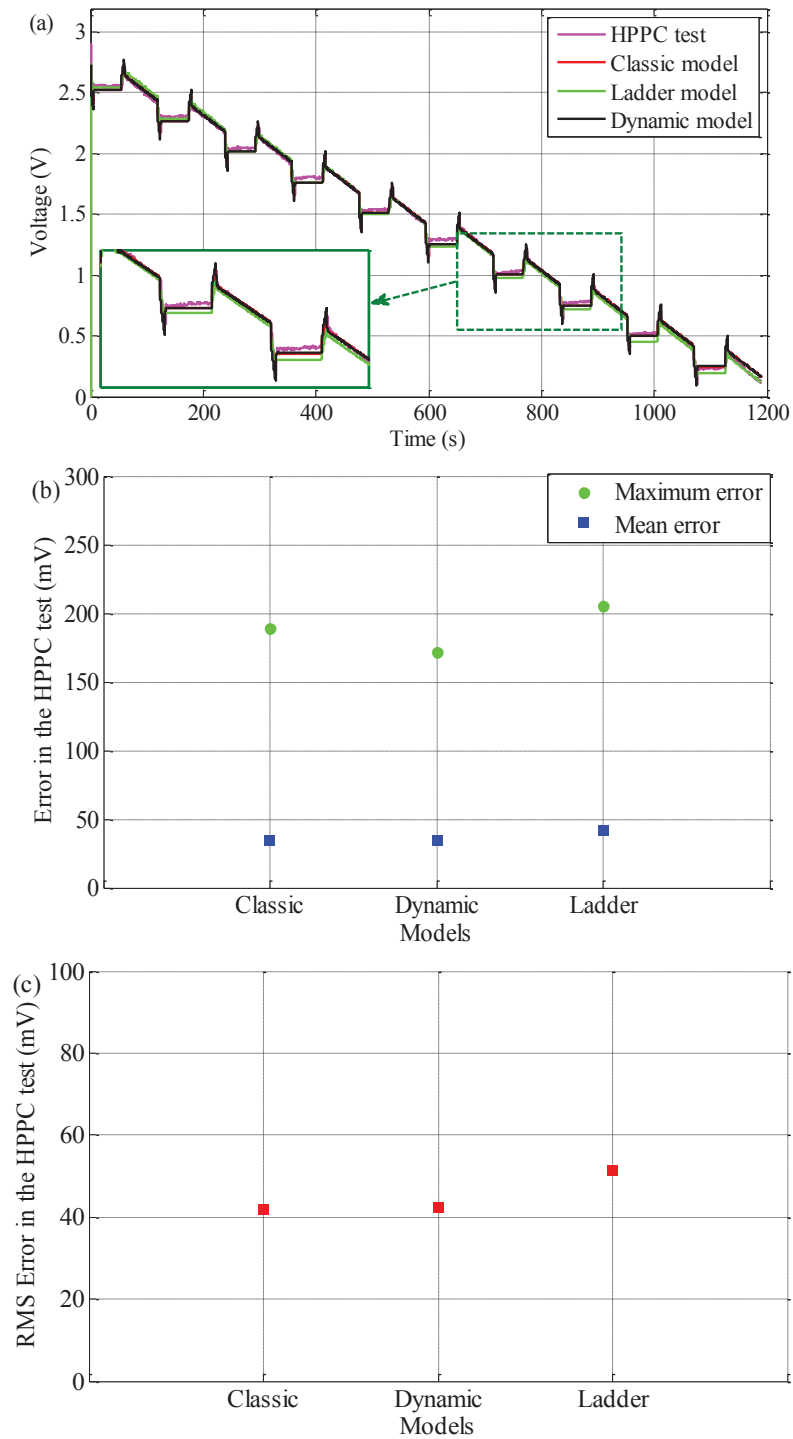


Fig. 3.2 Comparison outcomes in the HPPC test: (a) Simulated and measured voltages; (b) Maximum and mean absolute errors; (c) RMS error.

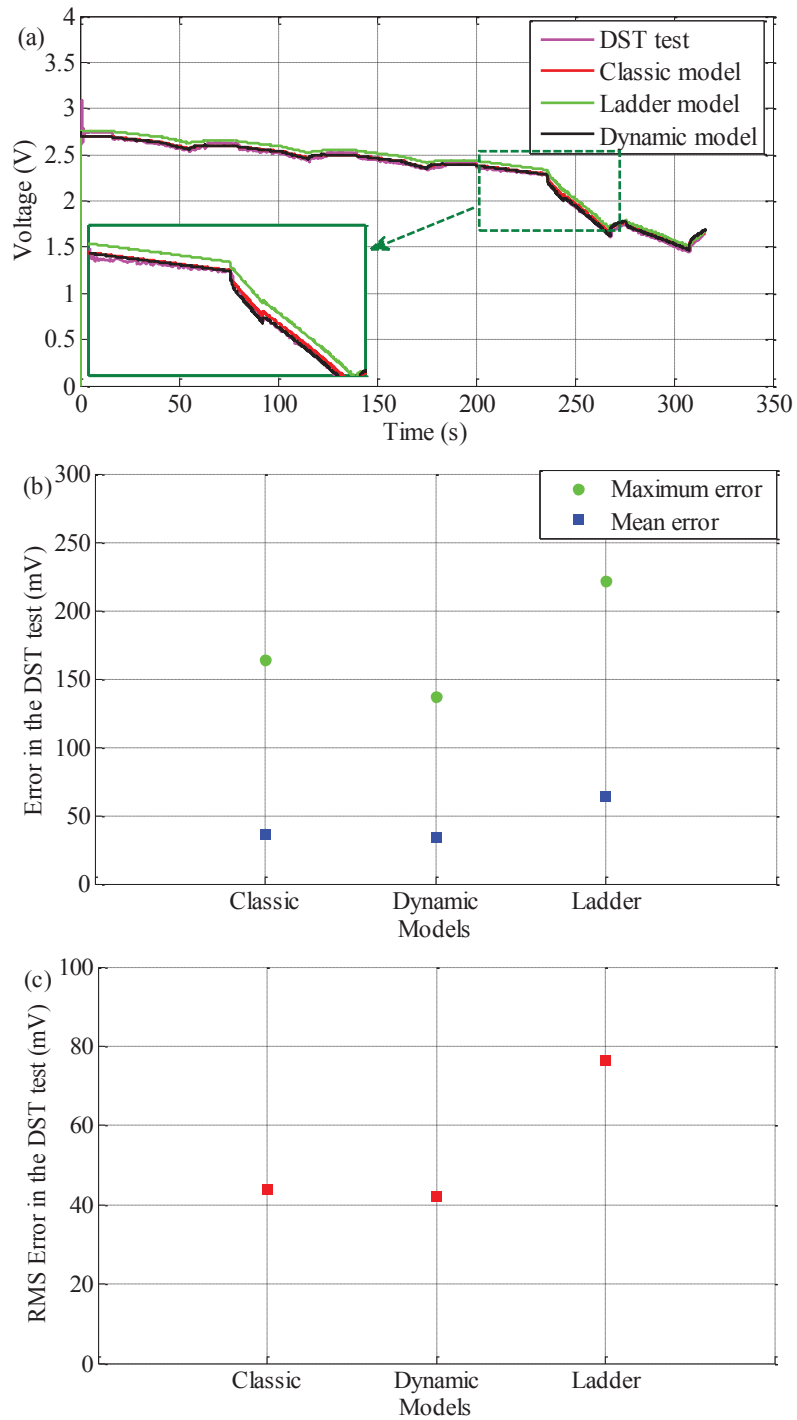


Fig. 3.3 Comparison outcomes in the DST test: (a) Simulated and measured voltages; (b) Maximum and mean absolute errors; (c) RMS error.

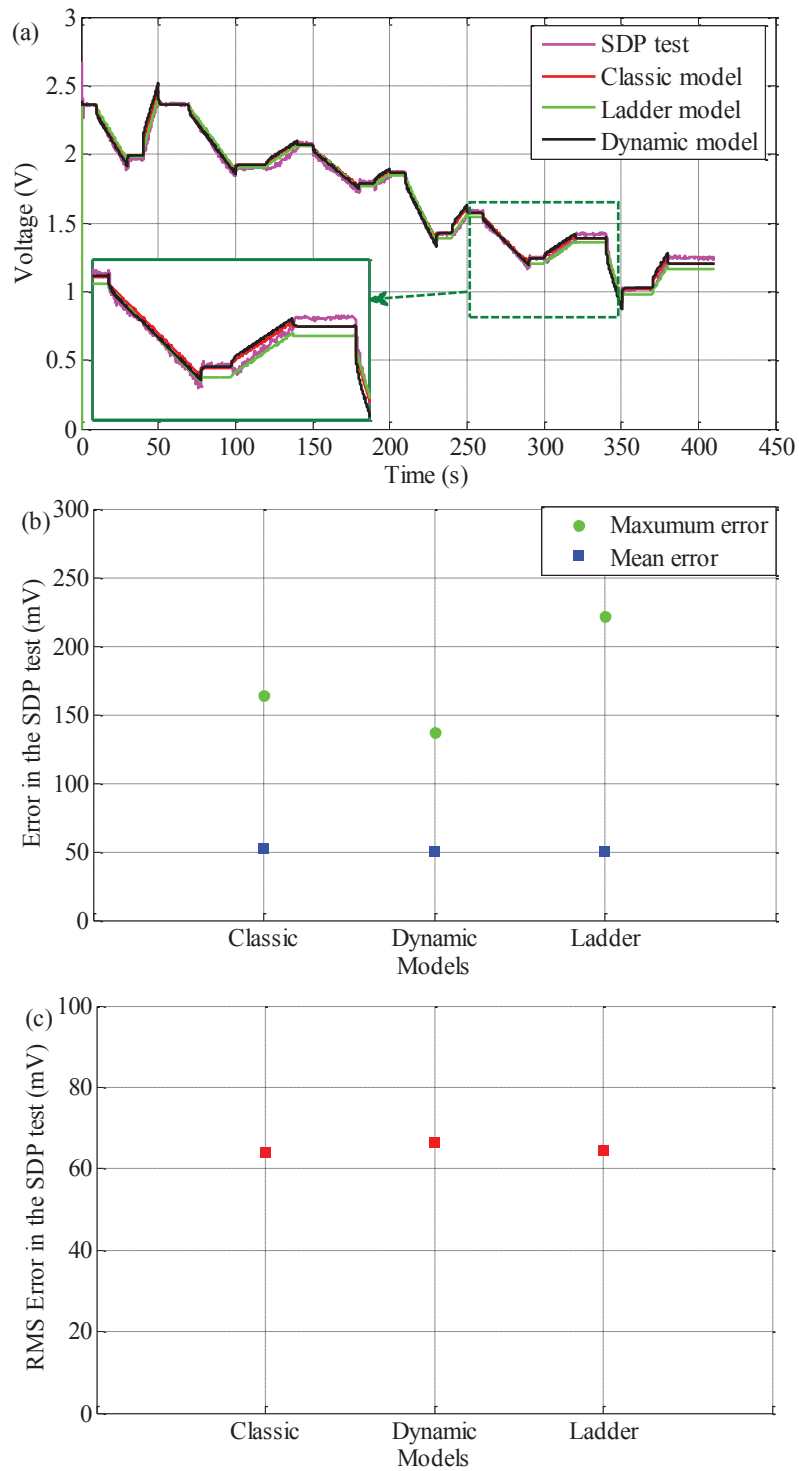


Fig. 3.4 Comparison outcomes in the SDP test: (a) Simulated and measured voltages; (b) Maximum and mean absolute errors; (c) RMS error.

3.4.2 Model complexity

In terms of model complexity, the classic model has the simplest structure. Only one ODE is sufficient to describe the state evolution during operation of the tested UC. However, it often fails to capture the highly dynamic voltage response of the tested UC. Meanwhile, the ladder model and the dynamic model appear to have similar complexity, and the same order of ODEs, in order to represent the dynamics of the tested UC. The derivation of the discrete system matrix for the ladder model proves to be extremely complex and time-consuming. In contrast, the dynamic model has a system matrix in the diagonal form so that the discretization process is fairly straightforward in accordance with the basic control theory, while it has the capability of capturing the dynamics using its inherent *RC* networks. Therefore, it is obvious that the dynamic model is preferred to the other models even when taking the model complexity into account.

3.5. Summary

A comparative study of the equivalent circuit models of UCs has been conducted in the context of EV applications. These models are selected from the state-of-the-art lumped equivalent circuit models reported in the literature; i.e., the classic model, the multi-stage ladder model, and the dynamic model. The GA is used to identify the optimal model parameters. The model accuracy, complexity, and robustness are then evaluated and compared by means of different datasets. Assessment results illustrate that the most complicated ladder model has the lowest accuracy and robustness; the classic model has the second best overall performance; and the dynamic model is the best compromise between model precision/robustness and complexity. It is reasonable to conclude that the dynamic model of a UC is the preferable option for EV energy management design.

4 An Online Parameter Identification of Ultracapacitor Models Using the Extended Kalman Filter

4.1 Motivation

Equivalent circuit models have been carefully developed, especially for the energy management design and power control. The key advantage of these equivalent models lies in their relatively small number of parameters. The accuracy of the parameterization is significant in terms of the electric vehicle context. A large body of literature exists pertaining to parameter extraction methods. For example, Spyker and Nelms [33] presented a classical equivalent circuit that comprises an equivalent series resistance, an equivalent parallel resistance, and a main capacitor. The model parameters were derived by measuring the voltage responses during charge and rest. However, the accuracy of this method is highly dependent on the measurement precision so it is sensitive to measurement noises. Gualous *et al.* [43] used the EIS method to characterize a second-order equivalent circuit model for UCs. EIS is a commonly used approach for the measurement of the complex impedance of energy storage devices such as batteries and UCs. This is done for a wide range of frequencies by imposing a known bias voltage upon the terminals of the tested storage device and detecting the corresponding excitation current [93]. The obtained frequency spectra can be modelled with interleaved *RC* circuits by analyzing the frequency dependency of the real and imaginary parts of impedance, thus resulting in an equivalent circuit model [94]. However, the precision of an identified model when obtained using the EIS method may be compromised under the

varying loading conditions due to offline implementation. This can be attributed to the fact that the lumped equivalent circuit model parameters are largely dependent on the loading conditions, which makes the offline EIS-obtained model incapable of representing the dynamics of batteries or UCs accurately in the real implementation. The majority of the methods presented in the literature are subject to the similar drawbacks; i.e., susceptibility to measurement precision and noise and offline implementation. In order to tackle these problems, this work employs the EKF to recursively estimate the model parameters. The EKF has the advantages of being closed-loop, online, and the availability of error bounds. Hence it has been widely used to perform the model calibration for batteries in real time. However, there is a lack of literature reporting the application of the EKF technique to identify online UC model parameters.

4.2 Modelling and Parameter Estimation for UCs

4.2.1 UC model structure

There are a variety of equivalent circuit model structures for UCs. Here, the dynamic model is selected since its superiority has been confirmed in Chapter 3. The detailed structure is shown in Fig. 4.1, where u_0 denotes the voltage across the bulk capacitor C , u_1 and u_2 denote the voltages of the two RC circuits, respectively, u denotes the output voltage, and R_s denotes the series resistance.

According to basic electrical circuit principles, the continuous state equation can be derived as:

$$\begin{bmatrix} \dot{u}_0 \\ \dot{u}_1 \\ \dot{u}_2 \end{bmatrix} = \begin{bmatrix} 0 & 0 & 0 \\ 0 & -\frac{1}{R_1 C_1} & 0 \\ 0 & 0 & -\frac{1}{R_2 C_2} \end{bmatrix} \begin{bmatrix} u_0 \\ u_1 \\ u_2 \end{bmatrix} + \begin{bmatrix} \frac{1}{C} \\ \frac{1}{C_1} \\ \frac{1}{C_2} \end{bmatrix} i \quad (4.1)$$

Based on the Euler method, the state equation can be further transformed into the discrete-time state equation so that:

$$\begin{bmatrix} u_{0,k+1} \\ u_{1,k+1} \\ u_{2,k+1} \end{bmatrix} = \begin{bmatrix} 1 & 0 & 0 \\ 0 & a_1 & 0 \\ 0 & 0 & a_2 \end{bmatrix} \begin{bmatrix} u_{0,k} \\ u_{1,k} \\ u_{2,k} \end{bmatrix} + \begin{bmatrix} \frac{\Delta T}{C} \\ b_1 \\ b_2 \end{bmatrix} i_k \quad (4.2)$$

where:

$$a_1 = e^{\frac{-\Delta T}{R_1 C_1}} \quad (4.3)$$

$$a_2 = e^{\frac{-\Delta T}{R_2 C_2}} \quad (4.4)$$

$$b_1 = R_1 - R_1 e^{\frac{-\Delta T}{R_1 C_1}} \quad (4.5)$$

$$b_2 = R_2 - R_2 e^{\frac{-\Delta T}{R_2 C_2}} \quad (4.6)$$

with the sampling time ΔT . The output equation can be derived:

$$u_k = u_{0,k} + u_{1,k} + u_{2,k} + i_k R_s \quad (4.7)$$

where k denotes the time interval index.

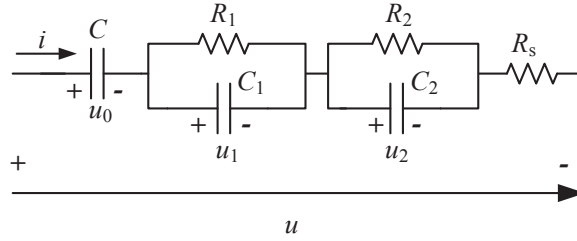


Fig. 4.1 The UC model structure.

4.2.2 Parameter estimation using the extended Kalman filter

Recently, the Kalman filter has gained more popularity in the field of state estimation, parameter estimation and dual estimation due to its inherent merits [95]. That is, it can be implemented online and automatically provides the estimation error bound. In order to implement an extended Kalman filter to recursively estimate the parameters, the process of parameter evolution can be formulated into a state equation so that:

$$\theta_{k+1} = \theta_k + \omega_k \quad (4.8)$$

$$u_k = g(\mathbf{x}_k, \mathbf{i}_k, \theta_k) + v_k \quad (4.9)$$

\mathbf{x}_k is the state vector, and:

$$\mathbf{x}_k = [u_{0,k}, u_{1,k}, u_{2,k}]^T \quad (4.10)$$

$$g(\mathbf{x}_k, \mathbf{i}_k, \boldsymbol{\theta}_k) = u_{0,k} + u_{1,k} + u_{2,k} + i_k R_s \quad (4.11)$$

$$\boldsymbol{\theta} = [a_1, b_1, a_2, b_2, C_{recip}, R_s]^T \quad (4.12)$$

where $\boldsymbol{\theta}$ denotes the parameter vector, C_{recip} denotes the reciprocal of C , u_k is the output voltage at time interval k , i_k is the charging current (a negative value denotes discharging), $\boldsymbol{\omega}_k$ represents the process noise, which is assumed to be Gaussian white noise with zero mean and covariance of \mathbf{Q} , and \boldsymbol{v}_k represents the measured noise which is also assumed to be Gaussian white noise with zero mean and a covariance of \mathbf{W} . Based on process and output equations described above, the EKF equations can be derived in the state-equation form. At each time interval, the time update and measurement update are consecutively performed. In this work, two constant values are assigned to process and measurement noise covariances:

1. Time update:

$$\hat{\boldsymbol{\theta}}_{k|k-1} = \hat{\boldsymbol{\theta}}_{k-1} \quad (4.13)$$

$$\mathbf{P}_{k|k-1} = \mathbf{P}_{k-1} + \mathbf{Q} \quad (4.14)$$

where $\hat{\boldsymbol{\theta}}_{k|k-1}$ is the priori estimate of the parameter vector $\boldsymbol{\theta}$ at time interval k before the measurement u_k is taken into consideration, $\hat{\boldsymbol{\theta}}_{k-1}$ is the a posteriori estimate of the parameter vector at time interval $k-1$, $\mathbf{P}_{k|k-1}$ represents the a priori estimation error covariance of parameter vector $\boldsymbol{\theta}$ at time interval k , and \mathbf{P}_{k-1} represents the a posteriori estimation error covariance of parameter vector $\boldsymbol{\theta}$ at time interval $k-1$.

2. Measurement update:

$$\mathbf{L}_k = \mathbf{P}_{k|k-1} \mathbf{C}_k^T (\mathbf{C}_k \mathbf{P}_{k|k-1} \mathbf{C}_k^T + \mathbf{W})^{-1} \quad (4.15)$$

$$\hat{\boldsymbol{\theta}}_k = \hat{\boldsymbol{\theta}}_{k|k-1} + \mathbf{L}_k (u_k - \mathbf{g}(\hat{\mathbf{x}}_k, \mathbf{i}_k, \hat{\boldsymbol{\theta}}_{k|k-1})) \quad (4.16)$$

$$\mathbf{P}_k = (\mathbf{I} - \mathbf{L}_k \mathbf{C}_k) \mathbf{P}_{k|k-1} \quad (4.17)$$

$$\mathbf{C}_k = \left. \frac{d\mathbf{g}(\hat{\mathbf{x}}_k, \mathbf{i}_k, \hat{\boldsymbol{\theta}}_{k|k-1})}{d\boldsymbol{\theta}} \right|_{\boldsymbol{\theta}=\hat{\boldsymbol{\theta}}_{k|k-1}} \quad (4.18)$$

where \mathbf{I} denotes the identity matrix with proper dimension, \mathbf{W} represents the covariance of the measurement noise ϑ and \mathbf{L}_k is the Kalman gain at time interval k . $\hat{\mathbf{x}}_k$ can be computed given $\hat{\mathbf{x}}_{k-1}$ and $\hat{\boldsymbol{\theta}}_{k-1}$ according to (4.2). Updates in the time and measurement equations at each time interval means that the parameter vector $\hat{\mathbf{x}}_k$ can be recursively estimated. Since $\hat{\mathbf{x}}_k$ acts as a function of the parameter vector $\hat{\boldsymbol{\theta}}_k$, \mathbf{C}_k can be computed by performing recurrent differentiations, which are:

$$\frac{d\mathbf{g}(\hat{\mathbf{x}}_k, \mathbf{i}_k, \boldsymbol{\theta}_k)}{d\boldsymbol{\theta}} = \frac{\partial \mathbf{g}(\hat{\mathbf{x}}_k, \mathbf{i}_k, \boldsymbol{\theta}_k)}{\partial \boldsymbol{\theta}} + \frac{\partial \mathbf{g}(\hat{\mathbf{x}}_k, \mathbf{i}_k, \boldsymbol{\theta}_k)}{\partial \hat{\mathbf{x}}_k} \frac{d\hat{\mathbf{x}}_k}{d\boldsymbol{\theta}} \quad (4.19)$$

$$\frac{d\hat{\mathbf{x}}_k}{d\boldsymbol{\theta}} = \frac{\partial f(\hat{\mathbf{x}}_{k-1}, \mathbf{i}_{k-1}, \boldsymbol{\theta})}{\partial \boldsymbol{\theta}} + \frac{\partial f(\hat{\mathbf{x}}_{k-1}, \mathbf{i}_{k-1}, \boldsymbol{\theta})}{\partial \hat{\mathbf{x}}_{k-1}} \frac{d\hat{\mathbf{x}}_{k-1}}{d\boldsymbol{\theta}} \quad (4.20)$$

where:

$$\frac{\partial \mathbf{g}(\hat{\mathbf{x}}_k, \mathbf{i}_k, \boldsymbol{\theta}_k)}{\partial \boldsymbol{\theta}} = [0 \quad 0 \quad 0 \quad 0 \quad 0 \quad \mathbf{i}_k] \quad (4.21)$$

$$\frac{\partial g(\hat{\mathbf{x}}_k, \mathbf{i}_k, \boldsymbol{\theta}_k)}{\partial \hat{\mathbf{x}}_k} = [1 \quad 1 \quad 1] \quad (4.22)$$

$$\frac{\partial f(\hat{\mathbf{x}}_{k-1}, \mathbf{i}_{k-1}, \boldsymbol{\theta})}{\partial \boldsymbol{\theta}} = \begin{bmatrix} 0 & 0 & 0 & 0 & \Delta T \mathbf{i}_{k-1} & 0 \\ u_{1,k-1} & \mathbf{i}_{k-1} & 0 & 0 & 0 & 0 \\ 0 & 0 & u_{2,k-1} & \mathbf{i}_{k-1} & 0 & 0 \end{bmatrix} \quad (4.23)$$

$$\frac{\partial f(\hat{\mathbf{x}}_{k-1}, \mathbf{i}_{k-1}, \boldsymbol{\theta})}{\partial \hat{\mathbf{x}}_{k-1}} = \begin{bmatrix} 1 & 0 & 0 \\ 0 & \hat{\mathbf{a}}_{1,k-1} & 0 \\ 0 & 0 & \hat{\mathbf{a}}_{2,k-1} \end{bmatrix} \quad (4.24)$$

f represents the system function given in (4.2).

It is obvious that the derivative calculation is recursive, and can be initiated by:

$$\frac{d \hat{\mathbf{x}}_0}{d \boldsymbol{\theta}} = 0 \quad (4.25)$$

4.3 Results and Discussion

4.3.1 Parameter estimation in the DST test

In order to validate the proposed estimation algorithm, a transient power test based on the standard DST was conducted on the established test rig. The DST-based test can represent the dynamic load conditions of a UC during daily driving of an electric vehicle with UCs as the single or complementary energy storage. The voltage and current of the UC in the DST test are shown in the Fig. 4.2.

Kalman filters require a priori knowledge about process and measurement noise statistics. When it comes to the algorithm, the process and measurement noise covariance, namely \mathbf{Q} and \mathbf{W} , should be carefully selected. Based on the knowledge of the tested UC, the parameters for the EKF algorithm are specified through trial-and-error method:

$$\hat{\mathbf{x}}_0 = [2.70 \quad 0.02 \quad 0.01]^T \quad (4.26)$$

$$\hat{\boldsymbol{\theta}}_0 = [0.9676 \quad 7.2869 \times 10^{-6} \quad 0.8767 \quad 6.9407 \times 10^{-6} \quad 2700 \quad 0.0006]^T \quad (4.27)$$

$$\mathbf{P}_0 = \text{diag}\{[1 \times 10^{-8} \quad 1 \times 10^{-10} \quad 1 \times 10^{-10} \quad 1 \times 10^{-8} \quad 1 \times 10^{-10} \quad 1 \times 10^{-14}]^T\} \quad (4.28)$$

$$\mathbf{Q} = \text{diag}\{[1 \times 10^{-14} \quad 1 \times 10^{-16} \quad 1 \times 10^{-16} \quad 1 \times 10^{-14} \quad 1 \times 10^{-20} \quad 1 \times 10^{-22}]^T\} \quad (4.29)$$

$$\mathbf{W} = 0.01 \quad (4.30)$$

where $\text{diag}\{[...]\}$ denotes a diagonal matrix with [...] on its main diagonal.

Given the specified parameters, the proposed EKF was implemented in order to online estimate the model parameters of the UC. The evolution of the estimated model parameters is shown in Fig. 4.3. It shows all the estimated parameters tend to converge at the end of the test. It can be seen that the value of R_1 is bigger than that of R_2 while C_1 is just slightly smaller than C_2 . It means that the first RC circuit has a larger time constant than the second RC

network in the selected model. It can be observed that the value C of the main capacitor exhibits a gentle decline, which indicates the capacitance varies with the terminal voltage. It can also be seen that the estimated resistance R_s increases along with the decline of the voltage in the test. The variations of C and R_s reveal that the internal characteristics are also dependent on the external loading conditions [52].

The evolution of the measured and estimated voltages is shown in Fig. 4.4. It can be seen that the estimated voltage shows good agreement with the measured voltage in the DST test. This proves that the recursively identified model can capture the voltage response after compensating for the initial model error. The relative voltage error is illustrated in Fig. 4.5 which further demonstrates the model performance. The converged estimation result is shown in Table 4.1. According to (4.3) to (4.6), the model parameters can be computed and these are shown in Table 4.2.

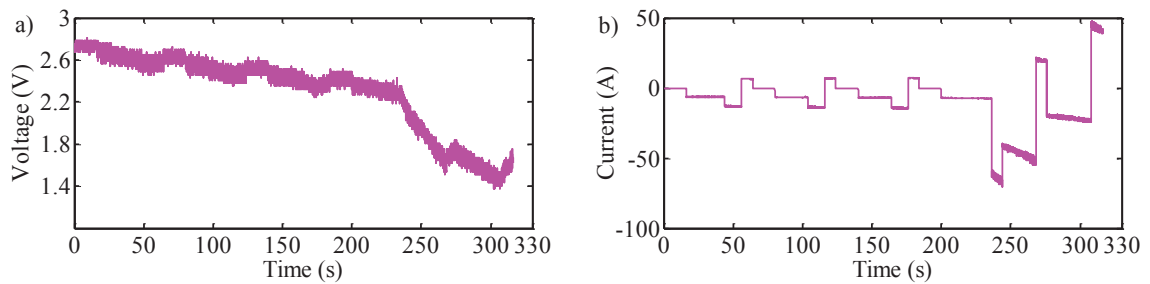


Fig. 4.2 The measured voltage (a) and current (b) profiles in the DST test.

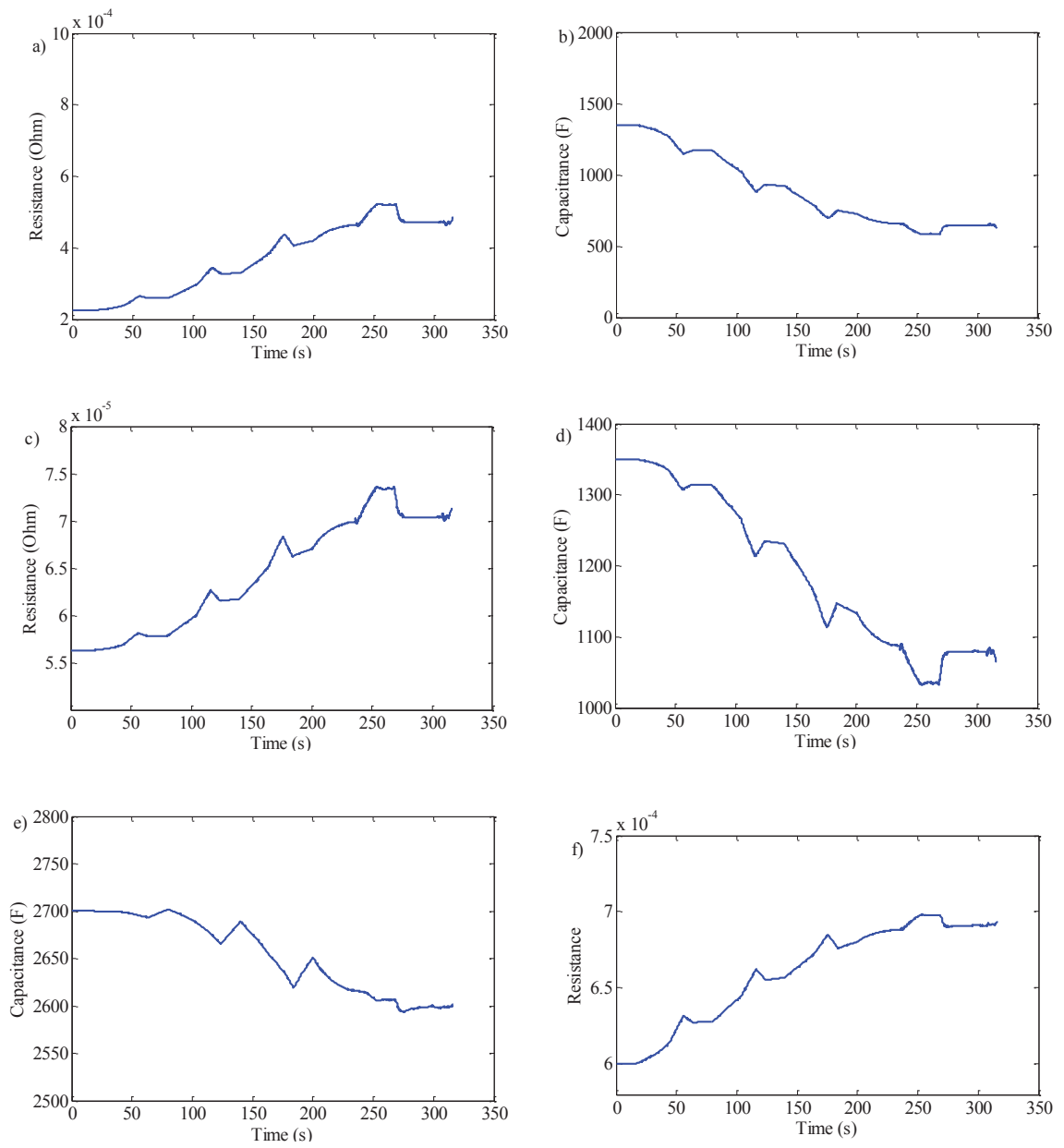


Fig. 4.3 The evolution of the estimated model parameters in the DST test: (a) R_1 ; (b) C_1 ; (c) R_2 ; (d) C_2 ; (e) C ; (f) R_s .

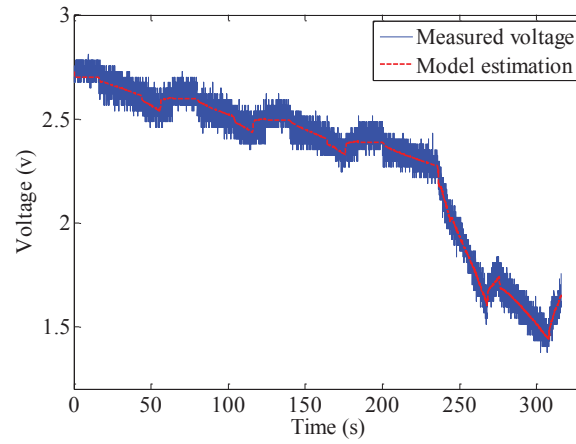


Fig. 4.4 The measured and estimated voltages in the DST test.

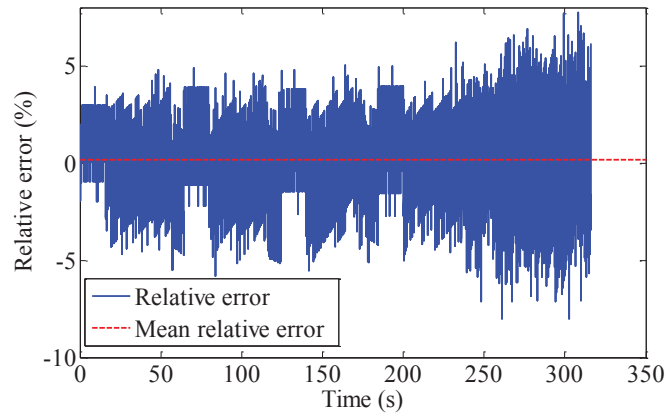


Fig. 4.5 The relative voltage error in the DST test.

Table 4.1 The estimation results of the EKF.

a_1	b_1	a_2	b_2	C_recip	R_s
0.9677	1.55×10^{-5}	0.8767	8.77×10^{-6}	3.85×10^{-4}	6.93×10^{-4}

Table 4.2 The estimated model parameters.

C (F)	C_1 (F)	C_2 (F)	R_1 (Ω)	R_2 (Ω)	R_s (Ω)
2601	628	1065	4.85×10^{-4}	7.14×10^{-5}	6.93×10^{-4}

4.3.2 Model validation in the HPPC test

In order to validate the derived model, the HPPC data was used. The voltage and current profiles in the HPPC test are shown in Fig. 4.6. The simulated and measured voltages are illustrated in Fig. 4.7. It can be seen that the model with the previously estimated parameters can represent well the voltage behaviour under the HPPC test. The error, instead of the relative error between the simulated and measured voltages, is used to indicate the accuracy of the identified model because the voltage of the UC generally decreases to 0 V at the end of the test. The error curve is shown in Fig. 4.8. The mean error is 0.058 V, indicating an average error of 2.2% relative to the rated voltage of the test UC. This accuracy is comparable to that of most advanced models reported in the literature [41]. It verifies that proposed estimation algorithm can achieve robust parameter estimation and be used to derive a model that can predict the dynamics of a UC under different load profiles. Owing to the fact that the DST and HPPC loading profiles are highly dynamic and thus representative of the real driving conditions of vehicles, it is reasonable to conclude that the derived model is applicable to the real driving scenarios with sufficient accuracy. The proposed method can identify the model with precision and robustness.

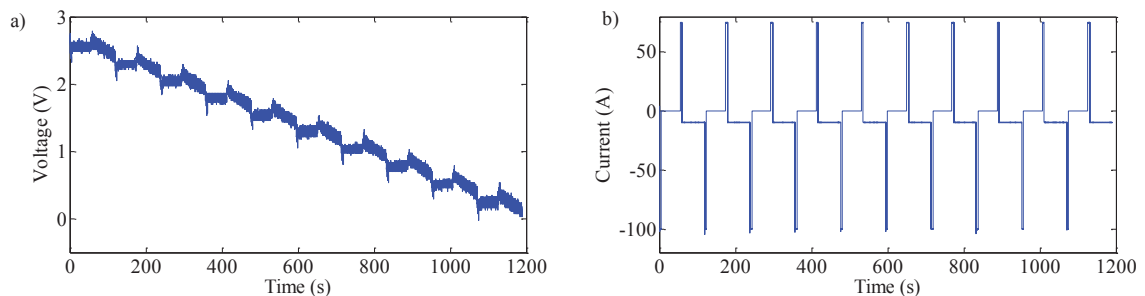


Fig. 4.6 The measured voltage (a) and current (b) profiles in the HPPC test.

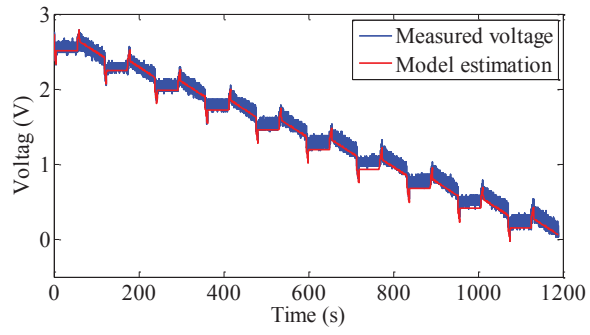


Fig. 4.7 The simulated and measured voltages in the HPPC test.

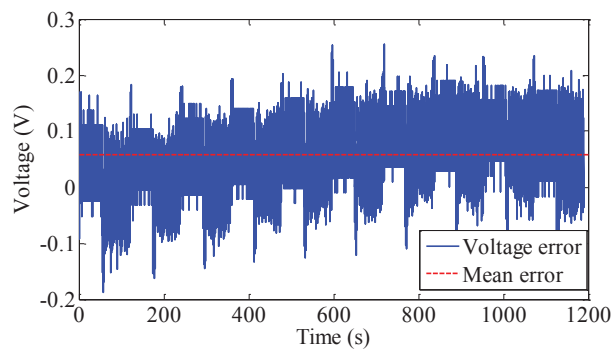


Fig. 4.8 The error between the simulated and measured voltages in the HPPC test.

4.4 Summary

This chapter presents an online model identification method for a UC model based on the well-known Kalman filter. The dynamic model was used to represent the dynamics of a UC. It was composed of a bulk capacitor, a series internal resistance and a second-order RC network. The rationale for the use of this model is that it can sufficiently capture the transient voltage response without introducing heavy computation burden. The evolution of the model dynamics was depicted by a set of discrete state equations according to electrical principles. The equation parameters were extracted and used as the targets for the proposed estimation method. The EKF was formulated and applied to recursively identify the parameters based on the DST test data. The results show that the recursively calibrated model can well represent the transient voltage behaviour under the dynamic operating conditions. In order to further validate the accuracy of the model, the HPPC test data was used. The result shows that the model can also depict the voltage behaviour under the HPPC operating scenarios with high fidelity. This verifies that the proposed method can identify a model in a robust manner against different load profiles.

5 Robust State-of-Charge Estimation of Ultracapacitors for Electric Vehicles

5.1 Motivation

In order to ensure safe and efficient operation of UCs in volatile and demanding conditions, an accurate SOC estimation is important. For example, energy management controllers in advanced energy systems base their control actions on precise SOC estimates, which turns out to make better use of the power potential of UCs without incurring detrimental over-charge/over-discharge.

This chapter presents a robust H -infinity observer for estimating the SOC of a UC. Its primary objective is to guarantee that the H -infinity norm of the estimation error over process and measurement noises is bounded by a given attenuation level in the worst case. In comparison with the state-of-the-art Kalman filter-based (KF-based) approach, there is no requirement for repeatedly adjusting statistical properties of process and measurement noises. Furthermore, the presented observer has the advantage of being robust to modelling uncertainty, thus enabling the feasibility of all-through-life operation against likely aging implications. Also, it is worth mentioning that the H -infinity observer gain can be derived offline, and then used as a fixed multiplier in the real-time estimation, which significantly reduces the computational intensity of real-time implementation. This is in contrast to the continuous and complicated matrix operations of Kalman filters. The Linear Matrix Inequality (LMI) approach is utilized to solve the H -infinity estimation problem, considering its computation efficiency and flexibility. By exploring the solution feasibility of the formulated LMI problem at a given attenuation level, the gain matrix of the H -infinity

observer can be derived. A large amount of experimental data is used to validate the robust estimation scheme, together with a comparison with KF-based methods.

5.2 UC Modelling and Characterization

5.2.1 Model validation in the HPPC test

The dynamic model has been demonstrated to be preferable in terms of model complexity, accuracy, and robustness in the prior work in Chapter 3, and is thus considered in this chapter. As shown in Fig. 5.1, the dynamic model is composed of a series resistance, a bulk capacitance, and two resistance-capacitance (RC) networks capturing the dynamic transients of UCs. In the model, u_0 denotes the voltage across the bulk capacitor C , u_1 and u_2 denote the voltages of the two RC circuits, respectively, V denotes the UC output voltage, R_s denotes the series resistance, and i represents the manipulated current.

According to the basic electrical circuit laws, the continuous state-space equation is:

$$\dot{\mathbf{x}}(t) = \mathbf{A}\mathbf{x}(t) + \mathbf{B}\mathbf{u}(t) \quad (5.1)$$

$$\mathbf{y}(t) = \mathbf{C}\mathbf{x}(t) + \mathbf{D}\mathbf{u}(t) \quad (5.2)$$

where $\mathbf{x}(t) = [u_0, u_1, u_2]^T$, $\mathbf{u}(t) = i(t)$, $\mathbf{y}(t) = V$,

$$\mathbf{A} = \begin{bmatrix} 0 & 0 & 0 \\ 0 & -\frac{1}{R_1 C_1} & 0 \\ 0 & 0 & -\frac{1}{R_2 C_2} \end{bmatrix} \quad \mathbf{B} = \begin{bmatrix} \frac{1}{C} \\ \frac{1}{C_1} \\ \frac{1}{C_2} \end{bmatrix}$$

$$\mathbf{C} = [1 \quad 1 \quad 1] \quad \mathbf{D} = R_s$$

Incorporating the impact of process and measurement noises, the state-space equation can be further formulated in a stochastic form:

$$\dot{\mathbf{x}}(t) = \mathbf{A}\mathbf{x}(t) + \mathbf{B}\mathbf{u}(t) + \mathbf{w}(t) \quad (5.3)$$

$$\mathbf{y}(t) = \mathbf{C}\mathbf{x}(t) + \mathbf{D}\mathbf{u}(t) + \mathbf{v}(t) \quad (5.4)$$

where $w(t)$ and $v(t)$ represent the process noise and the measurement noise, respectively.

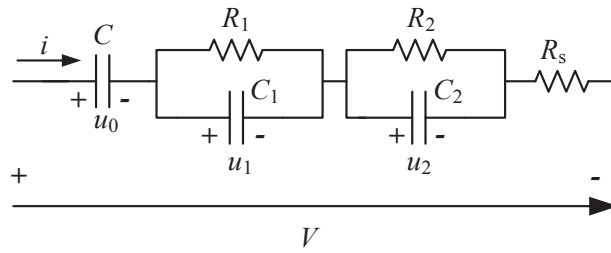


Fig. 5.1 UC model structure.

5.2.2 Model characterization

The EIS test data collected through experimentation shown in Chapter 2 was employed to characterize the dynamic model. The nonlinear least-squares algorithm was used to extract the optimal model parameters on the basis of the impedance spectrum obtained under a temperature of 20°C and a frequency range from 10 mHz to 100 Hz at 100% SOC. The derived model based on 100% SOC data has been demonstrated to have the highest accuracy in Chapter 2. Fig. 5.2 shows that the calibrated model is capable of simulating the UC impedance at the selected frequency range (especially at relative high frequencies commonly encountered in electric vehicle applications). The optimized model parameters are listed in Table 5.1.

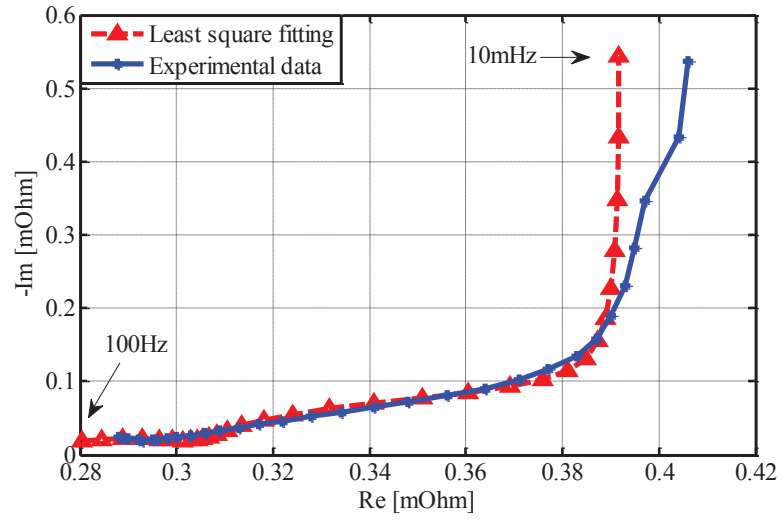


Fig. 5.2 Measured and predicted impedance spectra under 20°C at 100% SOC.

Table 5.1 The derived model parameters under 20°C at 100% SOC.

Model parameters (Unit)					
C (F)	R_s (Ω)	R_1 (Ω)	R_2 (Ω)	C_1 (F)	C_2 (F)
2959	2.68×10^{-4}	8.69×10^{-5}	3.70×10^{-5}	1095	60.7

5.3 H -infinity Observer for UC SOC Estimation

The H -infinity filter has been increasingly used to address state estimation problems with great success. The underlying beneficial properties give excellent tolerance against the unknown process and measurement noise, and intrinsic robustness against modelling uncertainty. These are desirable merits for UC SOC estimation, because the UC model parameters are highly susceptible to its operating conditions and health levels.

For ease of matrix manipulation, (5.3) and (5.4) can be rearranged to

$$\dot{\mathbf{x}}(t) = \mathbf{A}\mathbf{x}(t) + \mathbf{B}\mathbf{u}(t) + \mathbf{E}\boldsymbol{\omega}(t) \quad (5.5)$$

$$\mathbf{y}(t) = \mathbf{C}\mathbf{x}(t) + \mathbf{D}\mathbf{u}(t) + \mathbf{F}\boldsymbol{\omega}(t) \quad (5.6)$$

where $\boldsymbol{\omega}(t)=[\mathbf{w}, \mathbf{v}]^T$, $\mathbf{E}=[\mathbf{I}_0, \mathbf{0}]$, $\mathbf{F}=[\mathbf{0}, \mathbf{I}_1]$, with \mathbf{I}_0 and \mathbf{I}_1 being the identity matrix and $\mathbf{0}$ being the zero matrix with proper dimensions, respectively.

The observability of the UC model can be examined by checking the rank of the extended observatory matrix:

$$\mathbf{M}_\theta = \begin{bmatrix} \mathbf{C} \\ \mathbf{C}\mathbf{A} \\ \mathbf{C}\mathbf{A}^2 \end{bmatrix} = \begin{bmatrix} 1 & 1 & 1 \\ 0 & -\frac{1}{R_1 C_1} & -\frac{1}{R_2 C_2} \\ 0 & \frac{1}{R_1^2 C_1^2} & \frac{1}{R_2^2 C_2^2} \end{bmatrix} \quad (5.7)$$

The observatory matrix is of full rank if

$$R_1 C_1 \neq R_2 C_2 \quad (5.8)$$

Given the parameters in Table 5.1, it is evident that the UC model is observable. Then, an H -infinity observer can be expressed as follows:

$$\dot{\hat{\mathbf{x}}}(t) = \mathbf{A}\hat{\mathbf{x}}(t) + \mathbf{B}\mathbf{u}(t) + \mathbf{L}(\mathbf{y}(t) - \hat{\mathbf{y}}(t)) \quad (5.9)$$

$$\hat{\mathbf{y}}(t) = \mathbf{C}\hat{\mathbf{x}}(t) + \mathbf{D}\mathbf{u}(t) \quad (5.10)$$

where $\hat{\mathbf{x}}(t)$ and $\hat{\mathbf{y}}(t)$ are estimates of $\mathbf{x}(t)$ and $\mathbf{y}(t)$, respectively, and \mathbf{L} is the observer gain.

Thus, the error dynamics can be obtained:

$$\dot{\mathbf{e}}(t) = (\mathbf{A} - \mathbf{L}\mathbf{C})\mathbf{e}(t) + (\mathbf{E} - \mathbf{L}\mathbf{F})\boldsymbol{\omega}(t) \quad (5.11)$$

$$\mathbf{e}_y(t) = \mathbf{C}\mathbf{e}(t) \quad (5.12)$$

where

$$\mathbf{e}(t) = \mathbf{x}(t) - \hat{\mathbf{x}}(t) \quad (5.13)$$

$$\mathbf{e}_y(t) = \mathbf{y}(t) - \hat{\mathbf{y}}(t) \quad (5.14)$$

The main task of the H -infinity observer design is to find the filter (5.9) and (5.10) such that the error dynamics (5.11) and (5.12) are asymptotically stable at a specified attenuation level $\gamma > 0$, that is, satisfying the following inequality:

$$\|\mathbf{T}_{e\omega}\|_{\infty} = \sup_{\boldsymbol{\omega}} \frac{\|\mathbf{e}\|_2}{\|\boldsymbol{\omega}\|_2} \leq \gamma, \mathbf{e}(0) = \mathbf{0} \quad (5.15)$$

Many approaches have been put forward to solve the above mentioned H -infinity problem; e.g., the algebraic Riccati equation (ARE) approach, the polynomial equation approach, and the LMI based approach. The LMI method is adopted here for its computation efficiency and flexibility.

Based on *Bounded Real Lemma* from [96], the H -infinity problem (5.15) can be converted to finding an appropriate symmetric positive matrix \mathbf{P} and the filter gain \mathbf{L} such that the following inequality is satisfied:

$$\begin{bmatrix} (\mathbf{A} - \mathbf{L}\mathbf{C})^T \mathbf{P} + \mathbf{P}(\mathbf{A} - \mathbf{L}\mathbf{C}) + \mathbf{I} & \mathbf{P}(\mathbf{E} - \mathbf{L}\mathbf{F}) \\ (\mathbf{E} - \mathbf{L}\mathbf{F})^T \mathbf{P} & -\gamma^2 \mathbf{I} \end{bmatrix} < 0 \quad (5.16)$$

In order to transform (5.15) to an LMI, a new variable $\mathbf{N} = \mathbf{P}\mathbf{L}$ (i.e., $\mathbf{L} = \mathbf{P}^{-1}\mathbf{N}$) is defined, resulting in

$$\begin{bmatrix} \mathbf{A}^T \mathbf{P} + \mathbf{P} \mathbf{A} - \mathbf{C}^T \mathbf{N}^T - \mathbf{N} \mathbf{C} + \mathbf{I} & \mathbf{P} \mathbf{E} - \mathbf{N} \mathbf{F} \\ (\mathbf{P} \mathbf{E} - \mathbf{N} \mathbf{F})^T & -\gamma^2 \mathbf{I} \end{bmatrix} < 0 \quad (5.17)$$

By setting $\gamma = 1.2$, the matrices \mathbf{P} and \mathbf{N} can be derived by means of the Matlab-based toolbox *YALMIP* [97]. As state in its official website, *YALMIP* is a modelling language for advanced modelling and solution of convex and nonconvex optimization problems. It implements a large amount of tricks, allowing the user to concentrate on the high-level model, while *YALMIP* takes care of the low-level problems. After implementation, the derived \mathbf{P} and \mathbf{N} are

$$\mathbf{P} = \begin{bmatrix} 0.2587 & -0.0122 & -0.0003 \\ -0.0122 & 0.6666 & 0.0048 \\ -0.0003 & 0.0048 & 0.0112 \end{bmatrix} \quad (5.18)$$

$$\mathbf{N} = [1.1556 \quad -0.7069 \quad -0.2524]^T \quad (5.19)$$

The observer gain is

$$\mathbf{L} = [4.4145 \quad -0.8200 \quad -22.1240]^T \quad (5.20)$$

For a comparative study, the state-of-the-art Kalman filter is also employed to estimate the UC SOC. The state-space equations (5.1) and (5.2) are discretized to

$$\mathbf{x}_{k+1} = \mathbf{G} \mathbf{x}_k + \mathbf{H} \mathbf{u}_k + \mathbf{w}_k \quad (5.21)$$

$$\mathbf{y}_{k+1} = \mathbf{C} \mathbf{x}_k + \mathbf{D} \mathbf{u}_k + \mathbf{v}_k \quad (5.22)$$

where k denotes the time interval index, $\mathbf{w}(t)$ and $\mathbf{v}(t)$ represent the process and measurement noise, both of which are assumed to be Gaussian white noise with zero mean and covariance matrices of \mathbf{Q}_w and \mathbf{R}_v . The continuous H -infinity observer ((5.9) and (5.10)) can also be discretised similarly. The system matrix and the control matrix become:

$$\mathbf{G} = \begin{bmatrix} 1 & 0 & 0 \\ 0 & e^{\frac{-T}{R_1 C_1}} & 0 \\ 0 & 0 & e^{\frac{-T}{R_2 C_2}} \end{bmatrix} \quad (5.23)$$

$$\mathbf{H} = \begin{bmatrix} T/C \\ R_1(1 - e^{\frac{-T}{R_1 C_1}}) \\ R_2(1 - e^{\frac{-T}{R_2 C_2}}) \end{bmatrix} \quad (5.24)$$

where T is the sampling time. The detailed Kalman filter for the UC SOC estimation is illustrated in Fig. 5.3.

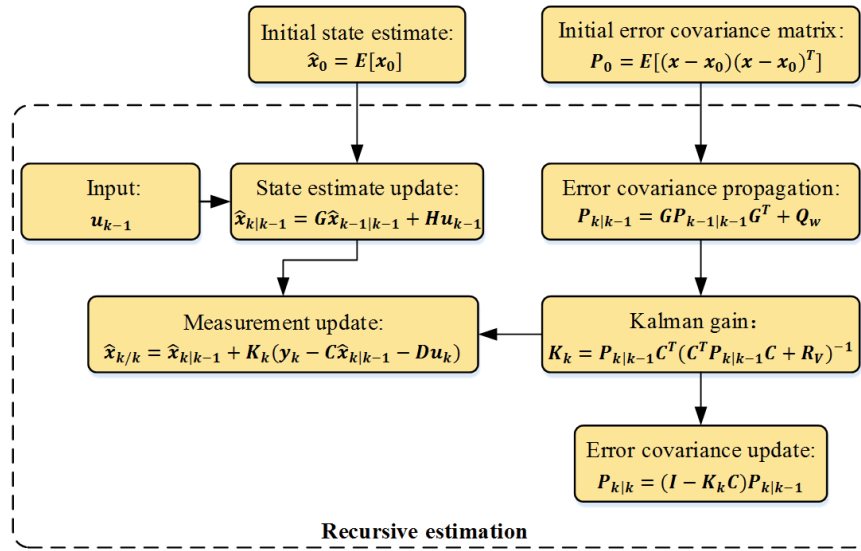


Fig. 5.3 Schematic of the Kalman filter for UC SOC estimation. ($\hat{x}_{k|k-1}$ and $\hat{x}_{k|k}$ are the prior and posterior estimate of state vector at time interval k ; $P_{k|k-1}$ and $P_{k|k}$ are the error covariance of $\hat{x}_{k|k-1}$ and $\hat{x}_{k|k}$; K_k represents the Kalman gain.)

5.4 Experimental Validation and Discussion

The test data collected through EIS tests are utilized to identify the model parameters. The accuracy and robustness against modelling uncertainty of the proposed observer is examined through the Federal Urban Driving Schedule (FUDS), a representative loading profile for UCs in electric vehicle applications. The FUDS test serves to present the typical loading conditions, but far from the wholly representative of vehicle operation. Here, the UC voltage is permitted to approach zero in order to execute the complete FUDS test. While, in real EV applications, the UC system cannot operate in such low voltage range due to the voltage limit for motor drive. It is noted that both the voltage and current were closely monitored during tests, thereby avoiding over-discharge risk.

5.4.1 Validity of the proposed H -infinity observer

The performance of the H -infinity observer is highly dependent on the attenuation level, since it is a direct indicator of the noise-to-estimate impact. However, a stringent attenuation level would cause divergence problem, resulting in the observer malfunction. Thus, taking the convergence issue into consideration, the attenuation level for the proposed H -infinity observer is given by:

$$\gamma = 1.2 \quad (5.25)$$

The covariance matrices \mathbf{Q}_w and \mathbf{R}_v for the Kalman filter were obtained via the trial-and-error method:

$$\mathbf{Q}_w = \mathbf{diag}([5.0e-6 \quad 1.0e-6 \quad 1.0e-7]), \mathbf{R}_v = 0.09 \quad (5.26)$$

Evolutions of the SOC estimates for both methods are shown in Fig. 5.4. The well-controlled coulomb counting was used to procure the reference (true) SOC based on the

integral calculation of the measured current and time. The high-accuracy current measurement capability of the test rig can ensure the validity of the reference SOC. It can be seen that the H -infinity observer predicts well the SOC of the tested UC. Its estimation accuracy is comparable to the Kalman filter. This fact highlights that the H -infinity observer is able to efficiently track the UC SOC without cumbersome and time-consuming tuning of process and measurement noise covariance.

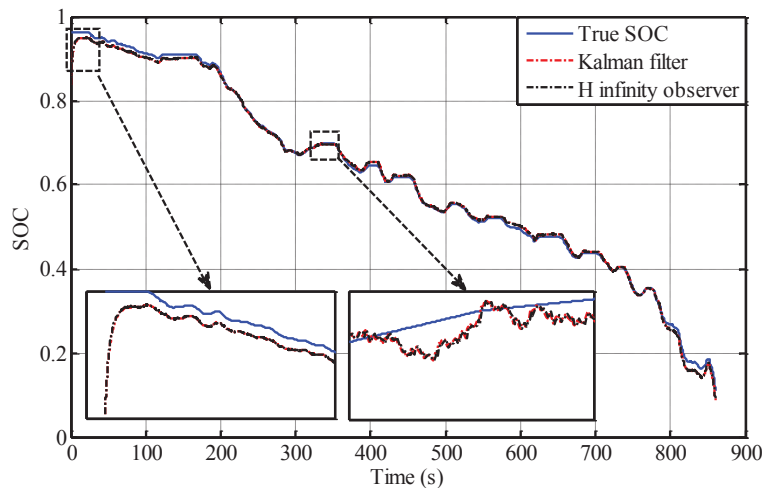


Fig. 5.4 Comparison of the H -infinity observer and the Kalman filter for the UC SOC estimation in the FUDS test at 20°C.

5.4.2 Robustness against modelling uncertainty

The UC model parameters are highly sensitive to operating conditions (e.g. temperature and SOC). Thus, the model uncertainty may make the KF-based method diverge, even though it is well-tuned in advance. Instead, the formulation of the H -infinity observer is inherently endurable to possible model variations. This property is highly appreciated since UCs always work in varying conditions, giving rise to parameter variation problems. As shown in Table 5.2, the model parameters (acquired through EIS tests) noticeably alter under different

temperatures. Figs. 5.5 to 5.7 show that the H -infinity observer, based on the model at 20°C, can still perform well under the other three temperatures and achieve SOC estimation with high accuracy. The true SOC value was calculated using the Coulomb counting method, thanks to the high precision measurement of charging/discharging current, thus guaranteeing the reference (true) SOC accuracy. Upon a further observation of these figures, it is prominent that the H -infinity observer converges much faster to the true SOC than the Kalman filter at all the temperature circumstances. It is notable that identical initial estimates were given for a fair comparison. Fig. 5.8 and Fig. 5.9 show mean absolute errors and RMS errors of the Kalman filter and H -infinity observer, respectively. It is clear that the H -infinity observer outperforms the Kalman filter under all temperatures. In particular, the performance of the H -infinity observer is most obvious at -40°C, as there exists the largest parameter change. This verifies the robustness of the proposed H -infinity observer against the modelling uncertainty, hence justifying its superiority to the state-of-the-art Kalman filter for UC SOC estimation.

Table 5.2 Model parameters under different temperatures.

Model parameters (Unit)						
T (°C)	C (F)	R_s (Ω)	R_1 (Ω)	R_2 (Ω)	C_1 (F)	C_2 (F)
-40	2835	4.05×10^{-4}	1.70×10^{-4}	1.07×10^{-4}	2601	736.2
0	2976	2.64×10^{-4}	1.13×10^{-4}	4.44×10^{-5}	976.6	40.3
40	3031	3.07×10^{-4}	4.19×10^{-5}	4.50×10^{-5}	5294	987.6

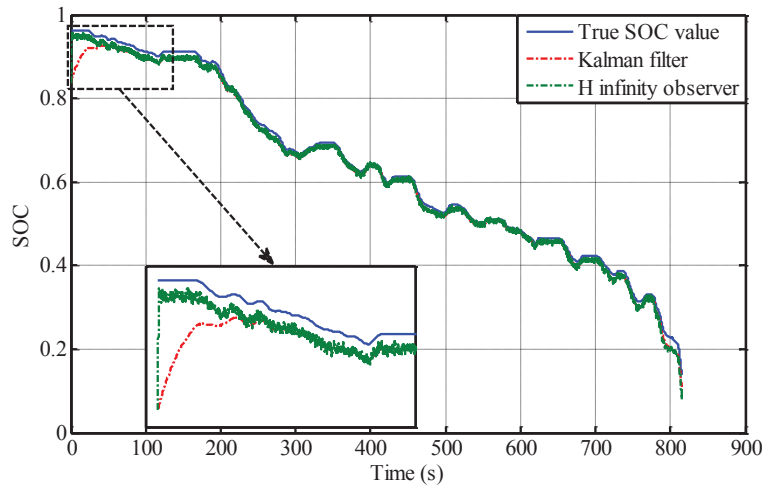


Fig. 5.5 UC SOC estimation result in the FUDS test at -40°C.

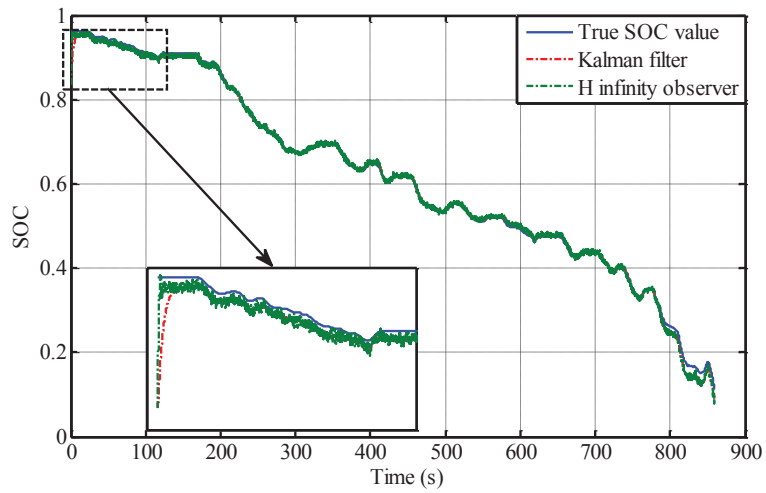


Fig. 5.6 UC SOC estimation result in the FUDS test at 0°C.

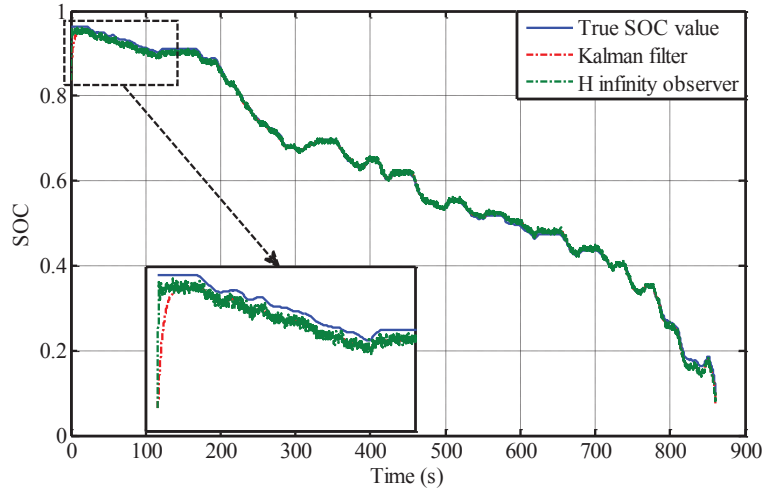


Fig. 5.7 UC SOC estimation result in the FUDS test at 40°C.

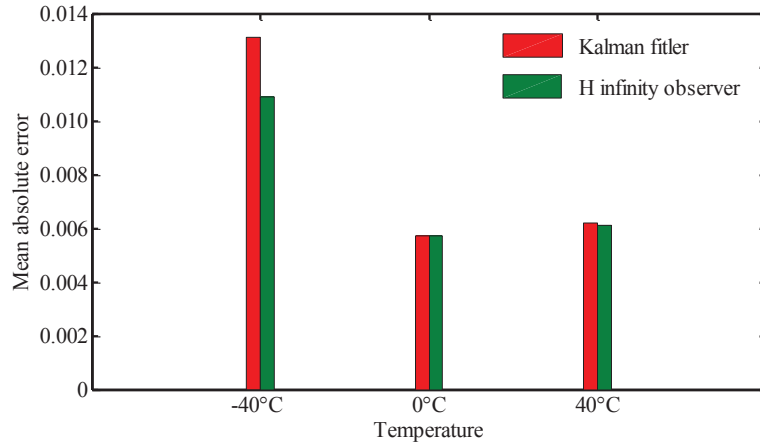


Fig. 5.8 Mean absolute errors of UC SOC estimation.

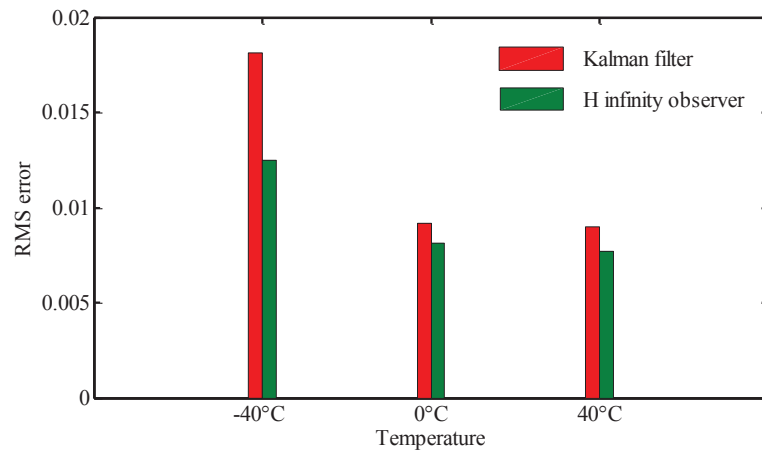


Fig. 5.9 Root-mean-square errors of UC SOC estimation.

5.5 Summary

This chapter presents a robust H -infinity observer for the estimation of the UC SOC. Compared to the state-of-the-art KF-based estimation methods, the proposed approach does not need any statistical information about process and measurement noises during operations, which eliminates the heuristic, error-prone, troublesome, and time-consuming tuning process. Its estimation accuracy can be ensured by minimizing the attenuation level. Moreover, it is less computationally intensive because the observer gain is synthesized offline rather than recursive gain calculation in the KF-based algorithms. The validation outcome substantiates that the H -infinity observer can estimate the UC SOC with comparable accuracy to the Kalman filter, given an exact model. Its robustness against modelling uncertainty is proven by taking varying temperatures into account, therefore justifying an enhanced extrapolation/generalization capability.

6 Fractional-order Modelling and SOC Estimation for Ultracapacitors

6.1 Motivation

Fractional-order models have attracted increasing interest in the area of energy storage devices, including both batteries and UCs [56][57][62]. They exhibit a better capability for the fitting of experimental data with fewer model parameters, this is in contrast to their integer-order counterparts. For example, Riu *et al.* [58] introduced a half-order model for UCs that dramatically reduced the model order while retaining certain accuracy. However, the fixation of the fractional differentiation order significantly restricted the model accuracy. Martynyuk *et al.* [59] presented a fractional-order model of an electrochemical capacitor, in which the model parameters were estimated by the least-squares fitting of impedance data. Bertrand *et al.* [60] deduced a non-linear fractional-order model from a set of linear equations resulting from the frequency analysis of UCs, where the model parameters were also estimated in the frequency domain. Such a treatment proved to be reliable in a specialized laboratory environment, since the UC impedance spectra can be steadily and precisely obtained over a range of frequencies via the EIS technique. Nonetheless, the model precision may be severely compromised when exposed to varying loading conditions in real-world operations because the model parameters can be highly sensitive to such conditions.

In order to overcome these issues, this chapter proposes a novel fractional-order model that comprises a series resistor, a CPE, and a Warburg-like element, with the primary goal to accurately emulating the UC behaviour. The Grünald-Letnikov derivative (GLD) is then used to perform the model discretization in a straightforward manner. The model parameters,

including the order coefficients, are calibrated using time-domain experimental data collected through the FUDS test. Based on the fractional-order model, a fractional Kalman filter is further developed to track the UC SOC in real time. Extensive experimental data are applied to demonstrate the effectiveness of the developed model and estimation scheme. To the best of the author's knowledge, this scheme is the first known application of fractional-order calculus to both modelling and SOC estimation in UCs.

6.2 Background and Fundamentals of Fractional-Order Calculus

Fractional-order calculus (FOC) is a natural generalization of integral-order and differential calculus, which was firstly mentioned by Leibnitz and L'Hospital in their correspondence letter in 1697. By permitting integral-differential calculus operations with arbitrary or even complex order coefficients, it significantly improves the modelling ability and applicability. With the continuous advance in calculation methods for fractional-order differential equations, fractional-order modelling is a rapidly growing area of research. Meanwhile, studies have shown that some physical systems can be better characterized by fractional-order models; e.g., permanent magnet synchronous motors, flexible robots with viscoelastic materials, and physical systems with mass transfer and diffusion phenomena [98][99]. Three main definitions of FOC have emerged, namely, the Grünald-Letnikov (GL) definition, the Riemann-Liouville (RL) definition, and the Caputo definition [100]. The Grünald-Letnikov fractional-order derivative has been chosen for implementation in this work because it can discretise the continuous fractional-order model in a concise and straightforward fashion.

The detailed Grünald-Letnikov derivative formulation is

$${}_{t_0}^G D^\gamma x(t) = \frac{1}{h^\gamma} \sum_{j=0}^{\lceil t/h \rceil} (-1)^j \binom{\gamma}{j} x(t - jh) \quad (6.1)$$

where ${}_{t_0}^G D^\gamma$ represents the integral-differential operator with respect to the variable t , and γ is the integral-differential order ($\gamma \in R$, when $\gamma > 0$, ${}_{t_0}^G D^\gamma$ means fractional derivative; when $\gamma < 0$, ${}_{t_0}^G D^\gamma$ stands for fractional integral; when $\gamma = 0$, ${}_{t_0}^G D^\gamma = 1$). The initial time $t_0=0$ is

always omitted in the expression when it starts with 0, h denotes the sampling time interval,

$[t/h]$ represents the memory length, and $\binom{\gamma}{j}$ stands for Newton binomial coefficient derived

from

$$\binom{\gamma}{j} = \frac{\gamma!}{j!(\gamma-j)!} = \frac{\Gamma(\gamma+1)}{\Gamma(j+1)\Gamma(\gamma-j+1)} \quad (6.2)$$

with $\Gamma(\cdot)$ being the Gamma function defined by

$$\Gamma(\theta) = \int_0^{\infty} t^{\theta-1} e^{-t} dt \quad (6.3)$$

6.3 Fractional-Order Modelling and Characterization of UCs

The dynamic model of a UC consists of an Ohmic resistor to represent the conduction resistance of carrier charges through electrolyte and metallic conductors, a bulk capacitor to account for the main capacitance, and RC (resistor-capacitor) networks to capture the charge distribution and diffusion. These idealized components are, however, insufficient to represent the entire diffusion dynamics inside a UC. As a result, in order to increase the modelling fidelity, a fractional-order model topology can be used where a CPE and a Warburg-like element substitute for the bulk capacitor and the RC networks (see Fig. 6.1). Note that the single model input is the charging/discharging current I , while the measured voltage is the UC model output V .

The impedance of the CPE, Z_{CPE} , can be expressed as

$$Z_{CPE} = \frac{1}{Cs^\alpha} \quad (6.4)$$

where C is a constant which accounts for the main capacitance effect of the CPE, s is a complex variable, and α ($\alpha \in R, 0 \leq \alpha \leq 1$) is the fractional-order coefficient. Equation (6.4) represents an ideal capacitor when $\alpha = 1$. The parallel combination with a charge-transfer resistor serves to capture the diffusion and charge distribution dynamics inside the UC. The flexibility of the varying fractional-order coefficient is expected to produce a better modelling capability [101]. The Warburg-like element is used to describe the main capacitance, whose impedance can be represented by

$$Z_w = \frac{1}{Ws^\beta} \quad (6.5)$$

where W represents the capacitance coefficient, and $\beta(\beta \in R, 0 \leq \beta \leq 1)$ denotes the capacitance dispersion. It can be noted that the Warburg-like element becomes a resistor when $\beta = 0$, and a capacitor when $\beta = 1$. The impedance of the fractional-order model can be deduced from

$$Z_f = R_s + \frac{R_c}{1 + CR_c s^\alpha} + \frac{1}{Ws^\beta} \quad (6.6)$$

where R_s is the series resistance, and R_c is the charge transfer resistance in parallel with the CPE. The transfer function of the fractional-order model is thereby presented by:

$$\frac{V(s)}{I(s)} = R_s + \frac{R_c}{1 + CR_c s^\alpha} + \frac{1}{Ws^\beta} \quad (6.7)$$

where $V(s)$ denotes the measured output voltage of the tested UC, and $I(s)$ denotes the working current with a positive value representing the charging current. Equation (6.7) can be further reformulated as a fractional-order differential equation where

$$\begin{aligned} & (W \cdot D^\beta + CR_c W \cdot D^{\alpha+\beta}) \cdot V(t) \\ & = (R_c W \cdot D^\beta + CR_c \cdot D^\alpha + R_s W \cdot D^\beta + R_s CR_c W \cdot D^{\alpha+\beta} + 1) \cdot I(t) \end{aligned} \quad (6.8)$$

Numerical methods are necessary for solving of general fraction-order differential equations (such as (6.8)) since analytic solutions are only available in special cases. The main idea behind numerical methods lies in approximating fractional-order derivatives using integral-order derivatives, based on an appropriate approach, such as polynomial interpolation, Gauss interpolation, and fractional linear multistep methods [102]. In this Chapter, the GLD method is used to approximate the continuous fractional-order model because it is straightforward and readily implementable.

A closer observation of (6.8) indicates that there are six independent parameters to be estimated, which can be represented as

$$\theta = [\alpha \quad \beta \quad R_s \quad R_c \quad C \quad W]^T \quad (6.9)$$

Equation (6.8) can be approximated by high-order difference equations, based on the short memory principle proposed by Podlubny [103]. Only recent past points are involved in such an approximation, which effectively mitigates the computational intensity. Accordingly, the fractional-order model is approximated by

$$\begin{cases} LL: \sum_{j=0}^N (-1)^j \left[\frac{W}{\Delta T^\alpha} \binom{\beta}{j} + \frac{CR_c W}{\Delta T^{\alpha+\beta}} \binom{\alpha+\beta}{j} \right] y(t-j\Delta T) \\ RR: \sum_{j=0}^N (-1)^j \left[\frac{CR_c}{\Delta T^\alpha} \binom{\alpha}{j} + \frac{W}{\Delta T^\beta} (R_s + R_c) \binom{\beta}{j} + \frac{R_s CR_c W}{\Delta T^{\alpha+\beta}} \binom{\alpha+\beta}{j} \right] u(t-j\Delta T) \end{cases} \quad (6.10)$$

where *LL* and *RR* mean the left side and right side of the equation, *N* is the number of involved points (*N* = 3 in this work), ΔT is the sampling time, and $y(t)$ and $u(t)$ are the output voltage V and the input current I , respectively.

Based on the FUDS test data, the GA was used to search for the optimal model parameters. The derived optimal model parameters are summarized in Table 6.1. The comparison of the measured voltage and model output at 20°C is illustrated in Fig. 6.2. It is apparent that the identified model can well predict the voltage evolution in the FUDS test. Similar results can be observed at other temperatures. The current and SOC in the FUDS are shown in Fig. 6.3.

In order to further verify the fractional-order modelling ability, the model performance is compared with the dynamic model in the frequency domain under different temperatures at 100% SOC. The experimental data was collected by the EIS method using the test rig. A comparison of the results is given in Fig. 6.4. It can be seen that both the fractional-order

model and dynamic model can emulate the impedance with high accuracy over temperatures from -40°C to -20°C . However, in contrast, the fractional-order model can better capture the UC impedance characteristics at the temperatures of 0°C , 20°C , and 40°C , especially over the low-frequency band. This highlights the usefulness of the fractional-order UC modelling.

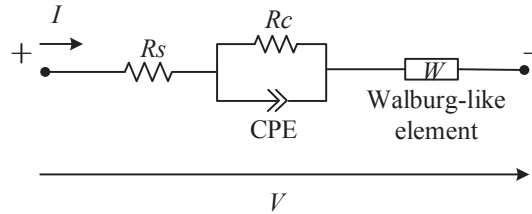


Fig. 6.1 Fractional-order model structure.

Table 6.1 The derived model parameters.

Parameter	α	β	$R_s(\text{Ohm})$	$R_c(\text{Ohm})$	C	W
-40°C	0.929	0.953	4.1×10^{-4}	2.2×10^{-4}	993	2764
-20°C	0.984	0.978	3.4×10^{-4}	1.5×10^{-4}	1038	2848
0°C	0.948	0.954	2.8×10^{-4}	1.0×10^{-4}	916	2933
20°C	0.971	0.975	3.0×10^{-4}	8.6×10^{-5}	854	2880
40°C	0.972	0.973	3.1×10^{-4}	7.3×10^{-5}	1210	3012

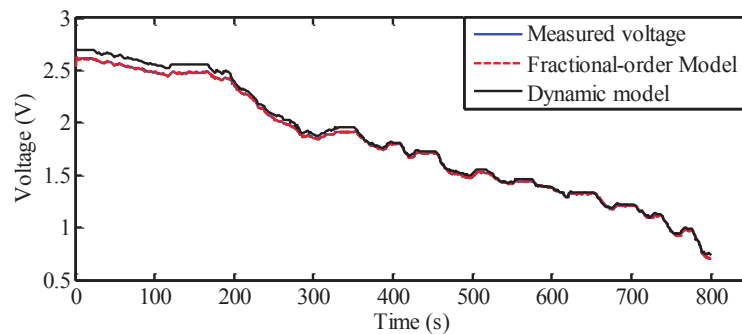


Fig. 6.2 Comparison of measured voltage, fractional-order model, and dynamic model in FUDS test at 20°C .

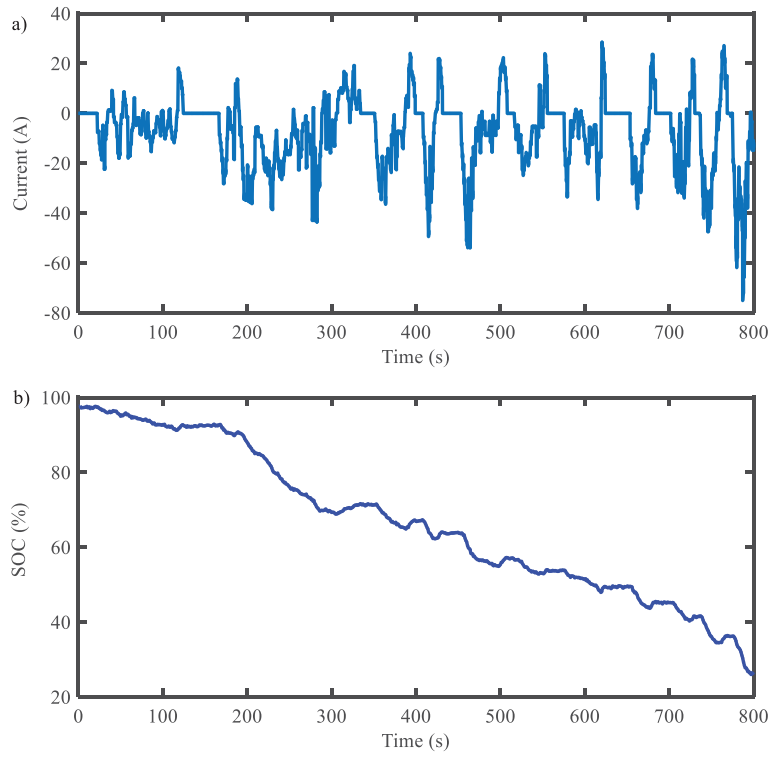
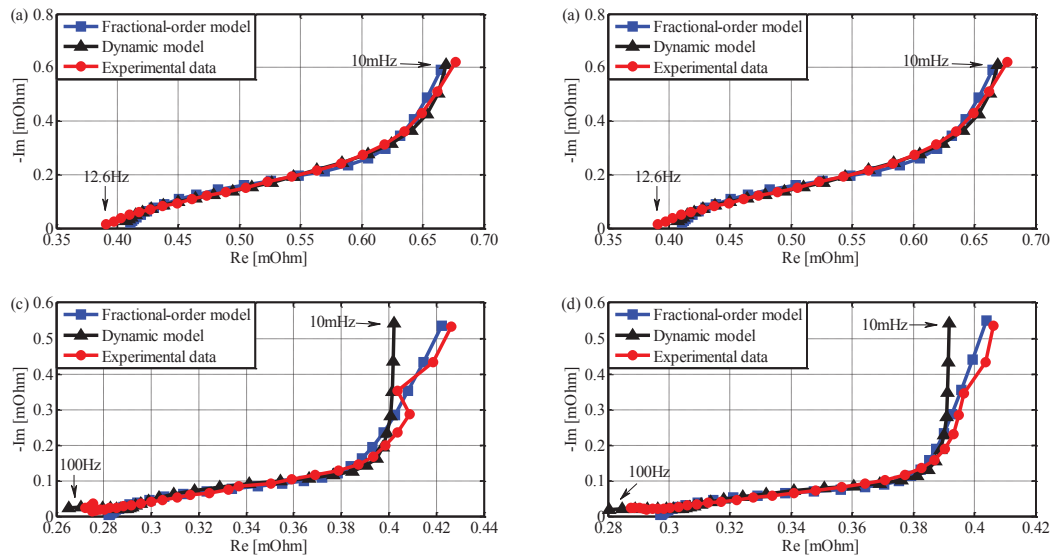


Fig. 6.3 The evolution of current and SOC in FUDS test at 20°C.



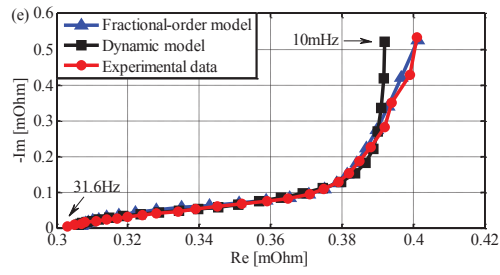


Fig. 6.4 Impedance spectra comparison at 100% SOC at the temperatures of (a) -40 °C; (b) -20 °C; (c) 0°C; (d)20°C; (e) 40 °C.

6.4 Fractional Kalman Filter for UC SOC Estimation

Accurate SOC estimation is highly desirable for optimal energy management and power control of UC systems, since it facilitates taking advantage of the UC power potential without incurring unfavourable over-charge/over-discharge. The Kalman filter methods have been widely and successfully deployed for SOC estimation of batteries and UCs. Based on the fractional-order model; here, a fractional Kalman filter is synthesized as the UC SOC gauge.

The continuous state-space equation of the fractional model can be expressed as

$$\begin{cases} \frac{d^\alpha V_1}{dt} = -\frac{V_1}{CR_c} + \frac{I}{C} \\ \frac{d^\beta V_2}{dt} = \frac{I}{W} \\ \frac{dz}{dt} = \frac{I}{3600C_n} \end{cases} \quad (6.11)$$

where V_1 and V_2 denote the voltages across the CPE and the Warburg-like element, respectively, z represents the SOC, and C_n denotes the nominal capacity of the tested UC. The output voltage is thus governed by

$$V = V_1 + V_2 + R_s \cdot I \quad (6.12)$$

Accordingly, the discrete fractional state-space model can be developed:

$$\begin{cases} x_{k+1} = A_\gamma x_k + B_\gamma u_k + \omega_k - \sum_{j=2}^{k+1} (-1)^j \Theta_j x_{k+1-j} \\ y_k = Cx_k + Du_k + v_k \end{cases} \quad (6.13)$$

where $A_\gamma = (h^\gamma A + \gamma I)$ is the system matrix, $B_\gamma = h^\gamma B$ is the control matrix,

$$C = [1 \quad 1 \quad 0], \quad D = R_s, \quad x_k = \begin{bmatrix} V_1 \\ V_2 \\ z \end{bmatrix} \text{ is the state vector at time } k, \quad \gamma = \begin{bmatrix} \alpha \\ \beta \\ 1 \end{bmatrix} \text{ is the derivative}$$

order, and $\Theta_j = \text{diag} \left[\begin{pmatrix} \alpha \\ j \end{pmatrix} \begin{pmatrix} \beta \\ j \end{pmatrix} \begin{pmatrix} 1 \\ j \end{pmatrix} \right]$. Here, h denotes the sample time, ω_k and ν_k represent the process noise and the measurement noise, both of which are assumed to be Gaussian white noise with zero mean and the covariance of Q and R , respectively.

At each time step, the following time update and measurement update are sequentially performed to realize the online UC SOC tracking.

Time update:

$$\begin{cases} \hat{x}_{k|k-1} = A_\gamma \hat{x}_{k-1} + B_\gamma u_{k-1} - \sum_{j=2}^k (-1)^j \Theta_j \hat{x}_{k-j} \\ P_{k|k-1} = A_\gamma P_{k-1} A_\gamma^T + Q_{k-1} + \sum_{j=1}^k \Theta_j P_{k-j} \Theta_j^T \end{cases} \quad (6.14)$$

where $\hat{x}_{k|k-1}$ and $P_{k|k-1}$ are the a priori state estimation and error covariance at time k , respectively; \hat{x}_{k-j} and P_{k-j} are a posteriori state estimation and error covariance at time $k-j$, respectively.

Measurement update:

$$\begin{cases} \hat{x}_k = \hat{x}_{k|k-1} + K_k (y_k - C \hat{x}_{k|k-1} - D u_k) \\ P_k = (I - K_k C) P_{k|k-1} \end{cases} \quad (6.15)$$

where K_k is the Kalman gain given by

$$K_k = P_{k|k-1} C^T (C P_{k|k-1} C^T + R_k)^{-1} \quad (6.16)$$

6.5 Experimental Validation

Two driving-cycle tests, i.e. the DST and FUDS, are considered for validating the SOC estimator. Their current profiles are shown in Fig. 6.5. The well-controlled Coulomb counting method was used to calculate the reference SOC for benchmarking purposes. The current measurement error reaches as low as 1 mA so that the fidelity of reference SOC can be justified. For the fractional filter implementation, the process and measurement covariance, namely \mathbf{Q} and \mathbf{R} , were consciously chosen by trial-and-error to ensure algorithm convergence. The initial estimate \hat{x}_0 , initial error covariance P_0 , process noise covariance Q , and measurement noise covariance R are assigned as follows. A deviant initial estimate was deliberately designated as 0.8 (the true SOC value is 0.97).

$$\hat{x}_0 = [0.02 \quad 2.0 \quad 0.8]^T$$

$$P_0 = \begin{bmatrix} 0.001 & 0 & 0 \\ 0 & 0.0002 & 0 \\ 0 & 0 & 0.005 \end{bmatrix}$$

$$Q = \begin{bmatrix} 0.0001 & 0 & 0 \\ 0 & 0.0005 & 0 \\ 0 & 0 & 0.002 \end{bmatrix}$$

$$R = 0.00005$$

The evolutions of the estimated SOC and true SOC in both tests at 20°C are showcased in Fig. 6.6. It is apparent that the estimated SOC can quickly offset the initial error and closely track the true SOC in both dynamic tests. As verified in Fig. 6.7, the estimation errors are bounded within 1% and 2% in DST and FUDS tests, respectively. The results at other temperatures are analogous, further proving the applicability of the proposed method.

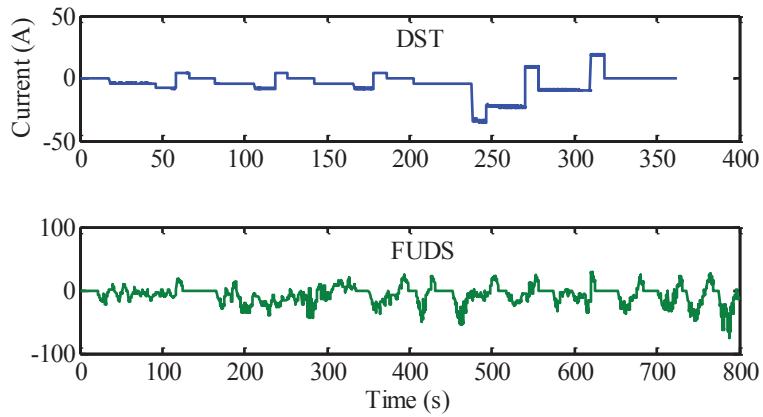


Fig. 6.5 The DST and FUDS current profiles.

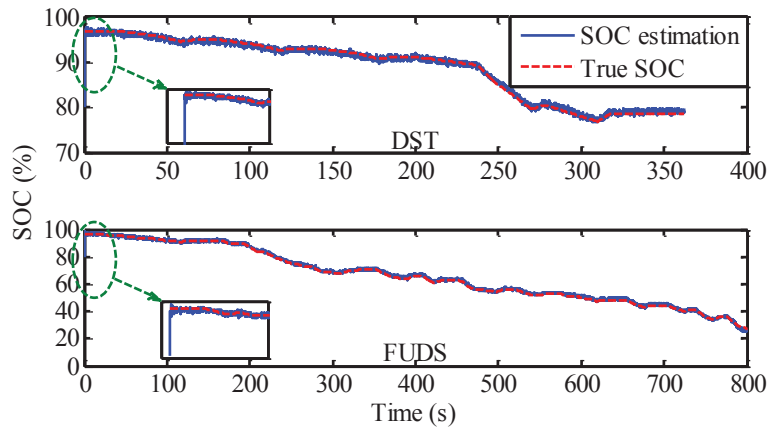


Fig. 6.6 SOC estimates at 20°C.

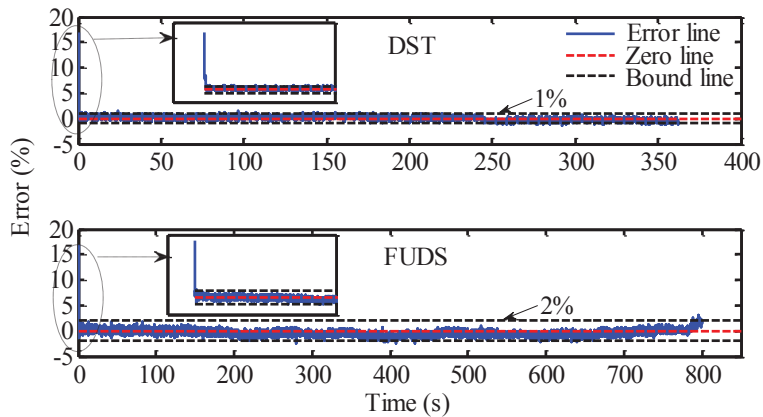


Fig. 6.7 Estimation errors at 20°C.

6.6 Summary

In this chapter, a fractional-order ultracapacitor (UC) model comprising a series resistor, a CPE, and a Warburg-like element has been proposed to capture the UC dynamics. The Grünald-Letnikov fractional-order derivative has been used to discretise the fractional-order model. The model parameters including the order coefficients are identified through the GA, based on the time-domain FUDS test data. The impedance spectrum investigation under different temperatures further confirms a higher precision of the fractional-order model than the integral-order dynamic model. A fractional Kalman filter, moreover, has been devised to estimate the UC SOC. The validation results corroborate that the SOC estimator can well track the true SOC, and the associated errors are less than around 2% in dynamic driving-cycl-based tests.

7 Multi-Objective Optimal Sizing of Hybrid Energy Storage System for Electric Vehicles

7.1 Motivation

The ESS is a key ingredient of an EV and significantly affects its driving performance and cost effectiveness. The exploration of an eligible vehicular ESS poses a challenge, because of high power/energy demand and unpredictable driving environments in EVs. Many potential ESSs have been reported and analysed in the literature, among which lithium-ion batteries represent one main choices, due to their high mass and volume energy densities [104][105]. However, the drawbacks of relatively low power density and susceptibility to high-rate power cycling always leads to battery oversizing in order to meet high power transients under realistic driving conditions, thereby inevitably incurring excess expense. Frequent charging and discharging operations of batteries tend to have adverse effects on battery durability [106]. The advantages of UCs have already been discussed and they make a good addition to high-energy ESSs in conjunction with lithium-ion batteries to form a hybrid energy storage system - HESS. This can fully leverage the synergistic benefits of both devices [107]. In such an ESS, batteries are often used to fulfil the average power demand, whereas UCs are mainly responsible for offering transient high-power delivery. This can help alleviate stresses on the batteries during hard accelerations and regenerative braking in aggressive decelerations.

HESS sizing is critical to the drivability and cost of an EV. Some preliminary insights into optimal HESS sizing have been given in the literature [108][109][110]. Generally, the transient power requirements are usually formulated as optimization constraints, while manufacturing cost, system efficiency, or fuel economy are often selected as optimization objectives [111].

The energy management of an HESS is important for improving operational performance and enhancing system efficiency. There are a number of approaches that have been proposed and analysed in the literature for implementing power split within a HESS [112][113]. For instance, an intuitive power control scheme of an HESS for an electric vehicle was analysed for the Urban Dynamometer Driving Schedule (UDDS) through the simulation in Matlab/Simulink environment [114]. A rule-based energy management strategy was also proposed and evaluated under several different driving cycles in simulation [115]. These methodologies have advantages of intuitiveness and ease of implementation, but cannot realize the optimal power allocation, with respect to some criteria, such as electricity consumption minimization. They may not sufficiently harness the HESS potential, or even induce malfunctions, such as over-charging/over-discharging and thermal runaway, bringing about system deterioration.

In order to realize the optimal power management of an HESS, optimization-based methods have been applied; there are associated issues such as algorithm complexity and driving cycle dependency. For example, Dynamic Programming (DP) and Model Predictive Control (MPC) have been both used to allocate power demand between battery and UC packs, with the aim of subduing battery current variations and improving system efficiency with an

appropriate UC control [116]. Likewise, power coordination of HESSs was cast as a convex optimization problem, and then solved by general solvers in polynomial time [117].

Furthermore, energy management strategies are closely coupled with powertrain component sizing, as presented in hybrid vehicle studies [118]. An integrated optimization approach was also proposed to simultaneously achieve the optimal sizing and energy management synthesis of HESSs, where a bi-loop optimization structure was employed [119]. Nevertheless, the search for optimal sizing parameters in the outer loop and the rule-based control strategy refinement in the inner loop proved to be computationally expensive, hindering its practicality. It is also still possible for the solution to be trapped at local minima.

Previous studies failed to simultaneously take the ESS weight, cost and battery health into account, with their coupling effects on ESS sizing insufficiently studied. Also, a computationally efficient power split strategy is absent in the existing literature when considering an optimally sized HESS. To bridge these issues, this chapter presents an integrated framework of the optimal sizing and energy management of an HESS for an example electric vehicle. The primary purpose is to search for the optimal HESS size through a multi-objective optimization algorithm considering the battery health status, HESS weight and manufacturing cost. To this end, a battery state-of-health (SOH) model is incorporated to quantitatively investigate the impact of component sizing on the battery lifetime under the constraints of driving performance requirements. It is well known that battery aging is influenced by on-board energy management strategies [120]. A wavelet-transform technique is adopted here to perform the real-time power allocation, with the drive to assign high-frequency components of load profile to the UC bank, and the rest to the battery pack. The UDDS is used to simulate the load profile during practical EV operation, which serves as the

example target of wavelet-transform. The interactions between the HESS weight, cost and battery health are thoroughly investigated and fully illustrated. The findings provide a good insight into realistic HESS sizing that emphasizes different optimization objectives.

7.2 Battery SOH Model

The accepted advantage of an HESS is to keep the batteries away from frequent charging and discharging and peak power operation. This is believed to benefit battery life preservation, which remains one of the consistent technical challenges hindering market penetration and mass-adoption of EVs. An accurate battery SOH model is needed since it closely maps the battery health state. Its influencing factors are the basis for health-conscious energy management system development. Numerous efforts have been directed towards exploring battery aging mechanisms and developing reliable battery SOH models [121][122][123]. Accordingly, different models were established from perspectives of parasitic side reactions [121], solid-electrolyte interface formation [122], and resistance increase [123]. However, the high computation requirement and burdensome calibration process made these models unfeasible for practical use. Alternatively, temperature, discharge-rate and depth-of-discharge (DOD) have been identified as the main causes to battery aging, and thus used to build a semi-empirical model [124]. Furthermore, it was pointed out that temperature and current rate play more significant roles in capacity fade of the tested batteries while the impact of DOD is negligible. The semi-empirical model developed in [124] is adopted here to quantitatively account for the correlation between the battery capacity fade and the discharged ampere-hour throughput, which is expressed as:

$$Q_{loss} = B(c) \cdot \exp\left(\frac{-E_a}{RT}\right) H^Z \quad (7.1)$$

where Q_{loss} is the percentage of capacity loss, c is the discharge-rate, $B(c)$ is the pre-exponential factor depending on the discharge-rate c as shown in Table 7.1 (the real-time value can be obtained through cubic interpolation), E_a is the activation energy in J/mol, R is

the gas constant (8.1 J/mol•K), T is the absolute temperature of the battery (it is assumed to be constant at 298.15K during operations through an efficient thermal management), H is the discharged Ah throughput, and z is the power law factor. The activation energy E_a and the power law factor z are extracted using the test data as

$$\begin{cases} E_a = 31700 - 370.3c \\ z = 0.55 \end{cases} \quad (7.2)$$

A capacity fade of 20% nominal capacity is usually taken as the end-of-life (EOL) point of EV batteries, therefore the total Ah can be deduced as

$$H = \left(\frac{20}{B(c) \exp\left(\frac{-E_a(c)}{RT}\right)} \right)^{\frac{1}{z}} \quad (7.3)$$

Assuming a symmetric capacity during charge and discharge processes, the charge cycles up to the battery EOL can be further derived:

$$N = \frac{3600H}{Q_{B_cell}} \quad (7.4)$$

where Q_{B_cell} denotes the nominal battery capacity in As. The energy throughout the battery SOH lifetime is

$$\text{SOH}(t) = 1 - \frac{1}{2N \cdot Q_{B_cell} \cdot V_{B_cell}} \int_0^t |I_b(\tau) \cdot V_{B_cell}| d\tau \quad (7.5)$$

where V_{B_cell} is the nominal voltage of battery in V, I_b is the battery load current in A. Then, the SOH change rate can be derived as

$$\frac{d\text{SOH}(t)}{dt} = \frac{-|I(t)|}{2 \cdot N(|I(t)|) \cdot Q_{B_cell}} \quad (7.6)$$

The relationship between the number of cycles and the SOH change rate with regards to the discharging rate are shown in detail in Fig. 7.1. The SOH change rate indicates the battery degradation rate. It is evident that the number of cycles peaks at 4 C-rate while the SOH deteriorates more significantly with increasing C-rate.

Table 7.1 Pre-exponential factor as a function of C-rate.

C-rate ^a	0.5C	2C	6C	10C
<i>B</i> values	31630	21681	12934	15512

^a1 C-rate corresponds to 2A.

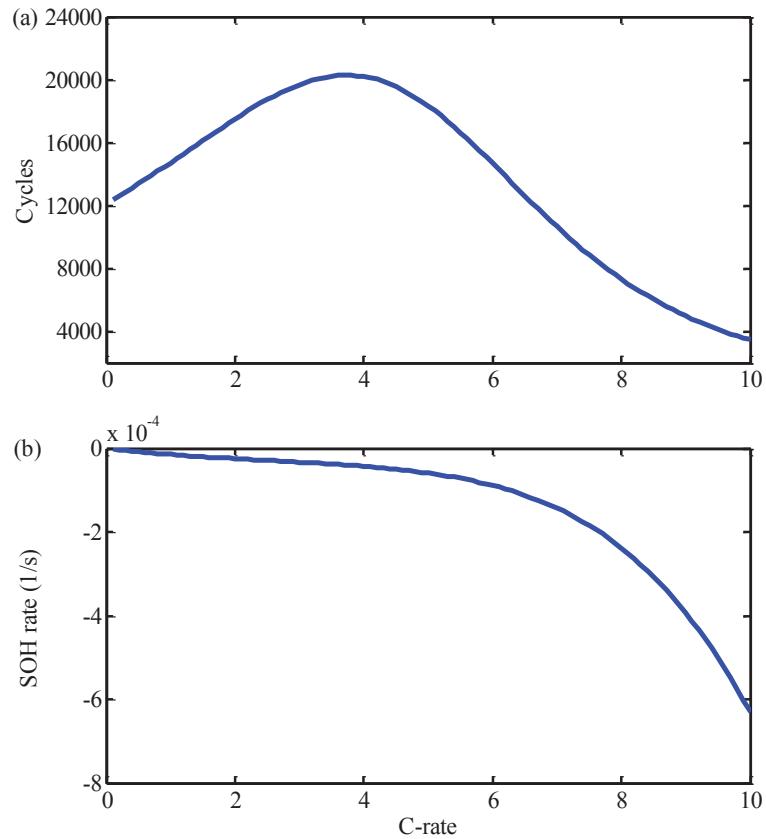


Fig. 7.1 (a) number of cycles until EOL; (b) SOH change rate.

7.3 Powertrain Modelling

7.3.1 Powertrain configuration

There are three main HESS configurations in relation to the number of DC-DC converters and system deployment patterns [125]. They are passive, semi-active and fully-active HESS; each with strengths and limits. Generally, the passive HESS connects the battery and UC packs in parallel, and directly couples to the load without any power electronic converter. The voltage of the UC pack is thus bound to battery voltage, which usually exhibits low change during operation. This means that the power potential of the UCs may not be well utilized because of the inherent relationship between the voltage and its delivered energy [104]. The fully active HESS gives the best performance by employing two DC-DC converters. It has increased complexity and manufacturing cost. The semi-active HESS seems to be a good trade-off between performance and circuit complexity by introducing only one additional DC-DC converter and the relatively simple control circuitry. A UC series configuration in a semi-active hybrid is chosen in this chapter because it permits the voltage of the UC pack to vary over a wide range, which contributes to a better use of the stored energy and power. An example electric vehicle is chosen in this study with its powertrain illustrated in Fig. 7.2. The basic vehicle parameters are listed in Table 7.2. A DC-DC converter is placed between the UC pack and DC bus to regulate the UC current flow from/to the DC bus. This is controlled by the control unit. The gap between the power demand from the electric motor (EM) inverter and the UC pack output is offset by the battery pack. The electric motor not only works to provide the driving torque in propulsion mode, but also functions as a generator to charge the UC pack by regenerative braking in deceleration mode. The EM efficiency and torque limits

are illustrated in Fig. 7.3. It is worth mentioning that the stored energy in the UC pack can be harnessed in future accelerations or hill-climbing conditions to fulfil the peak power demands. This is a typical torque/speed curve for a hybrid or electric vehicle and it exhibits the characteristic narrow constant torque region before entering into an extended constant power (or field weakening) region [126]. The transmission reduces the speed with a fixed gear ratio while maintaining good efficiency under different working conditions.

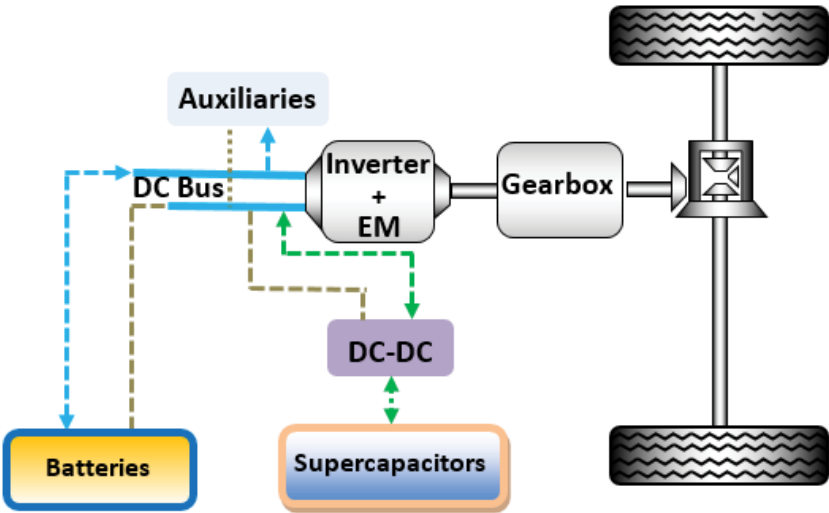


Fig. 7.2 The powertrain illustration of the example electric vehicle with HESS.

Table 7.2 Basic vehicle parameters.

Parameters (unit)	Value
m_0 , curb mass without HESS (kg)	1480
g , gravity acceleration (m ² /s)	9.81
f , rolling resistance coefficient	0.09
C_D , air drag coefficient	0.335
A , front area (m ²)	2.0
ρ , air density (kg/m ³)	1.2
η_T , transmission efficiency	0.96
δ , correction coefficient of rotating mass	1.11
k , gear ratio	6.65
R_{tire} , rolling radius of tire	0.3107

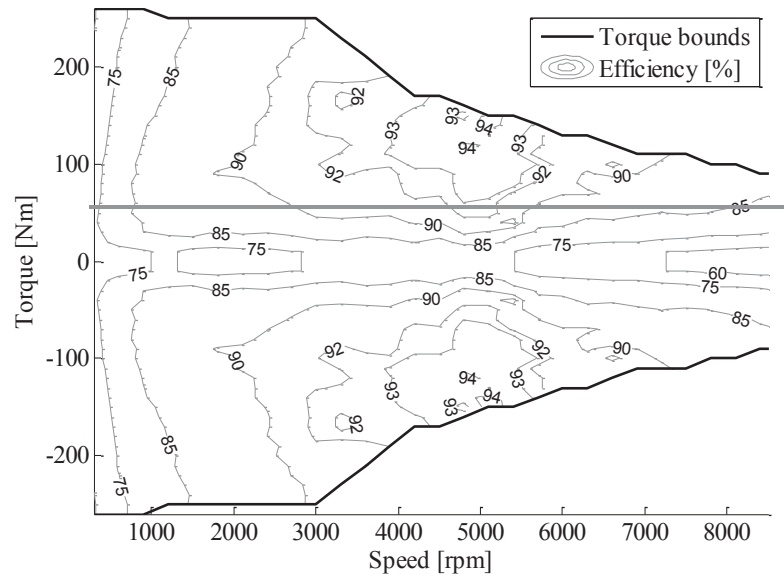


Fig. 7.3 EM efficiency and torque bounds.

7.3.2 Battery modelling

The *Rint* model, as shown in Fig. 7.4(a), is used here to represent the battery dynamics. It has simplicity and accuracy. In order to reach the required voltage level for the motor drive, and minimal capacity for ensuring a certain driving range, a battery pack composed of n_{bp} parallel strings with each containing n_{bs} series connected cells is deployed in the example

electric vehicle. It is worth noting that the parallel connections of cell strings also facilitate the enhancement of the power delivery capability of the battery pack. The main specification of the battery cell is shown in Table 7.3, while the main parameters of the battery pack are derived from

$$\begin{cases} Q_{BATT} = n_{bs} n_{bp} Q_{B_cell} \\ R_{BATT} = \frac{n_{bs} R_{B_cell}}{n_{bp}} \\ V_{BATT} = n_{bs} V_{B_cell} \end{cases} \quad (7.7)$$

where Q_{BATT} and V_{BATT} denote the capacity and the terminal voltage of the battery pack, n_{bs} denotes the number of series connected battery cells, n_{bp} denotes the number of parallel connected battery cell strings, R_{B_cell} is the battery cell resistance, Q_{B_cell} is the nominal cell capacity, and V_{B_cell} is the battery cell nominal voltage.

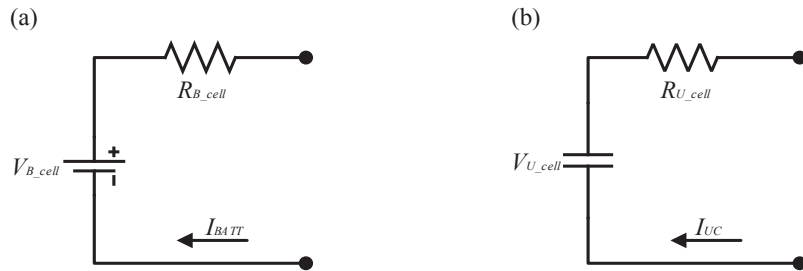


Fig. 7.4 (a) Battery; (b) UC model.

Table 7.3 Main specifications of battery.

Parameter (unit)	Value
Nominal cell voltage V_{B_cell} (V)	3.3
Cell Capacity Q_{B_cell} (As)	8280
Cell resistance R_{B_cell} (Ohm)	0.01
Cell unit cost c_b (USD)	6.5
Cell mass m_b (kg)	0.07

7.3.3 UC modelling

In contrast to the high energy density of batteries, UCs have high power density, low internal resistance, wide temperature window and excellent recyclability. It is reasonable to ignore the UC degradation in this study since the cycle-life of UCs can be millions before noticeable performance deterioration.

The low energy density characteristic of UCs means they need to be threaded to form a UC pack with the purpose of storing more energy and increasing terminal voltage. The UC specification used in the study are listed in Table 7.4, while the main parameters of the UC pack are deduced from

$$\begin{cases} C_{UC} = \frac{n_{up} C_{U_cell}}{n_{us}} \\ R_{UC} = \frac{n_{us} R_{U_cell}}{n_{up}} \\ V_{UC} = n_{us} V_{U_cell} \end{cases} \quad (7.8)$$

where C_{UC} and V_{UC} denote the capacitance and the terminal voltage of the UC pack, n_{us} denotes the number of series connected UC cells, n_{up} denotes the number of parallel connected UC cell stings, R_{U_cell} is the UC cell resistance, C_{U_cell} is the UC cell capacitance and V_{U_cell} is the UC cell voltage.

The terminal power of UC pack is calculated using

$$P_{UC} = n_{up} n_{us} (V_{U_cell}(t) I_{UC}(t) - R_{U_cell} I_{UC}^2(t)) \quad (7.9)$$

where I_{UC} is the cell current.

The linear relationship between the terminal voltage and the SOC of the UC means that the UC pack energy E_{UC} can be derived from

$$\begin{cases} soc_U = \frac{V_{U_cell}}{V_{U_n}} \\ E_{UC} = 0.5n_{up}n_{us}C_{U_cell}V_{U_n}^2SOC_U^2 \end{cases} \quad (7.10)$$

where V_{U_n} means the UC nominal voltage.

The working UC SOC window is from 20% to 90% in order to fully capitalize on the stored energy while avoiding detrimental effects of over-charging/discharging.

Table 7.4 Main specifications of UC.

Parameter (unit)	Value
UC nominal capacitance C_{B_cell} (F)	3000
Cell nominal voltage V_{U_n} (V)	2.7
Cell resistance R_{U_cell} (Ohm)	0.00029
Cell unit cost c_b (USD)	32.5
Cell mass m_u (kg)	0.51
Maximum UC SOC soc_{max} (%)	90
Minimum UC SOC soc_{min} (%)	20

7.4 Wave-transform-based Power Split Strategy

A capable and efficient power split strategy is crucial for fully utilizing the HESS potential and has been the subject of several studies. It is responsible for appropriately distributing the load to the two energy sources with either heuristic rules or optimization-based control algorithms. The wavelet-transform (WT) technique provides a promising solution to this problem. The WT is able to analyse and decompose an original signal into different localized contributions, each of which represents a portion of the signal with a different frequency [127]. The power demand profile of an EV can be viewed as a series of signals, and the reference power signals for the battery and UC packs can be acquired by using the WT as a load sharing algorithm [128]. The high frequency and low frequency components of the load profile can be effectively separated with the high-frequency components designated to the UC pack and the remaining components designated to the battery pack. This approach helps to protect the battery pack from frequent charging/discharging transients, with the advantages of online and easy implementation.

The continuous wavelet transform (CWT) is defined as

$$W(\tau, s) = \int_{-\infty}^{+\infty} x(t) \frac{1}{\sqrt{s}} \psi\left(\frac{t-\tau}{s}\right) dt \quad (7.11)$$

where $W(\tau, s)$ is the coefficients, $x(t)$ is the original signal, Ψ is the mother function, τ ($\tau \in R$, $\tau > 0$) is the position parameter that controls the time window size, s is the scale parameter that determines the frequency band width.

The mother wavelet function plays a vital role in decomposing and localizing the target transients. The *Harr* wavelet has been used with much success because of its short filter length

relative to other wavelets, and is used in this study [129]. It is defined by

$$\Psi(t) = \begin{cases} 1, & t \in [0, 0.5) \\ -1, & t \in [0.5, 1) \\ 0, & \text{otherwise} \end{cases} \quad (7.12)$$

A discrete waveform transform (DWT) is used to decompose the discretised signal into different resolutions based on the scale factor. The DWT and its inverse are given by

$$W(\tau, s) = \int_{-\infty}^{+\infty} x(t) \frac{1}{\sqrt{s}} \psi\left(\frac{t-\tau}{s}\right) dt, \quad (7.13)$$

$$s = 2^j, \tau = k2^j, k \in Z^2$$

$$x(t) = \sum_{j \in Z} \sum_{k \in Z} W(j, k) \psi_{j,k}(t) \quad (7.14)$$

where Z denotes the set of all positive integers.

In this study, the UDDS driving cycle is used to represent the power demand of the EV as shown in Fig. 7.5. The power demands are decomposed into high-frequency and low-frequency components by the *Harr* WT including three-level decomposition and reconstruction process as shown in Fig. 7.6. The high-pass analysis filter and the low-pass analysis filter are $H(z)$ and $L(z)$ in the decomposition process, respectively, while they are represented by $h(z)$ and $l(z)$ in the reconstruction process. After the processing, the power demands assigned to the battery pack and UC pack are derived as shown in Fig. 7.7. It is apparent that the battery pack produces a smooth power delivery along with a reduced maximum power level while the UC pack serves to meet the dynamic power transients. The WT based power split strategy is implementable for online HESS power coordination by incorporating a power demand prediction algorithm.

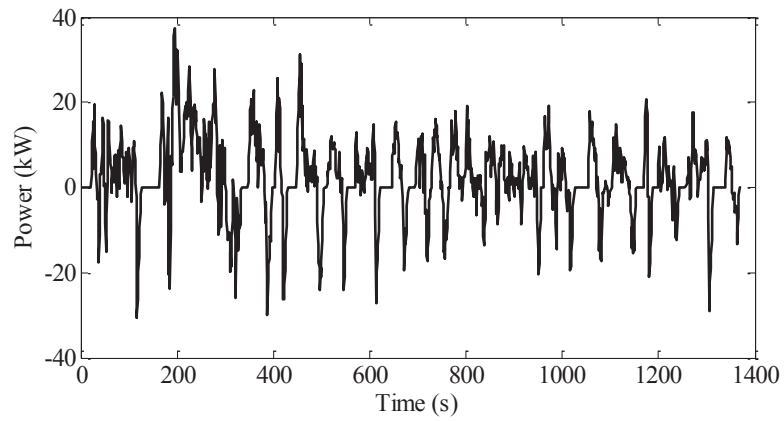


Fig. 7.5 UDDS driving cycle power demand.

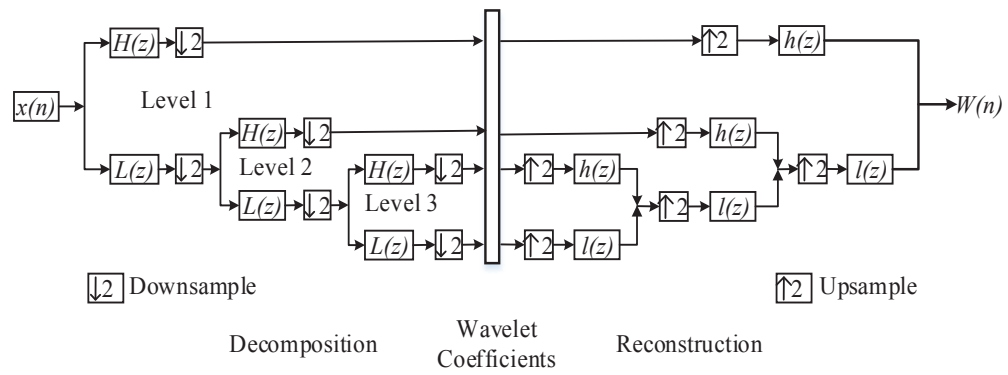


Fig. 7.6 Harr wavelet decomposition and reconstruction.

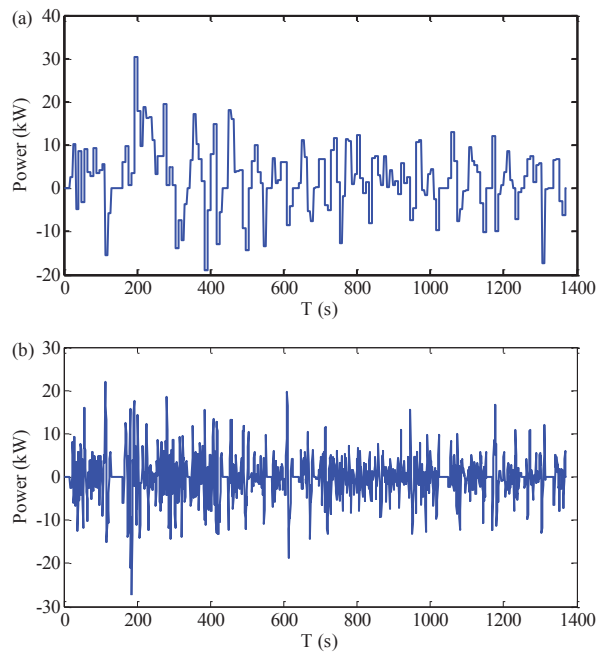
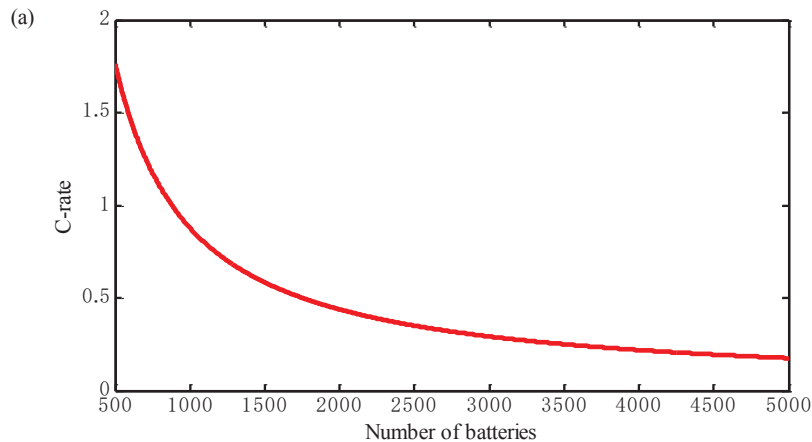


Fig. 7.7 Power demand for (a) battery pack; (b) UC pack.

7.5 Multi-objective Optimal Sizing of HESS

The primary goal of this study is to investigate the optimal sizing of an HESS by taking into account configuration, weight, manufacturing cost and battery degradation. Generally speaking, more UC usage in a system would help reduce battery stress during hard accelerations and recuperate more braking energy, which is conducive to prolonging battery life. Fig. 7.8 shows the evolution of cell discharging C-rate and SOH with respect to the deployed battery number. It is apparent that increased battery number reduces the overall discharging stress (i.e. C-rate) of each cell. But this benefit comes along with increasing cost. In addition, UCs have much smaller specific energy and energy density relative to batteries, so that the mounting weight issue is also a big concern. Thus, it is necessary to strike a trade-off between these conflicting objectives; i.e. prolonging battery life and diminishing the system weight and manufacture cost. This can be set as an optimization problem. The optimization variables are n_{up} , n_{us} , n_{bp} , n_{bs} . The driving performance requirements listed in Table 7.5 are formulated as the optimization constraints, which are detailed in the following Sections.



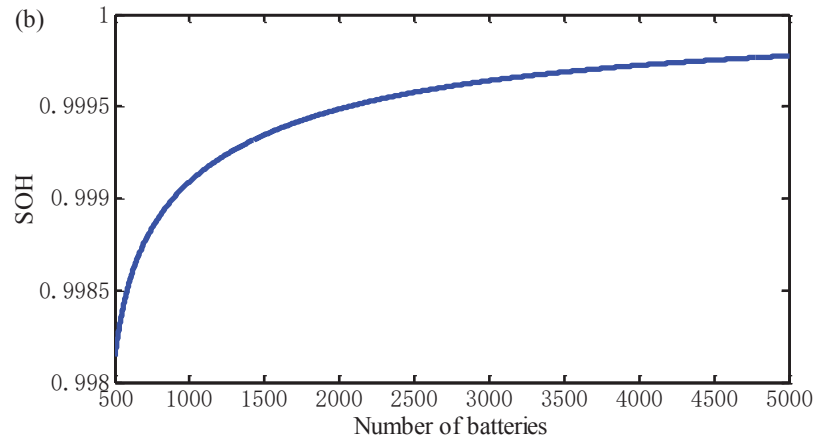


Fig. 7.8 The evolution of (a) discharging C-rate; (b) battery SOH after 100 repeated UDDS cycles; with regard to the battery number.

7.5.1 Maximum speed

According to the vehicle dynamic equation on flat ground, the relationship between the maximum speed and the HESS power demand can be obtained from

$$mgf_{u_{\max}} + 0.5C_D A \rho u_{\max}^3 \leq P_{HESS} \eta_m \eta_T \quad (7.15)$$

where m is the vehicle mass including the HESS, g is gravity, f is the rolling resistance coefficient, u_{max} is the maximum speed, C_D is the air drag coefficient, A is the front area of the vehicle, ρ is the air density, P_{HESS} is the HESS output power, η_m is the efficiency of the electric motor, and η_T is the transmission efficiency.

Table 7.5 Driving performance requirements.

Indicator	Requirements
Acceleration Time T_{acc}	<14.8 s
Mileage (@60Km/h) M_R	150 km
Maximum speed u_{max}	140 km/h

7.5.2 Driving mileage

It is well known that the driving range of an EV depends the driving style, road conditions and power control strategy. For fair comparison, the value is always calculated under the assumption of constant speed u_0 (60 km/h) and a flat road. Under such circumstances, only the battery pack runs as the sole power source since the power demand is quite stable. The driving range can be derived as

$$M_R \leq \frac{E_{BATT} \eta_m \eta_T}{mgf + 0.5C_D A \rho u_0^2} \quad (7.16)$$

where E_{BATT} is the nominal energy of battery pack.

7.5.3 Acceleration time

The acceleration time is usually used to represent the acceleration capability of the vehicle, which is calculated by accelerating the vehicle from stationary to a certain speed u_I ($u_I = 100$ km/h) on a flat road. The acceleration time t_{acc} is

$$\left\{ \begin{array}{l} u(i) = 0 \\ u(i) = u(i-1) + \frac{F_{acc} \Delta t}{\delta m} \\ F_{acc}(i) = \frac{T_{m_max} k \eta_T}{R_{tire}} - mgf - 0.5 C_D A \rho u(i-1)^2 \\ T_{m_max} = \min(T_{m_allowed}, \frac{P_{HESS_acc} \eta_m}{\omega(i)}) \\ t_{acc} \geq n \Delta t \end{array} \right. \quad (7.17)$$

where F_{acc} is the acceleration force, k is the gear ratio of the final drive, T_{m_max} is the maximum output torque of the electric motor determined by the external characteristic curve of the electric motor and power handling capability of the HESS, $T_{m_allowed}$ is the maximum output torque of the electric motor depending on the electric motor external characteristic curve, Δt is the sample time, R_{tire} is the rolling radius of the tire, P_{HESS_acc} is the HESS power demand, ω is the rotational speed of the electric motor, t_{acc} is the acceleration time, and N is the index of the discrete time instant when the target velocity u_1 (100 km/h) is reached.

In order to accommodate the handling ability of DC-DC converter, the allowed battery pack and the UC pack voltages are

$$\left\{ \begin{array}{l} 150 \leq V_{BATT} \leq 600 \\ 50 \leq V_{UC} \leq 300 \\ V_{UC} \leq V_{BATT} \end{array} \right. \quad (7.18)$$

The NSGA-II algorithm is employed to solve the optimization problem. It has the ability to find multiple Pareto-optimal solutions in one single simulation run [130]. It addresses the main issues of the seminal NSAG algorithm. These relate to the high computational complexity, lack of elitism and need for tuning the sharing parameter. The optimal sizing of an HESS can be mathematically expressed as

$$\begin{aligned} & \min(c_b n_{bs} n_{bp} + c_u n_{us} n_{up}, m_b n_{bs} n_{bp} + m_u n_{us} n_{up}, Q_{loss}) \\ & s, t, n_{bs}, n_{bp}, n_{us}, n_{up} \in N^+ \\ & \text{and Eqns. (7.15), (7.16), (7.17) and (7.18)} \end{aligned} \quad (7.19)$$

where c_b and c_u are the unit costs of the batteries and UCs; and m_b and m_u are the unit masses of the batteries and UCs.

After implementation of the optimization algorithm, a feasible solution region is obtained and shown in Fig. 7.9. The UC SOC evolution with $n_{us} = 60$ and $n_{up} = 1$ is illustrated in Fig. 7.10. The UC SOC is effectively constrained between the lower and upper operating limits while working to meet the peak transients. Fig. 7.11 illustrates the battery degradation with HESS and battery-only ESS during the UDDS driving cycle. It can be seen that the HESS can effectively reduce the battery degradation compared with the battery-only ESS, thereby prolonging the battery life. Since there is no dominant solution in the multi-objective optimization problem, the battery wear and HESS weight with respect to the manufacture cost in the feasible domain are shown in Fig. 7.12. It is obvious that the increasing cost can effectively extend battery life but inevitably produces additional weight. With different design emphases (i.e., cost, weight and/or battery degradation), a set of distinct coefficients can be assigned to the optimization objectives, in which a unique solution may be attainable while satisfying all the specifications formulated as constraints.

Since the cost-effectiveness is more sensitive in comparison to the weight and battery degradation when synthesizing HESS design in practice, an optimal sizing is derived by further formulating the weight and battery degradation as constraints. The unique optimal solution regarding to cost is the minimum value on the x -axle that locates between the weigh and battery degradation projection points on the x -axle as shown in Fig. 7.12.

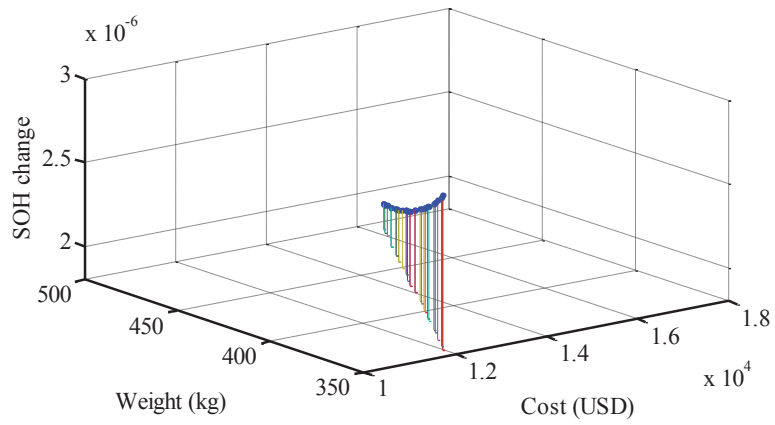


Fig. 7.9 The optimization result for a UDDS driving cycle.

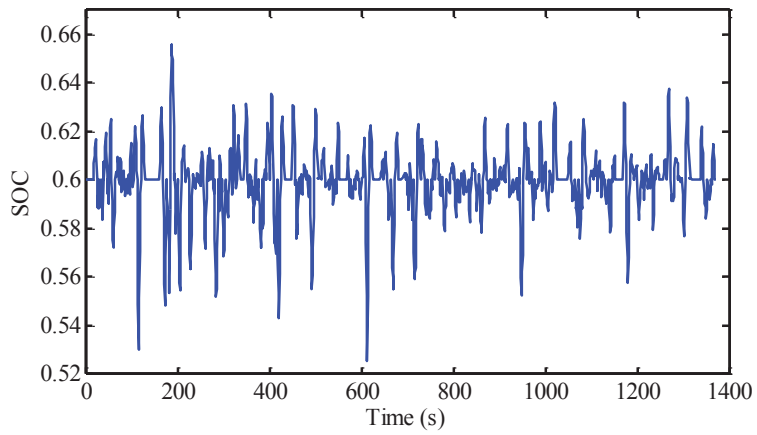


Fig. 7.10 UC SOC evolution during the UDDS driving cycle.

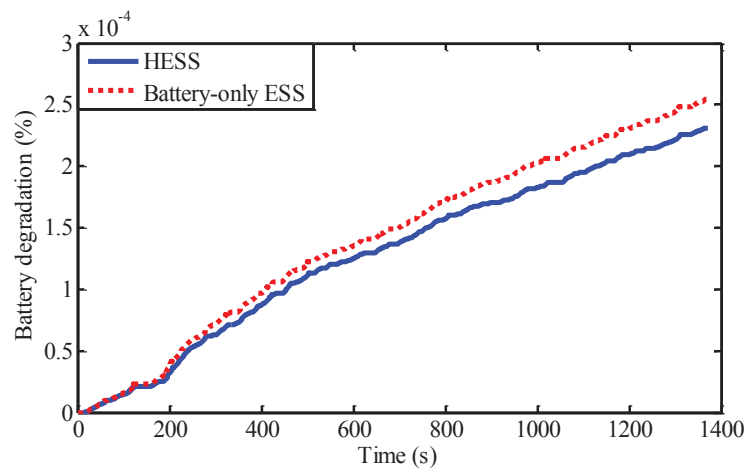


Fig. 7.11 Battery degradation with HESS and battery-only ESS during the UDDS driving cycle.

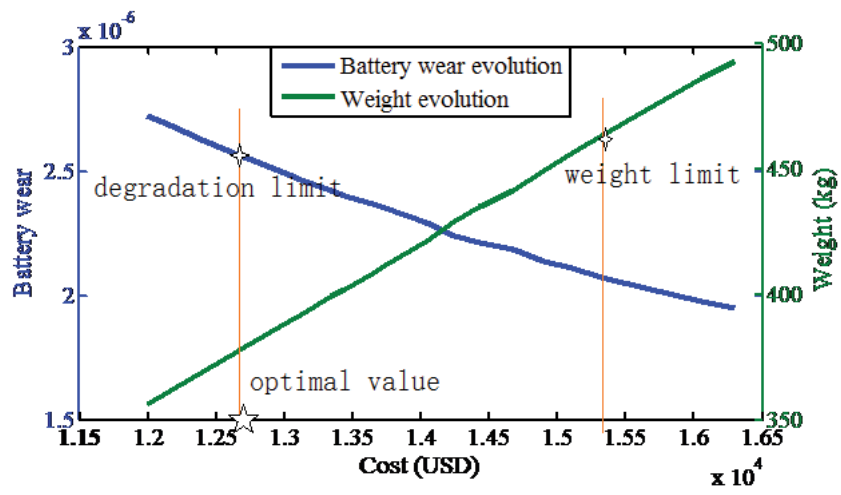


Fig. 7.12 The evolution of battery wear and HESS weight with regard to cost.

7.6 Summary

In this chapter, the optimal sizing of an HESS composed of batteries and UCs, for an example electric vehicle, has been studied and formulated as a multi-objective problem. The battery SOH, HESS weight and cost are selected as the optimization objectives. In particular, a battery SOH model was incorporated in order to investigate the impact of component sizing on the battery life in a quantitative fashion. The driving performance requirements and the operational boundaries for both the batteries and UCs were used as the optimization constraints. The wavelet-transform-based power management algorithm was adopted to realize the power split between the batteries and UCs. The NSGA-II algorithm was then utilized in order to search for the feasible solution domain that satisfies the optimization constraints. The results provide prudent insights into HESS sizing with different emphases.

8 Conclusions and Future Work

8.1 Conclusions

In this thesis, UC modelling and SOC estimation for in EV applications have been studied.

Firstly, a special test rig for UC characteristic investigation was designed and developed. A series of UC tests were conducted using this rig in accordance to a specifically composed test procedure, resulting in a wide-ranging UC database. This database is the foundation for later modelling and SOC estimation studies. Based on the EIS test data, the UC impedance characteristic dependency on temperature and SOC was investigated. In particular, their coupling effect was illustrated, and the high-efficiency SOC window was highlighted.

Secondly, a systematic examination of three commonly used equivalent circuit models for UCs was conducted. This addressed model accuracy, complexity and robustness in the context of EV applications. The results showed that the dynamic model has the best overall performance. In order to realize online model characterization, an EKF scheme was proposed to recursively estimate the model parameters. The effectiveness and robustness of the proposed method was validated using driving-cycle-based datasets.

Thirdly, a robust H -infinity observer was presented to realize the real-time SOC estimation. In comparison to the state-of-the-art Kalman filter-based methods (KF), the developed robust scheme can ensure high estimation accuracy even without prior knowledge of the process and measurement noise statistical properties. Moreover, it exhibits more robustness to modelling uncertainties.

For further improving modelling accuracy, a new fractional-order model was proposed to emulate the UC dynamics. The novel fractional-order model consists of a series resistor, a

CPE, and a Warburg-like element. By means of this fractional-order model, a fractional KF was formulated to estimate the UC SOC. Validation results show that the proposed fractional-order modelling and state estimation scheme are accurate, and outperform their integer counterparts.

Finally, an optimal HESS sizing method is put forward. This uses a multi-objective optimization algorithm, with the overarching goal of reducing ESS cost and weight while prolonging battery life. To this end, a battery state-of-health (SOH) model was incorporated to quantitatively investigate the impact of component sizing on battery life. The wavelet-transform-based power management algorithm was adopted in order to realize the power coordination between the batteries and UCs. The results provide prudent insights into HESS sizing with different emphases.

8.2 Future Work

This thesis is dedicated to addressing the modelling and SOC estimation for UCs in the context of EV applications. The optimal model structure has been identified through a systematically comparative study of the existing equivalent circuit models. However, these models invariably neglect the impact of temperature on the model parameters, and fail to explicitly account for the coupling effect of thermal and electrical behaviour, which may compromise the modelling validity when the systems are exposed to wild thermal variations. In order to further improve the modelling accuracy under varying thermal conditions, it is meaningful to develop an enabling but efficient thermo-electrical model for UCs to simultaneously predict the electrical and thermal behaviour of a cell under driving-cycle-based operating conditions. The coupling of electrical and thermal models allows for tuning

of temperature-dependent parameters to better account for the thermal impacts on the electrical behaviour.

With regards to HESS, this study mainly focuses the optimal sizing problem while the energy management strategy formulation is reasonably simplified with the purpose of improving the computational efficiency of the optimization algorithm. In order to fully realize the potential of HESSs, the energy management strategy plays essential roles, and its development deserve more efforts from detailed system modelling to advanced control synthesis, etc. This will be the focus of my future work.

References

- [1] Annual Energy Review 2010. Washington DC: US Energy Information Administration, October, 2011:
<http://www.eia.gov/totalenergy/data/annual/pdf/aer.pdf>.
- [2] Davis, Stacy C., Susan W. Diegel, and Robert G. Boundy. Transportation Energy Data Book: Edition 30. Washington, DC: US Department of Transportation, June, 2011.
- [3] National emissions inventory (NEI) air pollutant emissions trends data. Washington, DC: Environmental Protection Agency, 2011:
<http://www.epa.gov/ttn/chief/trends/trends06/nationaltierlupto2008basedon2005v2.xls>.
- [4] <http://www.eea.europa.eu/data-and-maps/figures/global-co2-emissions-186020132006>.
- [5] S. Chu and A. Majumdar, “Opportunities and challenges for a sustainable energy future,” *Nature*, vol. 488, no. 7411, pp. 294-303, Aug. 2012.
- [6] Siang Fui Tie, and Chee Wei Tang, “A review of energy sources and energy management system in electric vehicles,” *Renew. Sust. Energ. Rev.*, vol. 20, pp. 82-102, 2013.
- [7] N. A. Chaturvedi, R. Klein, J. Christensen, J. Ahmed, and A. Kojic, “Algorithms for Advanced Battery-Management Systems,” *IEEE Control Syst. Mag.*, vol. 30, no.3, pp. 49-58, 2010.
- [8] M. Armand, and J.M. Tarascon, “Building better batteries,” *Nature*, vol.451, pp. 652-657, 2008.

- [9] J. Cao, N. Schofield, and A. Emadi, "Battery balancing methods: A comprehensive review," in: *Proc. IEEE Veh. Power Propulsion Conf.*, pp. 1-6, 2008.
- [10] S. T. Huang, D. C. Hopkins, and C. R. Mosling, "Extension of battery life via charge equalization control," *IEEE Trans. Ind. Electron.*, vol. 40, no. 1, pp. 96-104, Feb. 1993.
- [11] Erdinc O, Vural B, Uzunoglu M. A wavelet-fuzzy logic based energy management strategy for a fuel cell/battery/ultra-capacitor hybrid vehicular power system. *J. Power Sources*, vol. 194, pp. 369-380, 2009.
- [12] Conway BE. Electrochemical supercapacitors: scientific fundamentals and technological applications. New York: *Kluwer Academic/Plenum Publishers*, 1999.
- [13] Y. Diab, P. Venet, H. Gualous, and G. Rojat. "Self-discharge characterization and modelling of electrochemical capacitor used for power electronics applications," *IEEE Trans. Power Electron.*, vol. 24, no.2, pp. 510-517, Feb. 2009.
- [14] G. Wang, L. Zhang, and J. Zhang. "A review of electrode materials for electrochemical supercapacitors," *Chem. Soc. Rev.*, vol. 41, no. 2, pp. 797-828, Jan. 2012.
- [15] L. Gao, R. A. Dougal and S. Liu, "Power Enhancement of an Actively Controlled Battery/Ultracapacitor Hybrid," *IEEE Trans. Power Electron.*, vol. 20, no.1, pp. 236-243, Jan. 2005.
- [16] P. Bentley, D. A. Stone and N. Schofield, "The parallel combination of a VRLA cell and supercapacitor for use as a hybrid vehicle peak power buffer," *J. Power Source*, vol.147, pp.288-294, 2005.
- [17] M. Ortúzar, J. Moreno, and J. Dixon, "Ultracapacitor-Based Auxiliary Energy System for an Electric Vehicle: Implementation and Evaluation," *IEEE Trans. Power Electron.*, vol. 54, no.4, pp. 2147-2156, Aug. 2007.

- [18] J. Cao, and A. Emadi, "A New Battery/UltraCapacitor Hybrid Energy Storage System for Electric, Hybrid, and Plug-In Hybrid Electric Vehicles," *IEEE Trans. Power Electron.*, vol. 27, no.1, pp. 122-132, Jan. 2012.
- [19] A. Kuperman, I. Aharon, S. Malki and A. Kara, "Design of a Semiactive Battery-Ultracapacitor," *IEEE Trans, Power Electron.*, vol. 28, no.2, pp. 806-815, Feb. 2013.
- [20] N. Omar etc., "Lithium iron phosphate based battery – Assessment of the aging parameters and development of cycle life model," *Appl. Energy*, vol. 113, pp. 1575-1585, Jan. 2014.
- [21] von Helmholtz, "H. Studien €uber elektrische grenzschichten," *Ann. Phys.*, vol. 243, pp. 337-382, 1879.
- [22] H. Wang, L. Pilon, "Accurate simulations of electric double layer capacitance of ultramicroelectrodes," *J. Phys. Chem. C*, vol. 115, no. 33, pp. 16711-16719, Jul. 2011.
- [23] G. Gouy, "Constitution of the electric charge at the surface of an electrolyte," *J. Phys. Theor. Appl.*, vol. 9, no. 4, pp. 457-467, 1910.
- [24] D. L. Chapman, "A contribution to the theory of electrocapillarity," *Philos. Mag. Ser. 6*, vol. 25, no. 148, pp. 475-481, Jun. 1913.
- [25] O. Stern, "The theory of the electrolytic double shift," *Z. Elektrochem, Angew. Phys. Chem.*, vol. 30, pp. 508-516, 1924.
- [26] A. Bard, L. Faulkner, *Electrochemical Methods: Fundamentals and Applications*, New York: *John Wiley & Sons*, 2001.
- [27] V. Bagotsky, *Fundamentals of Electrochemistry*, 2nd ed., New York: *John Wiley & Sons*, 2006.
- [28] J. J. Bikerman, "Structure and capacity of electrical double layer," *Philos. Mag.*, vol.

- 33, no. 220, pp. 384-397, Mar. 1942.
- [29] M. Verbrugge, P. Liu, "Microstructural analysis and mathematical modeling of electric double-layer supercapacitors," *J. Electrochem. Soc.*, vol. 152, no. 5, pp. 79-87, 2005.
- [30] S. Allu, B. Velamuri Asokan, W. A. Shelton, B. Philip, S. Pannala, "A generalized multi-dimensional mathematical model for charging and discharging processes in a supercapacitors," *J. Power Sources*, vol. 256, pp. 369-382, Jun. 2014.
- [31] H. Wang, L. Pilon, "Mesoscale modeling of electric double layer capacitors with three-dimensional ordered structures," *J. Power Sources*, vol. 221, pp. 252-260, Jan. 2013.
- [32] S. Kim, W. Choi, K. Lee, S. Choi, "Advanced dynamic simulation of supercapacitors considering parameter variation and self-discharge," *IEEE Trans. Power. Electron.*, vol. 26, no. 11, Nov. 2011.
- [33] R. L. Spyker, and R. M. Nelms, "Classical equivalent circuit parameters for a double-layer capacitor," *IEEE Trans. Aerosp. Electron. Syst.*, vol. 36, pp. 829-836, 2000.
- [34] L. Zubietta, R. Boner, "Characterization of double-layer capacitors for power electronics applications," *IEEE Trans. Ind. Appl.*, vol. 36, no. 1, pp.199-205, Jan./Feb. 2000.
- [35] R. Faranda, "A new parameters identification procedure for simplified double layer capacitor two-branch model," *Electr. Power Syst. Res.*, vol. 80, no. 4, pp. 363-371, Apr. 2010.
- [36] R. Chai, Y. Zhang, "A practical supercapacitor model for power management in wireless sensor nodes," *IEEE Trans. Power Electron.*, vol. 30, no. 12, pp. 6720-6730, Dec. 2015.
- [37] A. Weddell, G. Merrett, T. Kazmierski, B. Al-Hashimi, "Accurate supercapacitor modeling for energy harvesting wireless sensor nodes," *IEEE Trans. Circuits Syst. II*,

- Exp. Briefs*, vol. 58, no. 12, pp. 911-915, Dec. 2011.
- [38] P. O. Logerais, M. A. Camara, O. Riou, A. Djellad, A. Omeiri, "Modeling of a supercapacitor with a multibranch circuit," *Int. J. Hydrogen Energ.*, vol. 40, no. 39, pp. 13725-13736, Oct. 2015.
- [39] K. Liu, C. Zhu, R. Lu, C. Chan, "Improved study of temperature dependence equivalent circuit model for supercapacitors," *IEEE Trans. Plasma Sci.*, vol. 41, no. 5, pp. 1267-1271, May 2013.
- [40] Y. Zhang, H. Yang, "Modeling and characterization of supercapacitors for wireless sensor network applications," *J. Power Sources*, vol. 196, no. 8, pp. 4128-4135, Apr. 2011.
- [41] S. Buller, E. Karden, D. Kok, R. Doncker, "Modeling the dynamic behavior of supercapacitors using impedance spectroscopy," *IEEE Trans. Ind. Appl.*, vol. 38, no. 6, pp. 1622-1626, Nov./Dec. 2002.
- [42] V. Musolino, L. Piegari, E. Tironi, "New full-frequency-range supercapacitor model with easy identification procedure," *IEEE Trans. Ind. Electron.*, vol. 60, no. 1, pp. 112-120, Jan. 2013.
- [43] H. Gualous, D. Bouquain, A. Berthon, J. M. Kauffmann, "Experimental study of supercapacitor serial resistance and capacitance variations with temperature," *J. Power Sources*, vol. 123, no. 1, pp. 86-93, Sep. 2003.
- [44] F. Rafika, H. Gualous, R. Gallay, A. Crausaz, A. Berthon, "Frequency, thermal and voltage supercapacitor characterization and modeling," *J. Power Sources*, vol. 165, no. 2, pp. 928-934, Mar. 2007.
- [45] F. Belhachemi, S. Raël, B. Davat, "A physical based model of power electric double-

- layer supercapacitors,” in Conf. Rec. the 2000 IEEE Ind. Appl., vol. 5, pp. 3069-3076, Oct. 2000.
- [46] D. Torregrossa, M. Bahramipناه, E. Namor, R. Cherkaoui, M. Paolone, “Improvement of dynamic modeling of supercapacitor by residual charge effect estimation,” *IEEE Trans. Ind. Electron.*, vol. 61, no. 3, 1345-1354, Mar. 2014.
- [47] N. Rizoug, P. Bartholomeüs, P. Moigne, “Modeling and characterizing supercapacitors using an online method,” *IEEE Trans. Ind. Electron.*, vol. 57, no. 12, 3980-3990, Dec. 2010.
- [48] R. A. Dougal, L. Gao, S. Liu, “Ultracapacitor model with automatic order selection and capacity scaling for dynamic system simulation,” *J. Power Sources*, vol. 126, no. 1-2, pp. 250-257, Feb. 2004.
- [49] W. Shen, “State of available capacity estimation for lead-acid batteries in electric vehicles using neural network,” *Energ. Convers. Manage.*, vol. 48, no. 2, pp. 433-442, Feb. 2007.
- [50] A. Soualhi, A. Sari, H. Razik, P. Venet, G. Clerc, R. German, O. Briat, J. M. Vinassa, “Supercapacitors ageing prediction by neural networks,” in: *Proc. 39th IEEE Ind. Electron. Soc. Annu. Conf.*, pp. 6812-6818.
- [51] H. Farsi, F. Gobal, “Artificial neural network simulator for supercapacitors performance prediction,” *Com. Mater. Sci.*, vol. 39, no. 3, pp. 678-683, May 2007.
- [52] C. Wu, Y. Hung, C. Hong, “On-line supercapacitor dynamic models for energy conversion and management,” *Energ. Conv. Manage.*, vol. 53, no. 1, pp. 337-345, Jan. 2012.
- [53] A. Eddahech, O. Briat, M. Ayadi, J-M. Vinassa, “Modeling and adaptive control for

- supercapacitor in automotive applications based on artificial neural networks,” *Electr. Power Syst. Res.*, vol. 106, pp. 134-141, Jan. 2014.
- [54] T. Weigert, Q. Tian, K. Lian, “State-of-charge prediction of batteries and battery–supercapacitor hybrids using artificial neural networks,” *J. Power Sources*, vol. 196, no. 8, pp. 4061-4066, Apr. 2011.
- [55] J. Marie-Francoise, H. Gualous, A. Berthon, “Supercapacitor thermal- and electrical-behaviour modelling using ANN,” *IEE Proc. Electr. Power Appl.*, vol. 153, no. 2, pp. 255-262, Mar. 2006.
- [56] B. Wang, S. Li, H. Peng, Z. Liu, “Fractional-order modeling and parameter identification for lithium-ion batteries,” *J. Power Sources*, vol. 293, pp. 151-161, Oct. 2015.
- [57] J. Xu, C. C. Mi, B. Cao, J. Cao, “A new method to estimate the state of charge of lithium-ion batteries based on the battery impedance model,” *J. Power Sources*, vol. 233, pp. 277-284, Jul. 2013.
- [58] D. Riu, N. Retière, D. Linzen, “Half-order modelling of supercapacitors,” in *Conf. Rec. the 2004 IEEE Ind. Appl.*, vol. 4, pp. 2550-2554, Oct. 2004.
- [59] V. Martynyuk, M. Ortigueira, “Fractional model of an electrochemical capacitor,” *Signal Process.*, vol. 107, pp. 355-360, Feb. 2015.
- [60] N. Bertrand, J. Sabatier, O. Briat, J. M. Vinassa, “Fractional non-linear modelling of ultracapacitors,” *Commun. Nonlinear Sci. Numer. Simulat.*, vol. 15, no. 5, pp. 1327-1337, May 2010.
- [61] R. Martín, J. J. Quintana, A. Ramos, I. Nuez, “Modeling of electrochemical double layer capacitors by means of fractional impedance,” *J. Comp. Nonlinear Dyn.*, vol. 3,

pp. 021303, 2008.

- [62] A. Dzieliński, G. Sarwas, D. Sierociuk, “Time domain validation of ultracapacitor fractional order model,” in: *Proc. the 49th IEEE Conf. Decis. Contr.*, pp. 3730-3735, 2010.
- [63] T. J. Freeborn, B. Maundy, A. S. Elwakil, “Measurement of supercapacitor fractional-order model parameters from voltage-excited step response,” *IEEE J. Em. Sel. Topic Circuits Syst.*, vol. 3, no. 3, pp. 367-376, Jul. 2013.
- [64] J. -D. Gabano, T. Poinot, H. Kanoun, “LPV continuous fractional modeling applied to ultracapacitor impedance identification,” *Contr. Eng. Proct.*, vol. 45, pp. 86-97, Dec. 2015.
- [65] M. Catelani, L. Ciani, M. Marracci, B. Tellini, “Analysis of ultracapacitors ageing in automotive application,” *Microelectron. Reliab.*, vol. 53, no. 9-11, pp. 1676-1680, Sep.-Nov. 2013.
- [66] L. Zhang, Z. Wang, X. Hu, D. G. Dorrell, “Residual capacity estimation for ultracapacitors in electric vehicles using artificial neural network,” *Proceedings of IFAC World Congress*, vol. 19, pp. 3899-3904, 2014.
- [67] A. Nadeau, M. Hassanaliheragh, G. Sharma, T. Soyata, “Energy awareness for supercapacitors using Kalman filter state-of-charge tracking,” *J. Power Sources*, vol. 296, pp. 383-391, Nov. 2015.
- [68] C. Chiang, J. Yang, W. Cheng, “Temperature and state-of-charge estimation in ultracapacitors based on extended Kalman filter,” *J. Power Sources*, vol. 234, pp. 234-243, Jul. 2013.
- [69] H. Yang, Y. Zhang, “Estimation of supercapacitor energy using a linear capacitance for

- applications in wireless sensor networks,” *J. Power Sources*, vol. 275, pp. 498-505, Feb. 2015.
- [70] S. Dey, S. Mohon, P. Pisu, B. Ayalew, and S. Onori, “Online state and parameter estimation of battery-double layer capacitor hybrid energy storage system,” *Proceedings of the 54th IEEE Annual Conference on Decision and Control*, pp. 676-681, 2015.
- [71] A. Burke, “Ultracapacitors: why, how, and where is the technology,” *J. Power Sources*, vol. 91, no.1, pp. 37-50, Nov. 2000.
- [72] D. Torregrossa, M. Bahramipناه, E. Namor, R. Cherkaoui, M. Paolone, “Improvement of dynamic modeling of supercapacitor by residual charge effect estimation,” *IEEE Trans. Ind. Electron.*, vol. 61, no. 3, pp. 1345-1354, Mar. 2014.
- [73] Y. Parvini, J. Siegel, A. G. Stefanopoulou, A. Vahidi, “Supercapacitor electrical and thermal modeling, identification, and validation for a wide range of temperature and power applications,” *IEEE Trans. Ind. Electron.*, vol. 63, no. 32, pp. 1574-1585, Mar. 2016.
- [74] S.-M. Kim and S.-K. Sul, “Control of rubber tyred gantry crane with energy storage based on supercapacitor bank,” *IEEE Trans. Power Electron.*, vol. 21, no. 5, pp. 1420-1427, Sep. 2006.
- [75] V. Sedlakova, J. Sikula, J. Majzner, P. Sedlak, T. Kuparowitz, B. Buergler, P. Vasina, “Supercapacitor equivalent electrical circuit model based on charges redistribution by diffusion,” *J. Power Sources*, vol. 286, pp. 58-65, Jul. 2015.
- [76] W. Waag, S. Käbitz, D. U. Sauer, “Experimental investigation of the lithium-ion battery impedance characteristic at various conditions and aging states and its influence on the

- application,” *Appl. Energ.*, vol. 102, pp. 885-897, Feb. 2013.
- [77] D. Andre, M. Meiler, K. Steiner, Ch. Wimmer, T. Soczka-Guth, D. U. Sauer, “Characterization of high-power lithium-ion batteries by electrochemical impedance spectroscopy. I. Experimental investigation,” *J. Power Sources*, vol. 196, no. 12, pp. 5334-5341, Jun. 2011.
- [78] S. Rodrigues, N. Munichandraiah, A. Shukla, “AC impedance and state-of-charge analysis of a sealed lithium-ion rechargeable battery,” *J. Solid State Electrochem.*, vol. 3, no. 7, pp. 397-405, Jan. 1999.
- [79] E. Barsukov and J. Macdonald, *Impedance spectroscopy: theory, experiment, and applications. 2nd ed. Wiley-Inter science; 2005.*
- [80] A. Oukaour, M. Pouliquen, B. Tala-Ighil, H. Gualous, E. Pigeon, O. Gehan, and B. Boudart, “Supercapacitors aging diagnosis using least square algorithm,” *Microelectron. Reliab.*, vol. 53, no. 9-11, pp. 1638-1642, Sep.-Nov. 2013.
- [81] H. Michel, “Temperature and dynamics problems of ultracapacitors in stationary and mobile applications,” *J. Power Sources*, vol. 154, no. 2, pp. 556-560, Mar. 2006.
- [82] <http://zahner.de/products/electrochemistry/zennium.html>.
- [83] FreedomCar Ultracapacitor Test Manual. Available on-line at:
http://avt.inel.gov/battery/pdf/FreedomCAR_Capacitor_Test_Manual_Sept_2004.pdf.
- [84] M. F. Mathias, O. Haas, “Effect of counterion type on charge transport at redox polymer-modified electrodes,” *J. Phys. Chem.*, vol. 97, no. 3, pp. 9217-9225, 1993.
- [85] O. Bohlen, J. Kowal, D. U. Sauer, “Ageing behaviour of electrochemical double layer capacitors: Part II. Lifetime simulation model for dynamic applications,” *J. Power Sources*, vol. 173, no. 1, pp. 626-632, Nov. 2007.

- [86] R. R. Richardson, P. T. Ireland, D. A. Howey, "Battery internal temperature estimation by combined impedance and surface temperature measurement," *J. Power Sources*, vol. 265, pp. 254-261, Nov. 2014.
- [87] P. Rodatz, G. Paganelli, A. Sciarretta, L. Guzzella, "Optimal power management of an experimental fuel cell/supercapacitor-powered hybrid vehicle," *Control Eng. Pract.*, vol. 13, no. 1, pp. 41-53, Jan. 2005.
- [88] N. Bertrand, J. Sabatier, O. Briat, J. Vinassa, "Embedded fractional nonlinear supercapacitor model and its parametric estimation method," *IEEE Trans. Ind. Electron.*, vol. 57, no. 12, pp. 3991-4000, Dec. 2010.
- [89] F. Sun, X. Hu, Y. Zou, S. Li, "Adaptive unscented Kalman filtering for state of charge estimation of a lithium-ion battery for electric vehicles," *Energ.*, vol. 36, no. 5, pp. 3531-3540, May 2011.
- [90] A. Eddahech, M. Ayadi, O. Briat, J.-M. Vinassa, "Online parameter identification for real-time supercapacitor performance estimation in automotive applications," *Int. J. Electr. Power Energ. Syst.*, vol. 51, pp. 162-167, Oct. 2013.
- [91] X. Hu, F. Sun, X. Cheng, "Recursive calibration for a lithium iron phosphate battery for electric vehicles using extended Kalman filtering," *J. Zhejiang Univ. Sci. A*, vol. 12, pp. 818-825, Nov. 2011.
- [92] N. Devillers, S. Jemei, M.-C. Péra, D. Bienaimé, F. Gustin, "Review of characterization methods for supercapacitor modelling," *J. Power Sources*, vol. 246, pp. 596-608, Jan. 2014.
- [93] E. Cantú, *Efficient and Accurate Parallel Genetic Algorithms: Kluwer Academic Publishers*, Norwell, MA, 2000.

- [94] R. Kötz, M. Hahn, R. Gallay, “Temperature behavior and impedance fundamentals of supercapacitors,” *J. Power Sources*, vol. 154, no. 2, pp. 550-555, Mar. 2006.
- [95] G. Plett, “Extended Kalman filtering for battery management systems of LiPB-based HEV battery packs: Part 1. Background,” *J. Power Sources*, vol. 134, no. 2, pp. 252-261, Aug. 2004.
- [96] J. G. VanAntwerp, R. Braatz, “A tutorial on linear and bilinear matrix inequalities,” *J. Process Contr.*, vol. 10, pp. 363-385, 2000.
- [97] YALMIP official website: <http://users.isy.liu.se/johanl/yalmip/>
- [98] W. Yu, Y. Luo, Y. G. Pi, “Fractional order modeling and control for permanent magnet synchronous motor velocity servo system,” *Mechatronics*, vol. 23, no.7, pp. 813-820, Oct. 2013.
- [99] C.B. Ma, Y. Hori, “Fractional-order control: Theory and applications in motion control,” *IEEE Ind. Electron. Mag.*, vol. 1, no. 4, pp. 6-16, Dec. 2007.
- [100] D. Baleanu, K. Diethelm, E. Scalas, J.-J. Trujillo, Fractional Calculus: Models and Numerical Methods, *World Scientific*, 2010.
- [101] A. Ehsani, M. G. Mahjani, M. Jafarian, “Electrochemical impedance spectroscopy study on intercalation and anomalous diffusion of AlCl₄ ions into graphite in basic molten salt,” *Turk J Chem.*, vol. 35, no.5, pp. 735-743, Oct. 2011.
- [102] C. Li, F. Zeng, Numerical methods for fractional calculus, Taylor & Francis, 2015.
- [103] I. Podlubny, Fractional Differential Equations: an Introduction to Fractional Derivatives, Fractional Differential Equations, to Methods of Their Solution and Some of Their Applications, *Academic Press*, 1998.
- [104] A. Khaligh, Z. Li, “Battery, ultracapacitor, fuel cell, and hybrid energy storage systems

- for electric, hybrid electric, fuel cell, and plug-in hybrid electric vehicles: state of the art,” *IEEE Trans. Veh. Technol.*, vol. 59, no. 6, Jul. 2010.
- [105] Y. Zou, S. E. Li, B. Shao, and B. Wang, “State-space model with non-integer order derivatives for lithium-ion battery,” *Appl. Energy*, vol. 161, pp. 330-336, Jan. 2016.
- [106] M. Jafari, A. Gauchia, K. Zhang, and L. Gauchia, “Simulation and analysis of the effect of real-world driving styles in an EV battery performance and ageing,” *IEEE Trans. Transport. Electrific.*, 2015.
- [107] X. Hu, L. Johannesson, N. Murgovski, and B. Egardt, “Longevity-conscious dimensioning and power management of the hybrid energy storage system in a fuel cell hybrid electric bus,” *Appl. Energy*, vol. 137, pp. 913-924, Jan. 2015.
- [108] J. Shen, S. Dusmez, and A. Khaligh, “Optimization of sizing and battery cycle life in battery/UC hybrid energy storage system for electric vehicle applications,” *IEEE Trans. Ind. Informat.*, vol. 10, no. 4, pp. 2112-2121, Nov. 2014.
- [109] E. Schaltz, A. Khaligh, and P. O. Rasmussen, “Influence of battery/ultracapacitor energy-storage sizing on battery lifetime in a fuel cell hybrid electric vehicle,” *IEEE Trans. Veh. Technol.*, vol. 58, no. 8, Oct. 2009.
- [110] A. Ostadi and M. Kazerani, “A comparative analysis of optimal sizing of battery-only, ultracapacitor-only, and battery–ultracapacitor hybrid energy storage systems for a city bus,” *IEEE Trans. Veh. Technol.*, vol. 64, no. 10, Oct. 2015.
- [111] J. Shen and A. Khaligh, “A supervisory energy management control strategy in a battery/ultracapacitor hybrid energy storage system,” *IEEE Trans. Transport. Electrific.*, vol. 1, no. 3, pp. 223-231, Oct. 2015.
- [112] A. Dougal, S. Liu, and R. E. White, “Power and life extension of battery-ultracapacitor

- hybrids,” *IEEE Trans. Compon. Packag. Technol.*, vol. 25, no. 1, pp. 120-131, Mar. 2002.
- [113] Z. Song, H. Hofmann, J. Li, J. Hou, X. Han, and M. Ouyang, “Energy management strategies comparison for electric vehicles with hybrid energy storage system,” *Appl. Energy*, vol. 134, pp. 321-331, Dec. 2014.
- [114] C. Pan, L. Chen, L. Chen, Chuang, and M. Xie, “Research on energy management of dual energy storage system based on the simulation of urban driving schedules,” *Electr. Power Energy Syst.*, vol. 44, no. 1, pp. 37-42, Jan. 2013.
- [115] J. P. Trovão and C. H. Antunes, “A comparative analysis of meta-heuristic methods for power management of a dual energy storage system for electric vehicles,” *Energy Conv. Manage.*, vol. 95, pp. 281-296, May 2015.
- [116] A. Santucci, A. Sorniotti, and C. Lekakou, “Power split strategies for hybrid energy storage systems for vehicular applications,” *J. Power Sources*, vol. 258, pp. 395-407, 2014.
- [117] M. Choi, J. Lee, and S. Seo, “Real-time optimization for power management systems of a battery/supercapacitor hybrid energy storage system in electric vehicles,” *IEEE Trans. Veh. Technol.*, vol. 63, no. 8, pp. 3600-3611, Oct. 2014.
- [118] M-J. Kim and H. Peng, “Power management and design optimization of fuel cell/battery hybrid vehicles,” *J. Power Sources*, vol. 165, no. 2, pp. 819-832, Mar. 2007.
- [119] Y-H, Hung and C-H Wu, “An integrated optimization approach for a hybrid energy system in electric vehicles,” *Appl. Energy*, vol. 98, pp. 479-490, Oct. 2012.
- [120] X. Zhang, C. C. Mi, A. Masrur, and D. Daniszewsk, “Wavelet-transform-based power management of hybrid vehicles with multiple on-board energy sources including fuel

- cell, battery and ultracapacitor,” *J. Power Sources*, vol. 185, no. 2, pp. 1533-1543, Dec. 2008.
- [121] P. Ramadass, B. Haran, P. M. Gomadam, R. White, and B. N. Popov, “Development of first principles capacity fade model for Li-ion cells,” *J. Electrochem. Soc.*, vol. 151, no. 2, pp. 196-203, 2004.
- [122] R. Spotnitz, “Simulation of capacity fade in lithium-ion batteries,” *J. Power Sources*, vol. 113, no. 1, pp. 72-80, Jan. 2003.
- [123] Fuller TF, Doyle M, Newman J. “Simulation and optimization of the dual lithium ion insertion cell,” *J. Electrochem. Soc.*, vol. 141, no.1, pp.1-10, Jan. 1994.
- [124] J. Wang, P. Liu, J. Hicks-Garner, E. Sherman, S. Soukiazian, M. Verbrugge, H. Tataria, J. Musser, P. Finamore, “Cycle-life model for graphite-LiFePO₄ cells,” *J. Power Sources*, vol. 196, no. 8, pp. 3942-3948, Apr. 2011.
- [125] Z. Song, H. Hofmann, J. Li, X. Han, X. Zhang, M. Ouyang, “A comparison study of different semi-active hybrid energy storage system topologies for electric vehicles,” *J. Power Sources*, vol. 274, pp. 400-411, Jan. 2015.
- [126] D. G. Dorrell, M.-F. Hsieh, A. M. Knight, “Alternative rotor designs for high performance brushless permanent magnet machines for Hybrid Electric Vehicles,” *IEEE Trans. on Magn.*, vol. 48, no. 2, pp. 835-838, Feb. 2012.
- [127] S. M. Ahmmedaand, M. A Zahhad, “A new hybrid algorithm for ECG signal compression based on the wavelet transformation of the linearly predicted error,” *Med. Eng. Phys.*, vol. 23, no. 2, pp. 117-216, Apr. 2001.
- [128] O. Erdinc, B. Vural, M. Uzunoglu, Y. Ates, “Modeling and analysis of an FC/UC hybrid vehicular power system using a wavelet-fuzzy logic based load sharing and control

- algorithm,” *Int. J. Hydrogen Energ.*, vol. 34, no. 12, pp. 5223-5233, Jun. 2009.
- [129] C. Capilla, “Application of the Haar wavelet transform to detect micro-seismic signal arrivals,” *J. Appl. Geophys.*, vol. 59, no. 1, pp. 36-46, May 2006.
- [130] K. Deb, A. Pratap, S. Agarwal, T. Meyarivan, “A fast and elitist multiobjective genetic algorithm: NSGA-II,” *IEEE Trans. Evolut. Comput.*, vol. 6, no. 2, pp. 182-197, Apr. 2002.